Politecnico di Torino

京都工芸繊維大学
KYOTO INSTITUTE OF TECHNOLOGY

Politecnico di Torino

Collegio di Ingegneria Chimica e dei Materiali

Corso di Laurea Magistrale
in Ingegneria Chimica e dei Processi Sostenibili

Marzo 2024

Poly-(l)-lactic acid and Hydroxyapatite nanopowder composite scaffold for bone regeneration in the biomedical field

Relatori:
Prof. Specchia Stefania
Supervisor:
Prof. Marin Elia
Tutor:
Muhammed Daniel Idrus

Candidato:
Barbano Vittorio s292411

Index

Figure list

1. Italian translation of the thesis work

1.1. Introduzione

Il corpo umano è un complesso organismo composto da diversi sistemi che ci permettono di pensare, respirare, muovere, crescere e molto altro. Uno dei più importanti è il sistema scheletrico, il quale fornisce supporto all'intero corpo, protegge gli organi vitali e ci permettere di muovere liberamente. L'elemento costitutivo del sistema scheletrico è l'osso, un tessuto calcificato che si diversifica per fornire svariate funzionalità, dipendentemente dalla posizione nel corpo umano. A livello microscopico, una rete di trabecole forma un tessuto compatto e spugnoso, composto dal 30% di componenti organici e circa il 60% di idrossiapatite, un minerale composto da calcio e fosforo [1]. Questa matrice garantisce la possibilità di resistere a forze di compressioni grazie alla componente minerale, mentre le fibre organiche di collagene mantengono eccellente resistenza alla trazione [2].

Durante il corso della vita, due principali gruppi di cellule mantengono l'osso in buone condizioni, da una parte decomponendo le parti vecchie o danneggiate (osteoclasti), e dall'altra sintetizzando nuovo tessuto osseo (osteoblasti). Ovviamente, non solo il naturale corso della crescita fa sia che ci sia questo ricircolo: piccole fratture, o anche gravi incidenti nel corso della vita, portano ad aumentare la necessità di rigenerare più tessuto osseo, stressando la funzione esplicata dagli osteoblasti. In merito, numerosi sistemi di supporto sono stati sviluppati e applicati in campo medico per aiutare il recupero dei pazienti, come ad esempio l'utilizzo di protesi. Queste ultime, sebbene efficaci, possono portare alla necessità di interventi secondari che possono risultare molto invasivi sui pazienti, quali la rimozione dopo la cura avvenuta, o addirittura la necessità di tenerle per il resto della vita. A causa di questo, sempre più tecniche meno invasive sono state studiate e sviluppate, a partire dal campo medico e fino a quello biomedico, dove nuovi materiali innovativi sono costantemente ricercati ed analizzati per sviluppare campioni sempre più avanzati e innovativi che vengano usati come base per nuovi scaffold ed impianti [4, 5].

Un vasto numero di studi sono stati portati avanti e sono tutt'ora in atto, ma una idea comune sembra fuoriuscire per quanto riguarda la produzione degli scaffold, ovvero l'utilizzo di stampa 3D [10] per stampare in maniera efficace strutture fedeli e con un buon grado di precisione. Tra le diverse tipologie di stampa, che variano dalla classica stampa a filamento fino al

bioprinting [11−26], in questa tesi sono stati sviluppati degli scaffold usando una tecnica basata sul metodo di deposizione per fusione, chiamata melt electro-writing (MEW, elettroscrittura a fusione), usando una macchina autoassemblata guidata elettroidrodinamicamente. Essa si basa sull'uso di una siringa dentro la quale il campione viene fuso; dopo la completa fusione una pressione viene esercitata per movimentare il contenuto e portarlo verso la punta. Da qui, date le dimensioni ridotte di quest'ultima, il fuso rimane attaccato ad essa formando una bolla, a causa della presenza delle tensioni superficiali. L'attrazione delle molecole del fuso viene quindi modificata tramite la formazione di una differenza di potenziale tra anodo (letto di deposizione) e catodo (punta della siringa). Al crescere del potenziale, la tensione superficiale si riduce fino a raggiungere un equilibrio, in cui il materiale forma una struttura a cono chiamata *cono di Taylor*. Aumentando ulteriormente il campo elettrico la tensione superficiale viene meno ed un filamento di fuso viene rilasciato verso il letto di deposizione. Muovendo il letto è quindi possibile utilizzare questo principio per generare una struttura regolare che può anche svilupparsi su più strati, stampati uno dopo l'altro.

Per quanto riguarda il materiale scelto, in letteratura sono stati trovati una grande quantità e tipologie di applicazioni diverse, ma la categoria sulla quale ci si è concentrati è quella dei polimeri, in particolare i polimeri biodegradabili (biopolimeri) [3]: questo perché sono materiali molto promettenti se si guarda alla loro presenza a lungo termine nel paziente. La biodegradabilità può infatti ridurre l'invasività dell'intervento, non richiedendo la rimozione dell'impianto in quanto degradato naturalmente nel lungo periodo di tempo. Inoltre, in questo modo, l'osso appena formato può prenderne il posto dello scaffold e favorire così ulteriormente il processo di rigenerazione.

Uno dei biopolimeri più promettenti in campo biomedico è l'acido poli-lattico (PLA), dotato di eccellenti proprietà meccaniche per sostituire l'osso naturale, così come biocompatibilità e biodegradabilità [27]. Esso può essere ottenuto da canna da zucchero o mais, dove questi ultimi sono fermentati per ottenere l'acido lattico. Il monomero viene quindi polimerizzato, ottenendo così il polimero. L'utilizzo di questo materiale, però, non è solo limitato al campo biomedico: infatti vede utilizzi, per esempio, nel packaging, agricoltura o addirittura l'industria automobilistica, in quanto presenta caratteristiche simile a polistirene, polipropilene e polietilene [28].

Uno svantaggio di questo materiale è la sua instabilità termica [27], che fa sì che il suo processamento sia complicato, specialmente durante le fasi di stampa 3D, in cui viene nuovamente riscaldato, portando a possibili effetti dannosi sullo scaffold finale. Un'altra discrepanza di quest'ultimo quando confrontato con l'osso naturale, è la sua scarsa flessibilità e ridotta attività biologica [27].

Per andare a compensare queste lacune, si è deciso di unire le proprietà di biodegradabilità del PLA con la polvere di idrossiapatite. Questa è un minerale con caratteristiche che combaciano molto bene per lo scopo di rigenerazione ossea: addizionando questo materiale al polimero è possibile migliorare la biocompatibilità favorendo l'adesione cellulare, ed eventualmente agendo come sito di attacco per le cellule [32—35].

Per controllare meglio la struttura polimerica e mantenere per più tempo le caratteristiche meccaniche, si è deciso di utilizzare un particolare tipo di acido poli-lattico, ovvero l'acido poli-(l)-lattico (PLLA), un derivato del PLA ove la reazione di polimerizzazione è stata controllata per favorire la formazione di catene lineari. Il campione è stato quindi preparato come materiale composito formato da una matrice di PLLA in cui nanopolvere di idrossiapatite è dispersa sottoforma di piccole particelle.

1.2. Preparazione del campione

Studi precedenti sul PLLA hanno utilizzato materiali quali tensioattivi o altri additivi al fine di semplificare il processo di omogenizzazione: sebbene questa sembra una buona alternativa, rimane la necessità di rimuovere i componenti in eccesso nelle fasi di downstream. Per questo motivo, in questa tesi è stato deciso di preparare il composito senza l'uso di componenti aggiuntivi, al fine di semplificare e rendere più pulito il processo.

La preparazione del campione è stata eseguita pesando circa 2.5g di pellet di PLLA (130000 MW, Musashino Chemical Laboratory Ltd.) e la quantità corrispondente di idrossiapatite come percentuale in peso, in particolare 1%, 5% e 10%.

Il PLLA pesato è stato quindi trasferito in una fiala da 50mL e cloroformio (≥99.0%, Wako) è stato aggiunto in eccesso al fine di dissolvere completamente il polimero. La soluzione è stata miscelata a 280 rpm e 40°C per 4 ore usando un'ancora magnetica. La fiala è stata mantenuta inizialmente chiusa al fine di evitare l'evaporazione di cloroformio e garantire la corretta dissoluzione del PLLA.

In una fiala da 10mL la nanopolvere di idrossiapatite (Idrossifosfato di calcio, grandezza delle particelle < 200 nm, ≥97%, Sigma-Aldricht) è stata dispersa in cloroformio riempiendola fino a circa metà del volume con il solvente. Il campione è stato quindi immerso in un bagno di acqua distillata (Wako) in un sonicatore a bagno (50/60 Hz, 80 W, Branson) e lasciato agire per 4 ore al fine di permettere una dispersione omogenea della nanopolvere e ridurre la dimensione degli agglomerati.

La dispersione di idrossiapatite è stata quindi trasferita nella soluzione di PLLA e mantenuta in agitazione a 360 rpm e 70°C. Il tappo è stato rimosso per promuovere l'evaporazione del cloroformio. Il campione è stato quindi miscelato per circa 1 ora, o fino a quando la quantità di cloroformio è risultata dimezzata. La soluzione è stata poi colata in una capsula di Petri e lasciata asciugare sotto cappa a temperatura e pressione ambiente durante la notte.

Il campione così ottenuto è stato tagliato in piccoli pezzi rettangolari, che sono poi stati messi ad asciugare ulteriormente in forno a vuoto a 110°C per 2 ore, e poi a 80°C per almeno 6 ore. Ogni campione è stato conservato in una fiala da 50mL.

1.3. Stampaggio dello scaffold

Per ogni sessione di stampa sono stati pesati 0.5 grammi di materiale e mantenuti in forno a 80°C la notte precedente per garantire la completa asciugatura. La cartuccia per il campione è stata precedentemente immersa in cloroformio per dissolvere completamente eventuali residui di stampe precedenti.

La temperatura del letto di deposizione è stata impostata a 80°C per evitare lo shock termico durante la stampa. L'elemento riscaldante è stato impostato a circa 190°C, una temperatura maggiore della temperatura di fusione del materiale, ma non eccessivamente più alta: questo per fare in modo di ridurre il processo di degradazione, un fenomeno influenzato molto dalla temperatura, il quale può ridurre la qualità dello scaffold. Dopo aver inserito la siringa riempita di campione nell'elemento riscaldante, il processo di fusione è iniziato. La punta della siringa è stata posta ad una altezza di 1.5mm dal piano di raccolta. Dopo circa 40÷60 minuti il composito risulta completamente fuso ed il processo di stampa è stato quindi inizializzato. Essendo sia l'umidità ambientale che la temperatura fattori importanti per la corretta riuscita della stampa, due parametri sono stati aggiustati durante ogni sessione: (i) la pressione all'interno della camera del campione, utilizzata per movimentare quest'ultimo; (ii) il campo

elettrico, che permette alla goccia del materiale di essere rilasciata e depositata dalla punta della siringa al letto di raccolta. Nonostante questo, si è cercato di mantenere i parametri sopra citati circa simili tra una sessione e l'altra.

Lo scaffold così stampato consiste in una griglia quadrata con un passaggio tra ogni filamento di 200 µm, 25 linee orizzontali e verticali, 25 strati e 1 cm^2 di area in totale. Per quanto riguarda la geometria dello scaffold usato per i test meccanici, essa è una griglia rettangolare con un passaggio tra ogni filamento di 200 µm, 10 strati e 2.4 cm^2 di area in totale (4x0.6 mm).

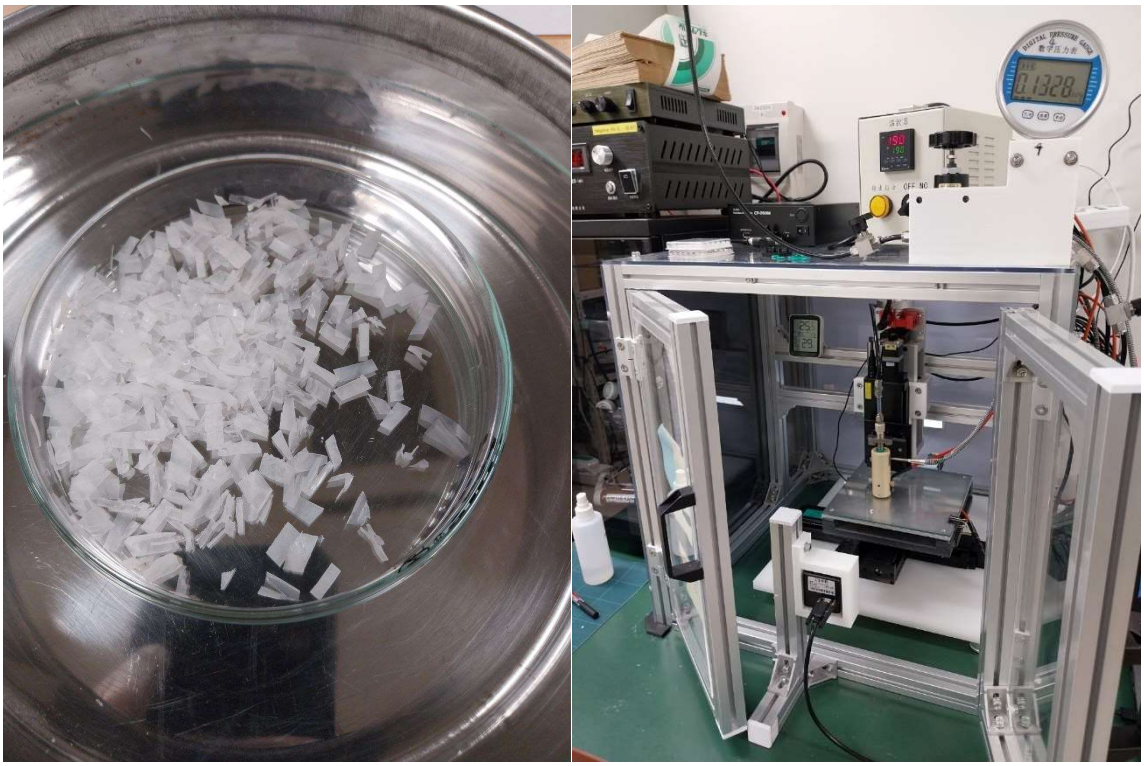

***Figure 1**: A sinistra, il composito ottenuto dopo la fase di asciugatura e taglio; a destra, la stampante ad elettro-scrittura a fusione*

1.4. Caratterizzazione dei campioni

Per caratterizzare i campioni diverse tecniche sono state utilizzate, qui una lista per ogni macrogruppo di tecniche:

- <u>Caratterizzazione morfologica</u>
    - Microscopio a Laser.
    - Microscopio a Scansione Elettronica (SEM).
- <u>Tecniche di caratterizzazione chimica non distruttive</u>
    - Angolo di contatto.

    - Spettroscopia IR a trasformata di Fourier (FT-IR).
    - Spettroscopia Raman.
    - Spettroscopia a raggi X a Dispersione di Energia (EDS).
    - Diffrattometria a raggi X (XRD).
- Tecniche di caratterizzazione chimica distruttive
    - Calorimetria a Scansione Differenziale (DSC).
    - Analisi Termo-Gravimetrica (TGA).
- Test meccanici
- Tecniche di caratterizzazione biologica
    - Citotossicità.
    - Test di acidità.

1.5. Risultati

In questo lavoro, campioni con concentrazioni diverse di idrossiapatite sono stati preparati, in particolare 0%, 1%, 5% e 10% in peso rispetto alla componente di PLLA.
I due materiali sono stati combinati a formare i seguenti compositi:

- PLLA con 1% in peso di idrossiapatite (PLLA-1%).
- PLLA con 5% in peso di idrossiapatite (PLLA-5%).
- PLLA con 10% in peso di idrossiapatite (PLLA-10%).

Che sono stati utilizzati per produrre quattro scaffold differenti:

- Scaffold con 0% in peso di idrossiapatite (MEW-0%).
- Scaffold con 1% in peso di idrossiapatite (MEW-1%).
- Scaffold con 5% in peso di idrossiapatite (MEW-5%).
- Scaffold con 10% in peso di idrossiapatite (MEW-10%).

1.5.1. Caratterizzazione morfologica

Microscopio laser ed immagini SEM dei diversi scaffold sono state acquisite per valutare la qualità dei campioni post stampaggio. Da **Fig. 2** si può notare come la morfologia cambia in funzione della concentrazione di idrossiapatite. Le immagini mostrano che, all'aumento del contenuto di idrossiapatite, la morfologia dello scaffold diventa meno precisa. Questo è

probabilmente causato da due fattori: (i) essendo l'idrossiapatite un materiale poco conduttivo, essa va ad influenzare l'effetto del campo elettrico durante il processo di elettro-scrittura, riducendo la qualità del cono di Taylor che si va a formare, e di conseguenza la deposizione del fuso; (ii) aggiungendo idrossiapatite all'interno della matrice polimerica, la risultante diventa una struttura più irregolare e meno omogenea, dove le catene di PLLA sono ostacolate dalla nanopolvere, cambiando la proprietà e la densità del composito così ottenuto. Un altro fenomeno importante che si viene ad instaurare durante la stampa è l'effetto di resistenza che lo scaffold stesso esercita sul campo magnetico all'aumentare del numero di strati, che porta ad una minore qualità della struttura man mano che la stampa procede. Una soluzione a questo fenomeno sarebbe quella di modificare la differenza di potenziale durante la stampa per ogni scaffold ed all'aumentare degli strati. Questo però non è stato applicabile data l'assenza di una sorgente automatica di potenziale.

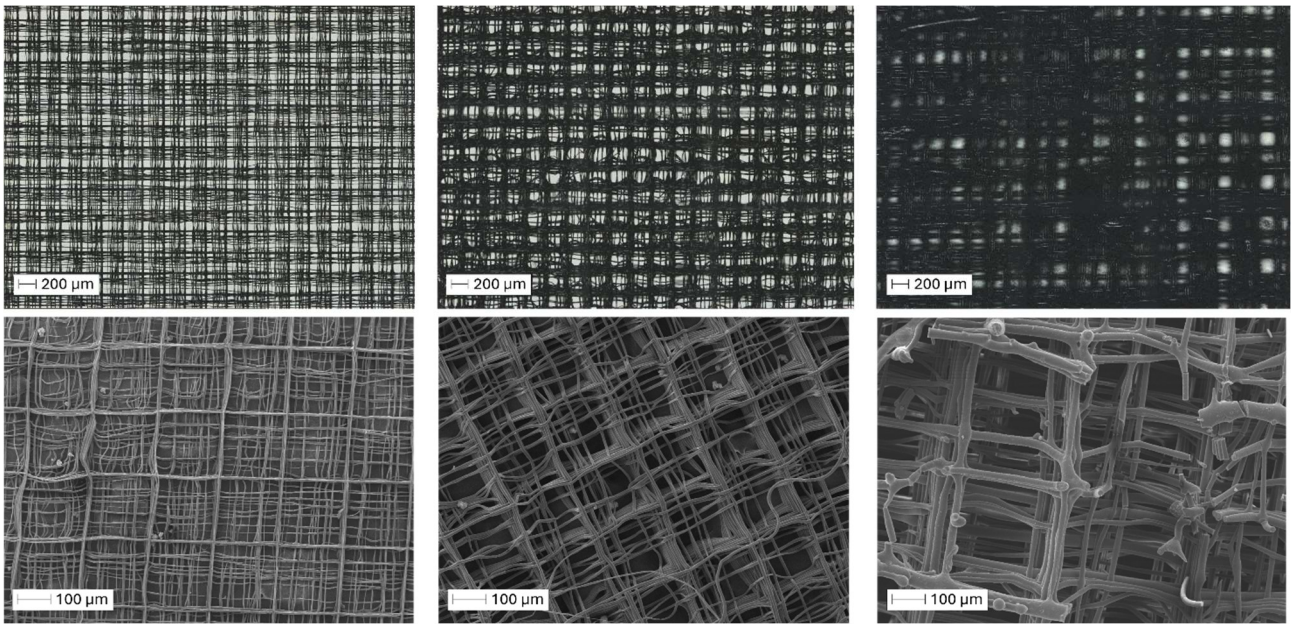

***Figure 2**: In alto, immagini a microscopio ottico; in basso, immagini SEM. Da sinistra a destra: MEW-1%, MEW-5%, MEW-10%*

1.5.2. Caratterizzazione chimica non distruttiva

Angolo di contatto

Il test dell'angolo di contatto è stato performato per verificare cambiamenti sulla bagnabilità degli scaffold al variare della concentrazione di idrossiapatite: questa proprietà è importante

per quanto riguarda l'interazione tra il materiale e l'ambiente circostante, oltre alle cellule osteoblastiche stesse, quando collocato nel paziente.

Quando comparati allo scaffold puro, i risultati mostrano una leggera riduzione di idrofobicità in MEW-1%, proprietà che sembra aumentare nuovamente passando a MEW-5% e poi MEW-10%.

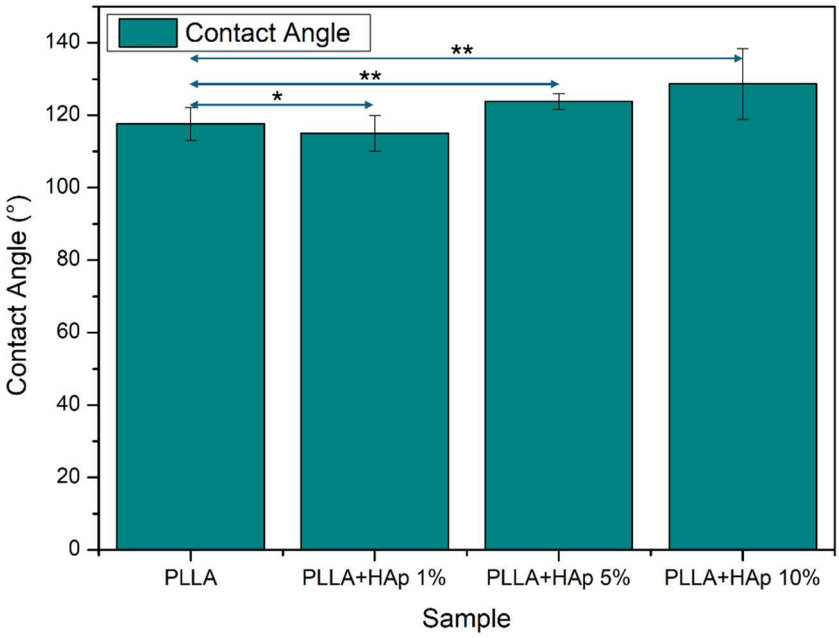

***Figure 3**: Risultati dell'angolo di contatto al variare del contenuto di idrossiapatite.*

FT-IR

Misurazioni FT-IR sono state prese per verificare la presenza di idrossiapatite nei diversi materiali grezzi e scaffold. Come controllo, le componenti pure sono state anche analizzate per visualizzare i picchi tipici di entrambi i materiali.

Purtroppo, i risultati mostrano una netta sovrapposizione delle bande di idrossiapatite con quelle di PLLA, portando ad una difficoltà nel discriminare le due componenti nello spettro del composito, come confermato dall'analisi di MEW-1%.

Spettroscopia Raman

Analogamente a FT-IR, la spettroscopia Raman è stata utilizzata per verificare la presenza di idrossiapatite nei compositi prodotti.

Dopo l'analisi dei campioni puri, un picco dell'idrossiapatite a 960 cm^{-1} si è rivelato non sovrapposto alle bande di PLLA. La conferma della lettura qualitativa del contenuto di idrossiapatite è stata confermata con la mappatura dei campioni, come mostrato in **Fig. 4**.

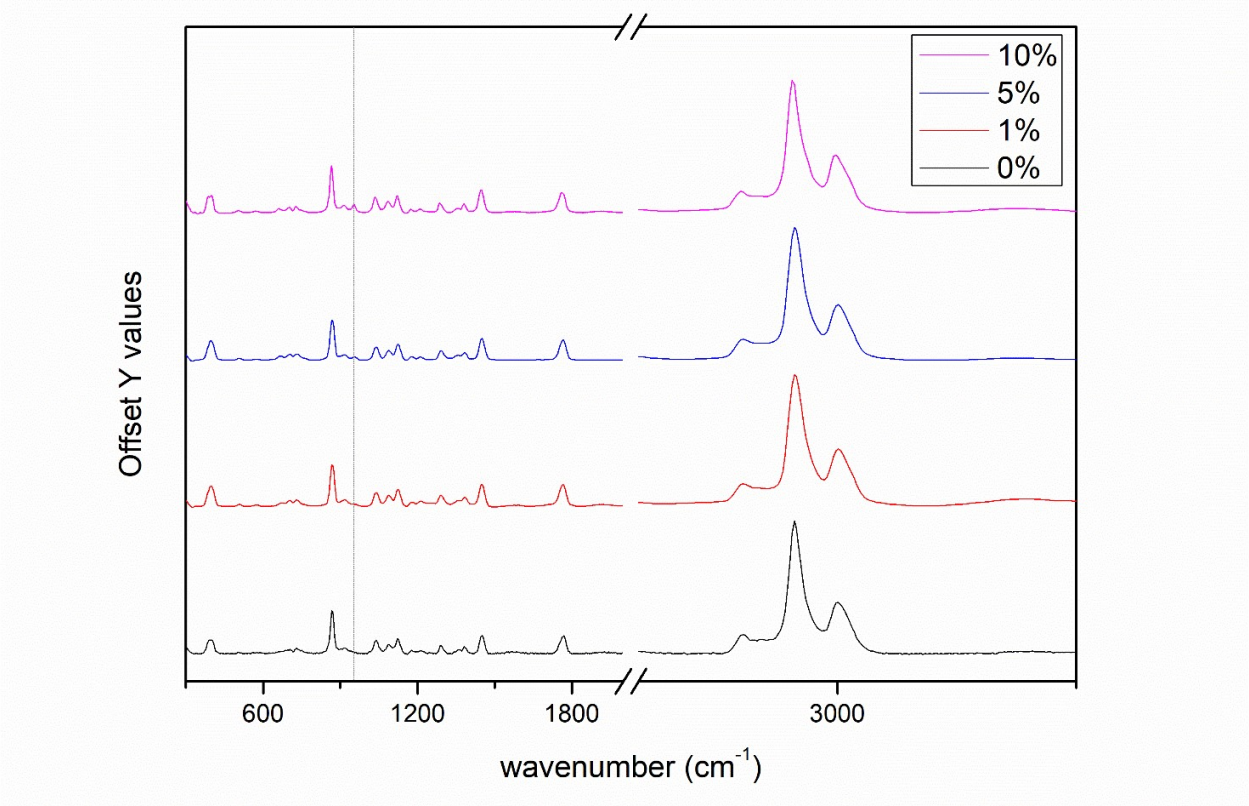

***Figure 4**: Confronto tra gli spettri Raman dei diversi materiali grezzi come funzione del contenuto di idrossiapatite (dal basso verso l'alto). La retta tratteggiata evidenzia la banda Raman a 960cm^{-1}*

Quando si confronta l'intensità del picco di idrossiapatite a 960 cm^{-1} con in contenuto nel composito, un'ottima proporzionalità può essere vista, che conferma le corrette proporzioni dei materiali nei compositi.

Risultati analoghi sono stati ottenuti facendo la mappatura dei filamenti dopo elettro-scrittura, mentre tramite imaging si può vedere una buona dispersione delle particelle di idrossiapatite, nonostante alcuni agglomerati rimangono presenti, in particolare per quanto riguarda MEW-10%:

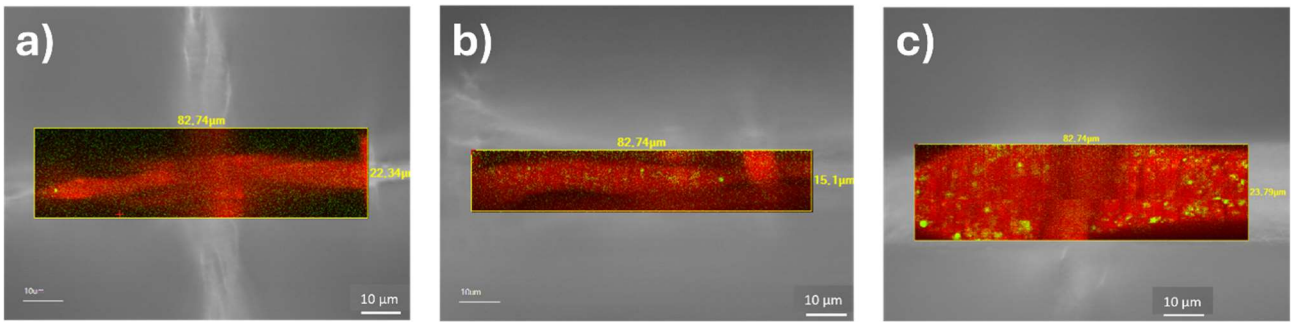

***Figure 5**: Risultati di imaging Raman dei diversi scaffold. a) MEW-1%, b) MEW-5%, c) MEW-10%. Il colore rosso è stato usato per mostrare il PLLA, mentre quello verde per l'idrossiapatite*

EDS

L'analisi EDS è stata utilizzata per verificare ulteriormente la presenza e dispersione di idrossiapatite nei campioni. La presenza di Carbonio, Ossigeno, Calcio e Fosforo è stata esaminata utilizzando il settaggio di scansione della superficie ad alta intensità del SEM, per migliorare il rilevamento dei segnali degli elementi.

I risultati hanno mostrato una alta concentrazione di fosforo nell'intero scaffold e perciò, per verificare che non siano stati segnali di artefatti, una scansione del background è stata anche eseguita per non commettere errori nella lettura finale. Come immaginato, le immagini EDS mostrano una alta concentrazione di fosforo nel materiale di riferimento, mentre il calcio rimane in basse quantità. Di conseguenza si è deciso di utilizzare le sole letture del calcio come riferimento alla presenza di idrossiapatite. **Fig. 6** mostra le immagini EDS dei tre compositi, dove la nanopolvere risulta dispersa abbastanza uniformemente, mentre il segnale aumenta sempre di più all'aumentare del contenuto di idrossiapatite.

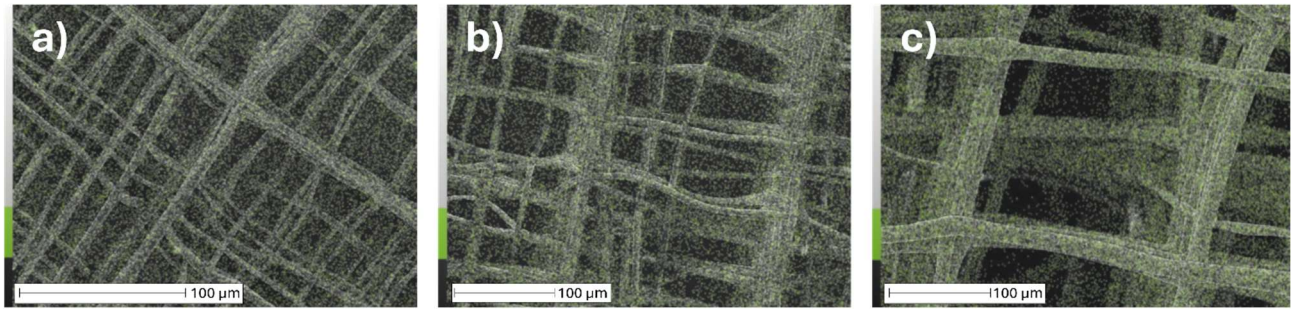

***Figure 6**: distribuzione del calcio negli scaffold compositi, misurata tramite EDS: a) MEW-1%, b) MEW-5%, c) MEW-10%*

XRD

Diffrattometria a raggi X è stata utilizzata per valutare il grado di cristallinità dei materiali grezzi e scaffold. In particolare, data la presenza del polimero, costituito da una struttura parzialmente amorfa e parzialmente cristallina, si è voluto osservare come la proporzione tra queste due strutture cambi con l'aumento del contenuto di idrossiapatite.

I risultati mostrano una riduzione della cristallinità del composito quando si aumenta la quantità di idrossiapatite, come può essere visto in **Fig. 7**.

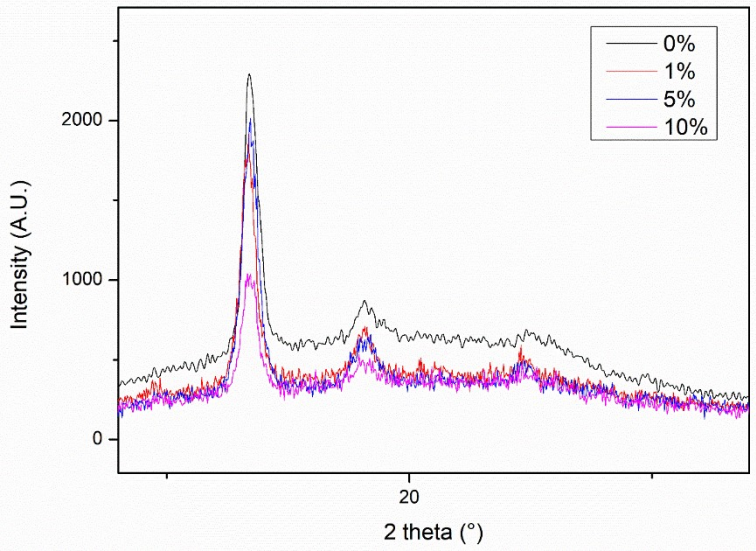

***Figure 7**: Pattern di diffrazione a raggi X per i materiali grezzi, come funzione del contenuto di idrossiapatite*

Questo indica quindi che la presenza di idrossiapatite va ad influenzare la formazione delle zone cristalline, e quindi ostacola le fibre di PLLA. Inoltre, si è visto che il grado di cristallinità scende rapidamente appena si aggiunge la componente minerale, per poi scendere gradualmente all'aumentare di quest'ultimo.

DSC

L'analisi calorimetrica è stata performata per valutare il cambiamento nella temperatura di fusione dei vari campioni dopo la preparazione. **Tab. 1** mostra i risultati così ottenuti. Considerando anche gli errori nella misura, non risulta esserci una sostanziale variazione nella temperatura di fusione con l'aggiunta di idrossiapatite, suggerendo quindi che non ci sia una

vera e propria interazione chimica tra le due componenti, e la struttura del PLLA non è alterata macroscopicamente dalla presenza delle particelle.

***Table 1**: Risultati del test calorimetrico relativi alla temperatura di fusione dei campioni*

Campione	Temperatura di fusione (°C)	Deviazione standard
PLLA	174.81	0.87
PLLA-1%	175.66	1.28
PLLA-5%	176.04	0.38
PLLA-10%	175.22	0.31

TGA

L'analisi termo-gravimetrica è servita per valutare la decomposizione degli scaffold, oltre ad avere una misura effettiva della quantità di materiale rimanente al termine della prova. Dato che la temperatura massima raggiunta durante l'analisi è pari a 600°C, è lecito ritenere che l'unica componente rimanente nei contenitori sia l'idrossiapatite, un minerale ceramico con proprietà di resistenza termica molto più elevate. **Fig. 8** mostra chiaramente come il peso residuo al termine della prova aumenti all'aumentare del contenuto di nanopolvere. Tramite un fitting della quantità sopracitata in relazione al contenuto teorico delle diverse stampe, si può confermare che questi siano stati preparati correttamente, risultando in una buona qualità in termini di composizione.

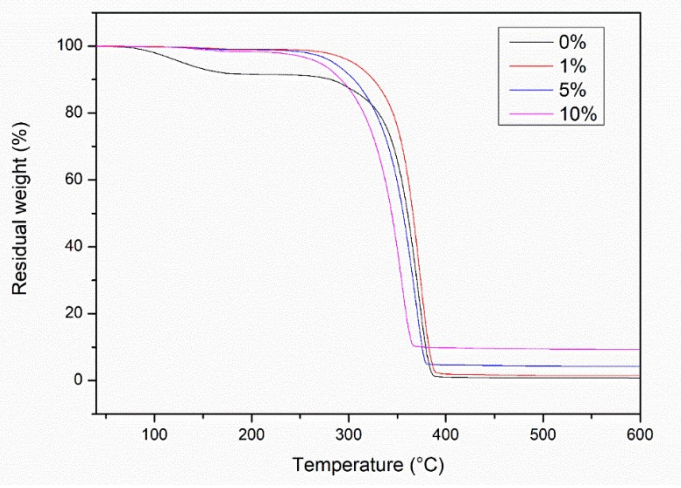

***Figure 8**: Curve TGA dei diversi scaffold, come funzione del contenuto di idrossiapatite*

Test Meccanici

La prova di trazione è stata effettuata sugli scaffold ottenuti da elettro-scrittura di forma rettangolare, come dettagliato in precedenza, di dimensioni 4x0.6 mm (10 strati in spessore). Ogni campione è stato bloccato alle estremità a formare una sezione di test alta 2 mm.
Dalla curva sforzo-deformazione in **Fig. 9** si può subito notare come l'aggiunta di idrossiapatite porta i campioni a cambiare da materiale elastico a materiale fragile. Sebbene l'aggiunta di una bassa quantità di idrossiapatite (MEW-1%) porti alla riduzione anche delle altre proprietà meccaniche, aumentando il contenuto fino al 5% si ottiene uno scaffold con maggiore resistenza, e modulo elastico addirittura doppio rispetto al polimero puro. Le proprietà meccaniche iniziano poi a declinare nuovamente all'aumento ulteriore di idrossiapatite.

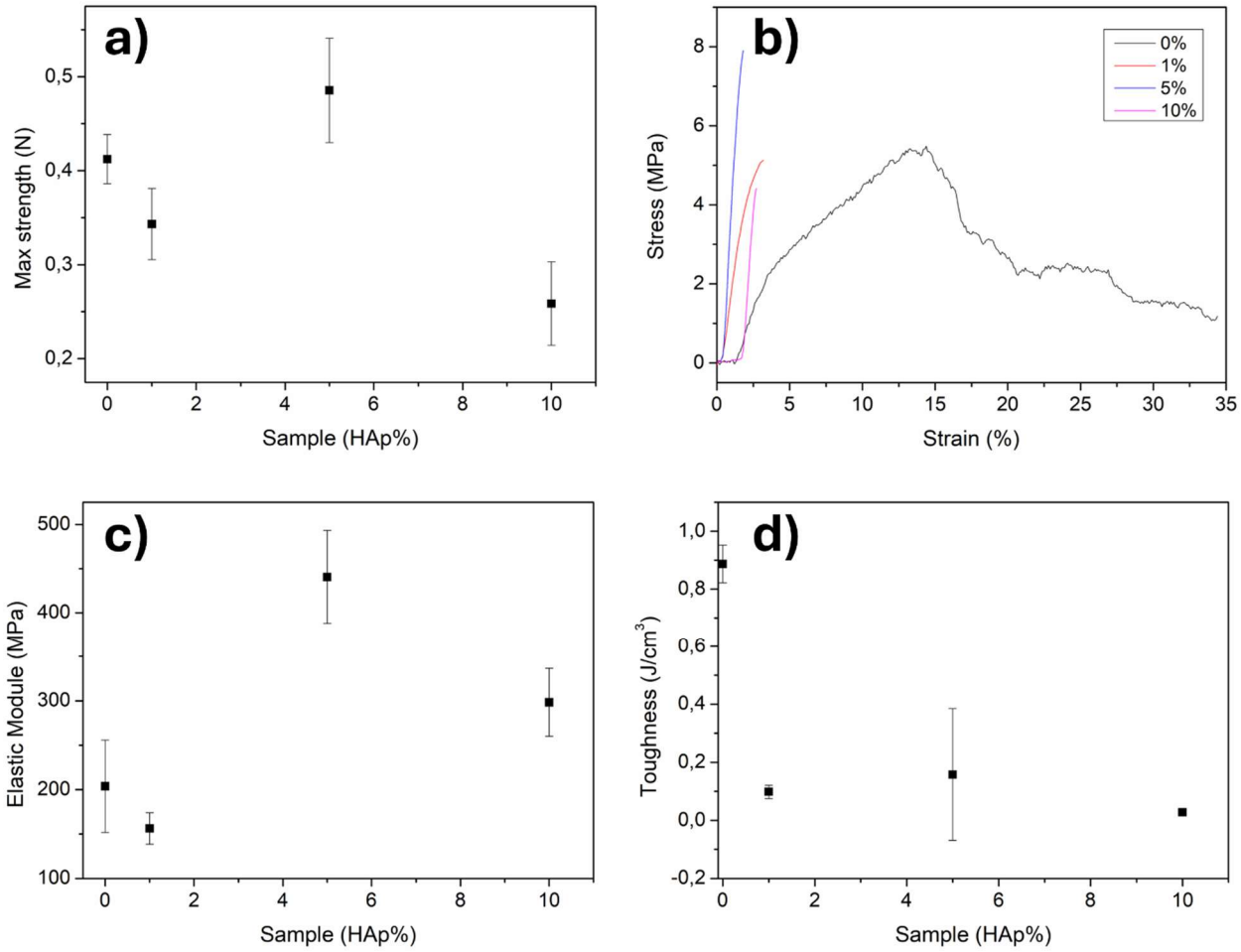

***Figure 9**: Risultati dei test meccanici. a) Tensione di rottura; b) curva sforzo-deformazione; c) modulo elastico; d) tenacità*

Citotossicità

Test di citotossicità WST-8 è stato utilizzato su fibroblasti dermici umani (Human Dermal Fibroblast, HDF) in presenza degli scaffold elettro-scritti, in particolare MEW-0%, MEW-1%, MEW-5% e MEW-10%. I campioni sono stati preparati, e due batch sono stati poi incubati per 24 e 72 ore, rispettivamente.

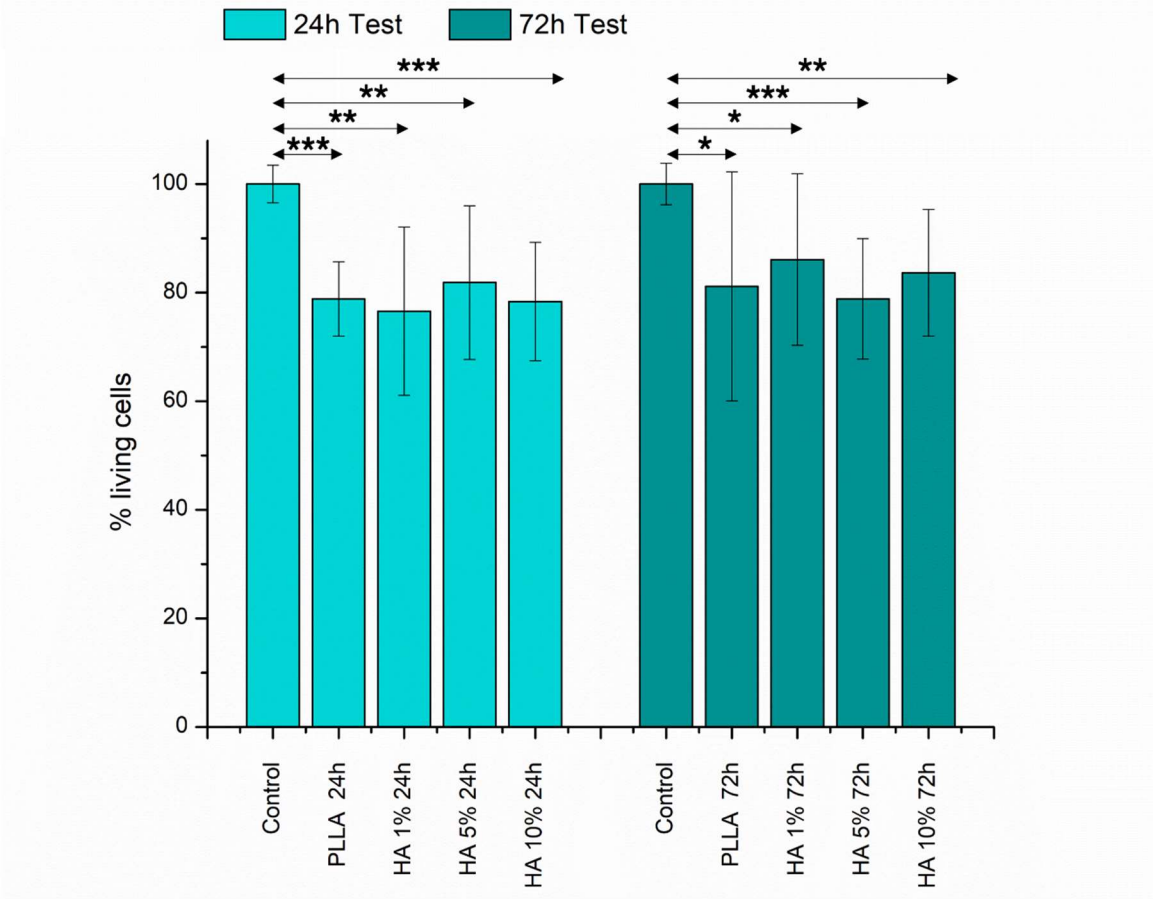

***Figure 10**: Risultati della prova di citotossicità effettuati sui diversi scaffold. A sinistra, dopo 24 ore; a destra, dopo 72 ore*

Fig. 10 mostra i risultati di entrambi i test: come si può vedere, circa l'80% delle cellule rimane vivo in ogni scaffold, confermando la non-citotossicità di questi ultimi. Inoltre, per quanto riguarda la parte di cellule non presente, è possibile che non sia completamente morta, ma che una parte sia rimasta attaccata ai diversi scaffold. Sebbene possa essere un risultato molto promettente in previsione dei test di bioattività, non è stato possibile confermare quanto detto a causa della difficoltà nella lettura, oltre alla trasparenza delle cellule, che risultano quindi complicate da individuare nella struttura degli scaffold.

Test di acidità

In letteratura sono state trovate alcune note relative alla degradazione del PLLA, che può portare ad una acidificazione dell'ambiente circostante. Per verificare ulteriormente questo fenomeno, un semplice test di pH è stato effettuato su campioni composti da 6mL di culture media (lo stesso usato per la citotossicità) e 6mg di materiale grezzo (PLLA-1%, 5% e 10%). Sebbene i risultati facciano notare una leggera acidificazione della soluzione, la presenza di idrossiapatite sembra rallentare questo processo, come visto in letteratura. Data la riduzione complessiva di pH molto limitata, si è affermata la non pericolosità di questo fenomeno durante il processo di rigenerazione nel paziente.

1.6. Discussione e conclusioni

In questa tesi, scaffold di idrossiapatite in PLLA (0%, 1%, 5% e 10% in peso) sono stati stampati in 3D usando la tecnica di elettro-scrittura a fusione usando una macchina autoassemblata guidata elettroidrodinamicamente.

Le tecniche di caratterizzazione morfologica eseguite con microscopio laser e SEM hanno mostrato come la presenza di idrossiapatite nella matrice polimerica porti ad una riduzione della qualità dello scaffold così stampato, in quanto il campo elettrico è influenzato dalla sempre maggiore presenza della nanopolvere, che destabilizza la differenza di potenziale esercitata durante la stampa.

Le caratterizzazioni chimiche fatte con FT-IR, EDS e spettrometria Raman hanno mostrato una buona uniformità nella distribuzione di idrossiapatite nei materiali grezzi e scaffold, con un aumento qualitativo del segnale all'aumentare della concentrazione. Risultati quantitativi sono stati invece ottenuti tramite la tecnica termo-gravimetrica, che ha effettivamente mostrato proporzionalità tra peso finale del campione a fine prova e contenuto teorico dei campioni, confermando una buona qualità dei compositi in relazione alla preparazione di questi ultimi. Analisi DSC è stata inoltre eseguita, ma nessun importante cambiamento nella temperatura di fusione è stato ottenuto, indicando un legame non chimico tra le due componenti. Il grado di cristallinità è stato inoltre comparato alla temperatura di decomposizione dei materiali, evidenziando una relazione per cui all'aumento del grado di cristallinità avviene un aumento della temperatura di decomposizione. L'analisi dell'angolo di

contatto ha mostrato un aumento della idrofobicità, specialmente per MEW-5% e MEW-10% quando comparato al controllo MEW-0%.

I test meccanici hanno evidenziato un netto cambiamento di proprietà del materiale, che è diventato completamente fragile. Nonostante questo, MEW-5% ha mostrato ottimi miglioramenti in termini di resistenza e resilienza, con un modulo elastico nettamente aumentato.

L'acidificazione dell'ambiente circostante gli scaffold è stata verificata e nessun dato ha evidenziato un grave cambiamento di pH che potrebbe compromettere la cura del paziente. Infine, i test di citotossicità hanno confermato la compatibilità degli scaffold con la colonia cellulare, dando ottimi risultati in previsione dei test biologici.

Sebbene ulteriore ricerca potrà sicuramente migliorare le conoscenze sulla tecnica di produzione usata, ed il comportamento ed il cambiamento delle proprietà al variare del contenuto di idrossiapatite, questa tesi ha portato alla luce un materiale composito molto promettente con proprietà interessanti per applicazioni nella rigenerazione ossea in campo biomedico.

2. Abstract

Due to the aging population, the need for new materials for bone regeneration that can substitute natural bone is increasing. With the requirement of biodegradability and biocompatibility, many possibilities have been developed in recent years.

In this thesis, a composite made with poly-(l)-lactic acid (PLLA) and hydroxyapatite has been developed and characterized. The amount of hydroxyapatite was chosen as a weight percentage of PLLA, in particular 1%, 5% and 10%. The composite was made by solubilizing PLLA in chloroform by mixing, and dispersing hydroxyapatite in the same solvent in another vial via bath sonication. The samples were combined, dried, ground and then dried in vacuum oven again. A self-assembled electrohydrodynamics guided melt electro-writing 3D printer was then used to make scaffolds of the composite materials. Laser microscope and SEM analyses were used to show the structure of the scaffold after printing and its change with the amount of hydroxyapatite.

FT-IR, EDS and Raman techniques were employed to verify the presence of hydroxyapatite and its distribution in the raw material and after melt electro-writing. Contact angle was performed to investigate the hydrophobicity or hydrophilicity of the scaffolds. XRD has been applied to highlight any change in the crystallinity of the composites before and after printing. DSC and TGA techniques were used to respectively examine the melting temperature and degradation of both the raw materials and their scaffolds. Finally, cytotoxicity test was performed to confirm the non-toxicity of the scaffolds, and acidity test was performed to ensure a non-acidification of the scaffold's surrounding environment due to PLLA degradation. Optical characterization analyses have shown an overall good quality print of the scaffold, very dependent on the amount of hydroxyapatite, which influences the printing itself. Chemical characterizations showed a good quality dispersion of the nanopowder in the raw material, as well as in the scaffold after printing, maintaining the percentage ratio of hydroxyapatite in relation to PLLA. Mechanical testing showed brittle properties of the composites, while an increase in strength and elastic module can be highlighted for some analytes, when compared to the pure PLLA. The hydrophobicity of the scaffolds was confirmed by the contact angle, and

non-toxicity has been observed with the WST-8 cytotoxicity test. Finally, PLLA degradation was assessed to be non-critical. Although further research would only improve the knowledge of this material and all of its properties, the research shows promising results for a biocompatible and biodegradable composite that can positively impact the bone regeneration field in biomedicine.

3. Aim of the thesis

Nowadays, the need for new and simple substitute materials for bone regeneration is increasing, thus the need to study and test different methods and materials for scaffold production.

One of the most interesting candidates for this application is poly-(l)-lactic acid (PLLA), thanks to its chemical and biodegrading properties. Though it lacks in mechanical and bioactivity properties, a way to compensate has been investigated: the production of a composite where hydroxyapatite nanopowder is dispersed in a matrix of PLLA shall result in a material with both PLLA biodegradability properties and the biocompatibility and bioactivity properties of hydroxyapatite. The latter, in fact, is also a bone constituent and should very much be compatible with the cells to favor their adhesion on the scaffold.

The subject of this thesis is the analysis of the PLLA/hydroxyapatite composite properties with different percentages of the latter (as wt% of PLLA), to verify its applicability in the biomedical field as a scaffold for bone regeneration in patients with bone injuries**.** The prepared sample will act as a basis for future works in terms of composite and scaffold preparation for bone regeneration.

The raw material was firstly prepared by dissolving PLLA pellets in chloroform and then mixing this with different percentages (wt.% of PLLA) of hydroxyapatite (1%, 5% and 10%). The resulting composite, after being dried and removed the chloroform component, has undergone the melt electro-writing printing process, an advanced technique to produce high definition and small-scale scaffolds.

The raw materials thus obtained were characterized with different techniques: for optical characterization, SEM and laser microscope were used to evaluate the structure of the printed scaffolds; FT-IR, EDS and Raman spectroscopy were adopted to evaluate the presence, concentration, and dispersion of hydroxyapatite in the raw material and post-printing; contact angle test checked the wettability of the scaffolds, while XRD analyzed the degree of crystallinity. Tensile strength tests were also applied to evaluate the mechanical properties of

the scaffolds. Finally, cytotoxicity and acidity test were performed to make sure the scaffolds were not toxic to the cells and the polymer degradation would not critically affect the nearby environment.

The results show that hydroxyapatite has been homogeneously dispersed in the PLLA matrix, thus resulting in a homogeneous composite. Raman spectroscopy and EDS show a qualitatively good dispersion of hydroxyapatite, and a signal coherent with the predicted amount in the raw materials and scaffolds. TGA qualitatively confirmed this results by evaluating the remaining weight after the test as a function of hydroxyapatite content. Tensile tests have shown brittle behavior of the scaffolds, while mechanical properties have improved with a 5% content of hydroxyapatite. WST-8 test confirmed non-cytotoxicity of the scaffolds, while acidity test has shown that polymer degradation is a non-critical point and to be not dangerous for the patient.

The results lead to the conclusion that a PLLA/hydroxyapatite composite for bone regeneration is feasible and interesting properties have been highlighted after characterization.

4. Introduction

4.1. The bone and its properties

The human body is a marvelous complex machine consisting of many different systems that makes us able to think, breathe, move, grow and much more. One of the most important parts of our body is the human skeletal system, providing support to the whole body, protects vital organs and with its articulations lets us move freely. The building block of all this is bone, a calcified tissue that persists through all of our life and grows with us, especially during our first two decades. Nevertheless, bone in general is not enough to describe this system: in fact, there are many different types of bones, all with their own shape and structure; long bones, short bones, flat bones and irregular bones are arranged to provide functionalities in different regions of the body. Microscopically speaking, a network of trabeculae forms a compact and spongy tissue that grants both strength and flexibility to the system. With approximately 30% of organic components – mainly proteins such as collagen – and about 60% of hydroxyapatite, a mineral composed of calcium and phosphate, and the remaining part of water, this matrix grants the bone its rigidity and hardness, essential for its mechanical functions [1]. Bone, in fact, has the ability to withstand compressive forces thanks to the mineral component, while collagen fibers allow for an excellent tensile strength element [2].

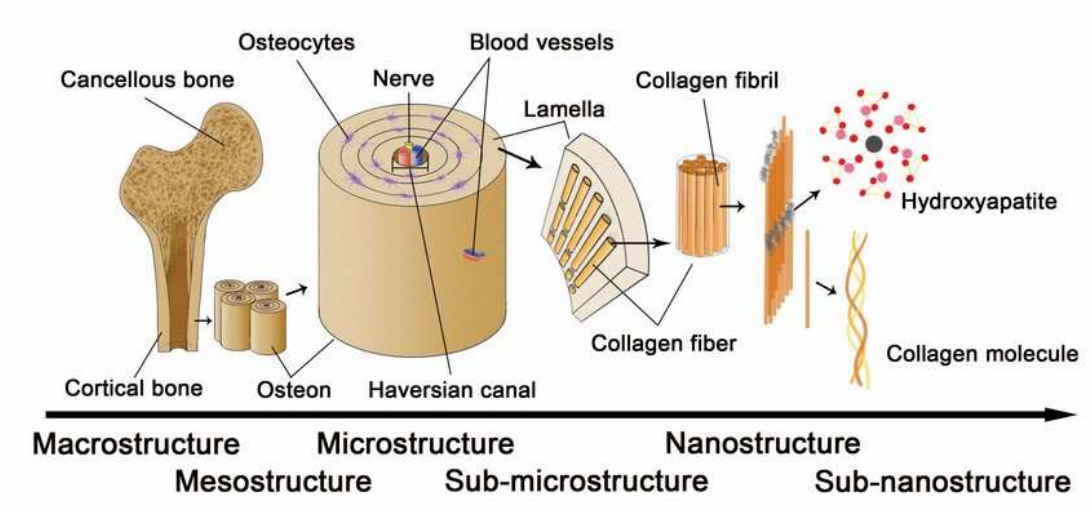

***Figure 11**: Bone hierarchic structure [3]*

As previously stated, the skeletal system undergoes numerous changes, regenerations, and remodeling during life; these are owed to two important types of cells: the osteoblasts, bone-forming cells responsible for the synthesis and deposition of new bone tissue; and the osteoclasts, bone-resorbing cells that breakdown and remove old bones, or even damaged sections of the tissue, helping the renewal and homeostasis of the bone tissue. Indeed, the physiological and growth processes that occur during the life of an individual, are not the only cause of bone reshaping and/or renewal. To this, external factors may also occur, such as light blows, deep cuts that damage the bone surface, up to serious injuries like complete bone breakage; human diseases are also to be kept in mind, as genes play an important role in this, influencing the development and susceptibility to those complications. To all these aspects, different external support systems have been used in the medical field, in order to help bone regeneration and ease the patient's aches during recovery, as well as treatment and measures for individuals at risk. A simple and straightforward option is the use of prosthetics, mainly metallic structures that are surgically implanted in the patient to substitute or support the wounded bone; in the long term, the patient will either have to undergo a second surgery for its removal or keep the whole prosthetics in the body for the rest of his or her life. Due to the invasiveness of this procedure, more and more techniques have been studied and tested to reduce this aspect, starting from the medical field in general, all the way to the biomedical field, where materials and substances are studied to develop new and advanced solutions as basis for scaffolds and implants[4, 5].

For that reason, in the biomedical field there is a growing demand for effective materials that can be used for patient treatment. In the topic of bone regeneration, artificial substitutes are more and more in need when trying to improve and accelerate bone healing and regrowth, as only the natural metabolism results in a slow healing process, despite the great properties of the natural bone, especially when speaking of some patient conditions like osteoporosis, osteonecrosis, and osteomalacia [6]. Indeed, several materials have been studied and combined to obtain a sustainable, cost efficient and simple-crafting result, with both *in vitro* and *in vivo* experiments [7–9]. While the only material study is not enough, the structure of the implant is also of fundamental study to simulate bone-like (or better) conditions during the healing process in the patient. In particular, porosity and pore size are fundamental parameters to make sure the cells are able to diffuse and proliferate in the implant [1, 4]. To

do so, many scaffold production techniques have been studied and applied to the different materials.

4.2. Scaffolding for bone regeneration

Currently, 3D printing techniques are the most popular way to produce a high-quality and fidelity scaffold [10]: the fundamental printing process is the so-called Fused Deposition Modelling (FDM), where the material gets melted, extruded and dropped on the print bed; the melt gets released as a continuous thread, and multiple layers are made by laying the filament above the previously print sections: this makes it possible to create a complete three-dimensional structure. From this basis, several techniques have been developed over the years, all with their features and strength points. **Tab. 2** shows different materials that have been studied, and the printing technique used:

***Table 2**: Applications of innovative materials and techniques for bone regeneration scaffolding*

Material Category	**Techniques Used**	**Applications**	**Characteristics and Results**	**Reference**
Haversian bone	Digital Laser Processing 3D printing	Bone-mimicking scaffold for multicellular delivery	Good control over compressive strength and porosity of scaffolds	[11]
Polycaprolactone (PCL) – Hydroxyapatite	Fusion Deposition Modelling (FDM)	Biocompatible filaments	Facilitation in the fabrication of biocompatible structures	[12]
Poly (propylene fumarate)	Stereolithography (SLA)	Curable scaffolds with controlled microstructure	Accuracy on the xy-plane and minimization of overcuring	[13]
PCL/multicomponent	FDM	Scaffold for potential	Improvement of compressive strength and	[14]

bioactive glass		application in bone tissue engineering	increased hydrophilicity, apatite-forming ability and cytocompatibility	
Poly-(l)-lactic Acid (PLLA)/hydroxyapatite	FDM	Personalized bone tissue engineering scaffolds	Decrease in crystallinity of PLLA with the increase in hydroxyapatite weight fraction. Femur and tibia-like mechanical strength	[15]
Silica-based bioactive glass	Robocasting technology	Cylindrical grid-like scaffolds	Apatite-forming ability, osteogenic effect upon implantation	[16]
Alginate/Gelatin Hydrogel Ink containing bioactive glass 45S5 and ZIF-8 nanoparticles	Pneumatic extrusion-based bioprinter	Pneumatic extrusion-based bioprinting of scaffold, further treated via cross-linking	Increase in degradation rate and bioactivity	[17]
Collagen Hybrid Formulations	Bio X Bioprinter + Genpin crosslinking	Mesh-like scaffolds via bioprinting, then treated with cross-linking technique	High biocompatibility of the hybrid system	[18]
Gelatin/β-Tri-Calcium Phosphate	3D Bioprinting + crosslinking	Scaffold bioprinting with post-print cross-linking	Compressive strength similar to of cancellous bone, good cellular activity with preosteoblasts, bone	[19]

			formation with no inflammation	
rhBMP-2 Loaded PCL/β-TCP/bdECM	Multihead Deposition Systems (MHDS)	Square shaped scaffolds	Enhanced cell bioactivity and higher bone volume and area	[20]
PCL/fucoidan	Melt-plotting system| layer-by-layer	Layer-by-layer composite scaffold	High increase in hydrophilicity and mechanical properties, easy adhesion of cells and enhanced mineral deposition	[21]
Poly(lactide-co-glycole)/titania composite	Cylindrical silica gel mold	Bone repair	Large enhancing of mechanical properties, increased cell proliferation, increased ALP activity of osteoblasts when cultured on composite scaffolds	[22]
PMMA/ZnO	Electrospinning	Fibers and films	Hydrophobic structure, good biocompatibility, although bioactivity inhibited with 15% ZnO	[23]
-Bioactive porous Ti alloy -Ti-Ta-Nb-Zr alloy	Selective Laser Melting (SLM)	-Direct treatment of bone defects -bone regeneration and osteointegration	-Improved repair of bone defects on one sample, while improved formation of new bone tissue for another one	[24] [25]

			-enhanced osteogenic differentiation, excellent osteogenic activity	
Hydroxyapatite-based honeycomb scaffold	Electrophoretic deposition dip coating (EP2D)	Bone implant application	Compressive strength within the average of human cancellous bone	[26]

As can be seen, there is a lot of variety in terms of both materials and techniques. Especially polymers see a high range of applications and available printing processes they can go through. This is not surprising, as another important property demand for the substitute material is the biodegradability: biobased polymers, in fact, are promising materials to support bone growth and regeneration due to their biocompatibility and biodegradability properties [3]. The latter is a crucial point when talking about scaffolding for implants, as there is the need for the non-human-derived material to not remain inside the patient for a prolonged period of time. This also ensures that the polymeric scaffold is then replaced by the newly formed bone.

In that regard, poly-lactic acid (PLA) is a very promising biopolymer for biomedical applications, holding appropriate mechanical properties to replace natural bone, as well as excellent biocompatibility and biodegradability [27]. PLA can simply be obtained by treatment of corn or sugar cane, where the produce is fermented to obtain lactic acid. Finally, the monomer is polymerized, and the polymer is obtained (**Fig. 12**). PLA is not only used in the biomedical field though: this biodegradable polymer, in conjunction with its excellent characteristics that similar polystyrene, polypropylene or polyethylene [28], can be used for the production of packaging for food, single-use products, textiles or even in the automotive industry as interior components or under-the-hood gears [29].

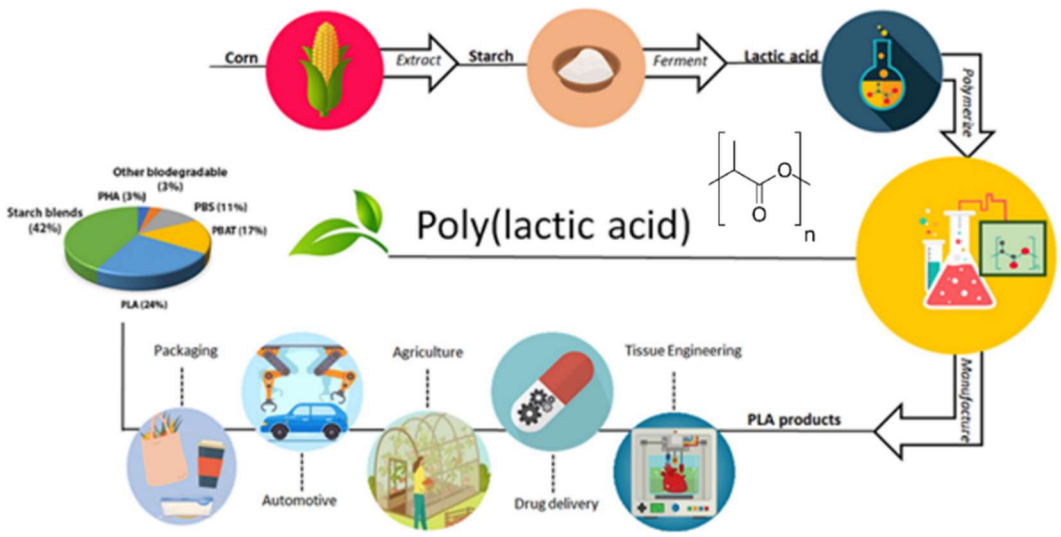

***Figure 12**: Life-cycle of poly (lactic acid) and its molecular structure [29]*

A disadvantage of PLA is its thermal instability [27], which makes its industrial processing a challenging task, especially during the printing process: indeed, thermal degradation of PLA occurs and reaches its maximum rate at temperatures higher than about 330 °C [27, 30, 31], leading to detrimental effects on the final scaffold product, and a difficult step for the correct scaffold preparation. Another discrepancy of the pure polymer scaffold with respect to the bone is its poor flexibility and relatively low biological activity [27], thus requiring some modifications in order to be an interesting candidate for this application.

To do so, we decided to join the biodegradability properties of PLA with hydroxyapatite ($Ca_{10}(PO_4)_6(OH)_2$). The latter, is a mineral whose characteristics fit very well in this situation, also considering the intrinsic presence in bone itself. With that, the addition of this component in the scaffold structure is made to improve biocompatibility by favoring the cellular adhesion, possibly acting as site for cells to attach to [32–35]. To control the structure of the produced polymer, in particular its random occurring structure during the reaction, we decided to more specifically utilize poly-(l)-lactic acid (PLLA), a derivate of the general PLA, where the polymerization process is controlled in order to obtain a polymer chain which is mostly linear, with very few ramifications. Furthermore, high-molecular weight PLLA can be produced in order to improve the preservation of its mechanical properties over the long period of time.

The composite has been then prepared as a matrix of PLLA in which hydroxyapatite is dispersed as small particles, due to their difficulty in solubilizing [36, 37]. In the long term,

then, PLLA would be able to degrade and leave only hydroxyapatite behind, which due to its natural presence in the bone shall be unharmful to the human body.

As **Tab. 2** shows, some tests have already been done with PLLA/hydroxyapatite composite, by using for example FDM as printing technique. The category of printing we focused on this thesis revolves around the so-called Electrostatic Fiber Drawing Techniques (EFDT). Our aim in this regard has been to increase the quality and reduce the filament thickness by utilizing this kind of special printing. Conceptually, a polymer or similar material is melted in a syringe-like container and gets extruded on a plane using electrostatic forces. One of the most common techniques is the Melt Electrospinning printing: here, the electric field induces the filament to, indeed, 'spin' and produce randomly oriented filament structures. As porosity and pore size properties play an important factor in the scaffold, this parameter cannot be regulated with this technique. To specify the above-mentioned property and still exploit the advantages of EFDTs, Melt Electro-Writing (MEW) technique has been used instead [6, 38, 39]. This is an electro-hydrodynamics-guided additive manufacturing technology to create high-fidelity constructs [27]. Specifically, this work revolved around the use of a self-assembled electrohydrodynamic guided melt electro-writing machine. The printing process is based on melting the material in a similar way of the Fusion Deposition Modelling (FDM), where the material is then pushed through the needle via pressure. MEW, though, is able to surpass the traditional methods by reducing the scale at which the work is done by increasing the precision of the printed structure, emphasizing the role of the scaffold geometry; as a downside, though, is the limitation in size (in particular thickness) of the printable projects.

As operating principle of MEW is concerned, at the tip of the needle the fused material accumulates and, due to surface tension, a bubble-shape fuse (now slowly cooling) remains attached to the tip. In order to overcome this physical effect and properly start printing, an electric field is used to generate a potential difference between the anode (print bed) and the cathode (syringe nozzle). As the force exerted by the electric field increases, the shape of the bubble gets deformed and eventually the two tensions will get to an equilibrium state, forming a cone-like shape, called *Taylor cone*. By further increasing the voltage, a threshold can then be reached, where a jet of liquid is emitted from the cone (*cone-jet*). From this moment, more and more of the melted polymer is able to flow down to the bed in a controlled way, which makes possible, in combination with the printing speed, to tweak the thickness of the printed

thread. Furthermore, the speed at which the plane moves can influence the shape with which the structure is printed, ranging from a line to a sinusoidal curve [40, 41].

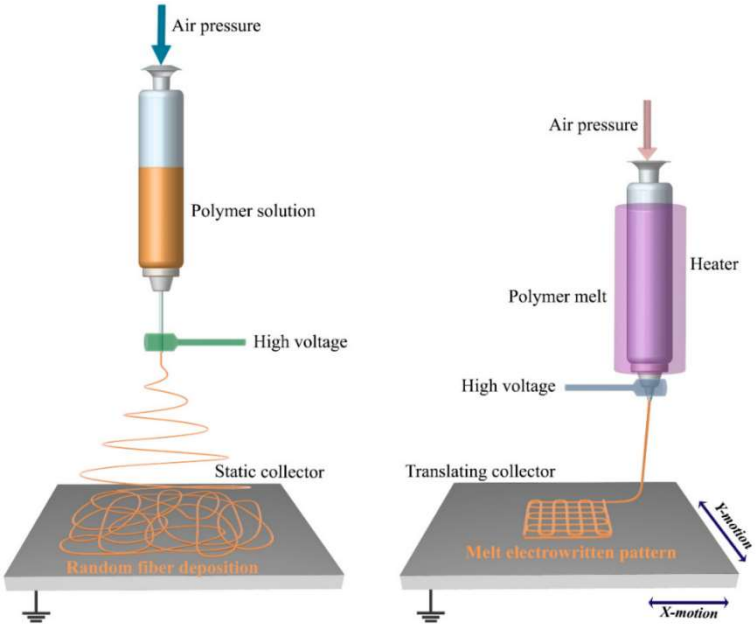

***Figure 13**: Melt electrospinning and melt electro-writing printing techniques [42]: while the first is able to print electrospun filaments, MEW improves scaffold precision by moving the collector accordingly during printing, thus making a regular and modulable structure*

To improve the printing quality of the MEW scaffold, different parameters can be modified:

- Voltage: adjusting the electric field accordingly helps the printing process to maintain a good quality during time: indeed, the dropped amount of material on the scaffold is heavily dependent on a proper tweaking of the voltage, to ensure a similar amount of fused material being dropped, as well as constantly leave behind the desired structure during the whole process.
- Temperature: depending on the material used for printing, the temperature of the heating chamber must be properly set. Reaching a temperature slightly higher than the melting temperature of the material is a requirement to be satisfied. The temperature has to be maintained uniformly in the syringe, all the way to the nozzle and its tip, and must not be much higher than the melting temperature of the material: if the temperature is too high, degradation would occur too quickly, thus making the melt not suitable for printing in a longer period of time and resulting in a bad quality structure and filament.

- Distance between the nozzle and the bed: this is a straightforward procedure that helps us find a fitting position in terms of height. This is to ensure the effective influence of the electric field on the molten material, promoting its adhesion to the bed. If the distance was too short, excessive intensity of the field might cause the melt to escape too rapidly from the nozzle, which can cause empty spots in the print due to the lack of material. On the other hand, if the tip of the needle were to be too far from the plane, the voltage required would not be enough to pull the filament towards the anode.
- Pressure inside the heating chamber: as for every 3D printing technique, there is the need to push or movement the material (in this case completely melted) towards and through the tip of the needle: by increasing the pressure, the melt is able to escape the cartridge and start printing. One important factor is the amount of material inserted into the: if the quantity is too low, increasing the pressure would allow the gas itself to move across the needle, instead of the melt, resulting in an inability to proceed with the printing.
- Needle size: this is a very important tool to succeed in the printing process, that also determines the filament size. Depending on the material that has to be printed, a too small needle diameter would not allow the escape of the melt from the tip, thus being unable to print. To overcome this problem, even a slight increase of diameter can allow the release of the melt from the needle.

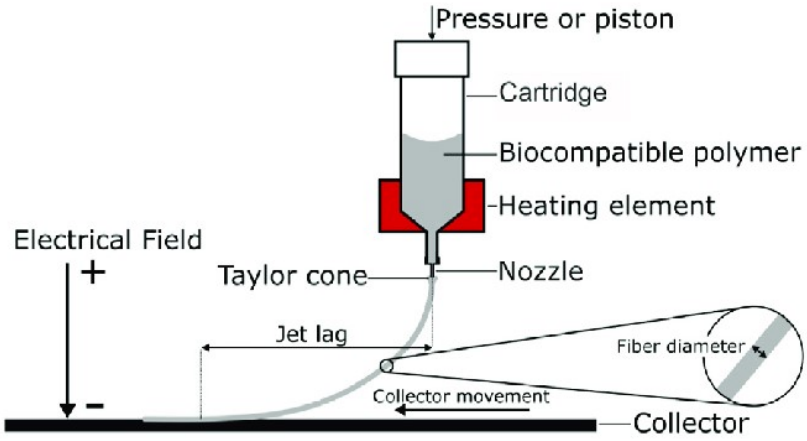

Figure 14: *Operation principle of melt electro-writing [40]: with the usage of pressure to movement the melted material, an electric field allows a filament to be released from the nozzle via a Taylor cone. Due to the movement of the collector, the position where the material is deposited will not be exactly perpendicular to the syringe but slightly delayed*

4.3. Acidity of PLLA

An important point that must be addressed for this composite is the acidic origin of PLLA and the possible implications when talking about degradation. Different studies have shown that during the degradation process PLLA influences the acidity of the environment near to it, thus reducing the pH of the system [30, 31, 43–46]. These kinds of applications that locally affect the natural environment of the body, may result more harmful than beneficial: a reduction in pH in the bone may result in the loss of activity of osteoblasts or even damage to the surface of the bone itself.

Studies of pure PLLA scaffold have shown different results, that vary between a small reduction of pH of some tenths of units and a few entire units. Scaffolds composed of both PLLA and hydroxyapatite, instead, have had a different behavior from the pure polymer: the release of acid degradation byproducts from the PLLA remain present, but the addition of hydroxyapatite allows the acidification process to be slowed down. In fact, the release of alkaline ions by the mineral component interacts with the acidic fraction, resulting in a neutral pH, if the amounts were stoichiometrically correct. Nonetheless, this property allows the net amount of acid release to be mostly controlled, thus having a smaller acidification effect and extensively reducing the possible issues around the implant area in the long term; even so, decreases of pH after several times from implant insertion can also be related to bone tissue ingrowth, which indeed achieves a good therapeutic effect [45].

4.4. Pore size effect

To improve cell proliferation, another important aspect is the development of a scaffold with appropriate characteristics that favor the diffusion, proliferation, and attachment of cells. In this regard, porosity and pore size play an important role. With the latter being easier to tweak when talking about MEW, studies show that a pore size between 100 and 500 µm is best [4, 47, 48]. With print quality and technical factors in mind, 200 µm pore size has been chosen for this research.

5. Material and methods

5.1. Materials

Chloroform (TCM, ≥99.0%, Wako), Hydroxyapatite nanopowder (Calcium hydroxy phosphate, < 200 nm particle size, ≥97%, Sigma-Aldricht), Poly-(l)-lactic acid (130000 MW, Musashino Chemical Laboratory Ltd.), Distilled water (Wako), Acetone (≥99.5%, Wako), Ethanol (EtOH, 99.5%, Wako).

5.2. Raw material preparation

Previous studies on PLLA/hydroxyapatite composite have used surfactants or other additives during the preparation of the material in order to simplify the homogenization and preparation process [15, 49]. Although this looks like a good alternative, the need to remove the above-mentioned additions from the composite before its application remain, which implies secondary steps downstream. Our choice on the preparation phase has been to avoid the use of additional components to simplify and make the process cleaner.

The raw material preparation was performed by weighing around 2.5 g of pure PLLA pellets, then weighing the corresponding amount of hydroxyapatite based on the composite that was being prepared (0.025 g for 1% wt., 0.125 g for 5% wt. and 0.25 g for 10% wt.).
The so weighted PLLA was transferred in a 50 mL vial where chloroform was added in excess amount, in order to completely dissolve the PLLA. The solution was mixed at 280 rpm and 40 °C for 4 hours using a magnetic anchor. The container was initially closed to ensure the correct dissolution of PLLA in chloroform without the latter able to evaporate and escape.
In a different 10 mL vial, hydroxyapatite nanopowder was dispersed in chloroform, filling it up to around 50% with the solvent. The sample was then put in a distilled water bath inside a bath sonicator (50/60 Hz, 80 W, Branson) and let it run for 4 hours, to allow a homogenous dispersion of the nanopowder.
The hydroxyapatite dispersion was transferred inside the PLLA solution vial under stirring, letting now the vial open to allow evaporation of the chloroform. To speed up the evaporation process and ensure the correct homogenization of the nanoparticles in the solution before

casting, the mixture was heated at 70 °C, and the stirring speed increased to 360 rpm. The latter was then mixed for 1 hour or until about half the chloroform was evaporated.

***Figure 15**: Images of the cast composite solution before and after drying at room temperature and pressure*

The resulting mixture was then cast in a Petri dish and let dry under ventilation chamber overnight at room temperature and pressure.

The dried composite thus obtained was cut into small rectangular-like pieces and then set drying in oven under vacuum conditions at 110 °C for 2 hours then at 80 °C for at least 6 hours. Each raw composite material was stored in a 50 mL vial.

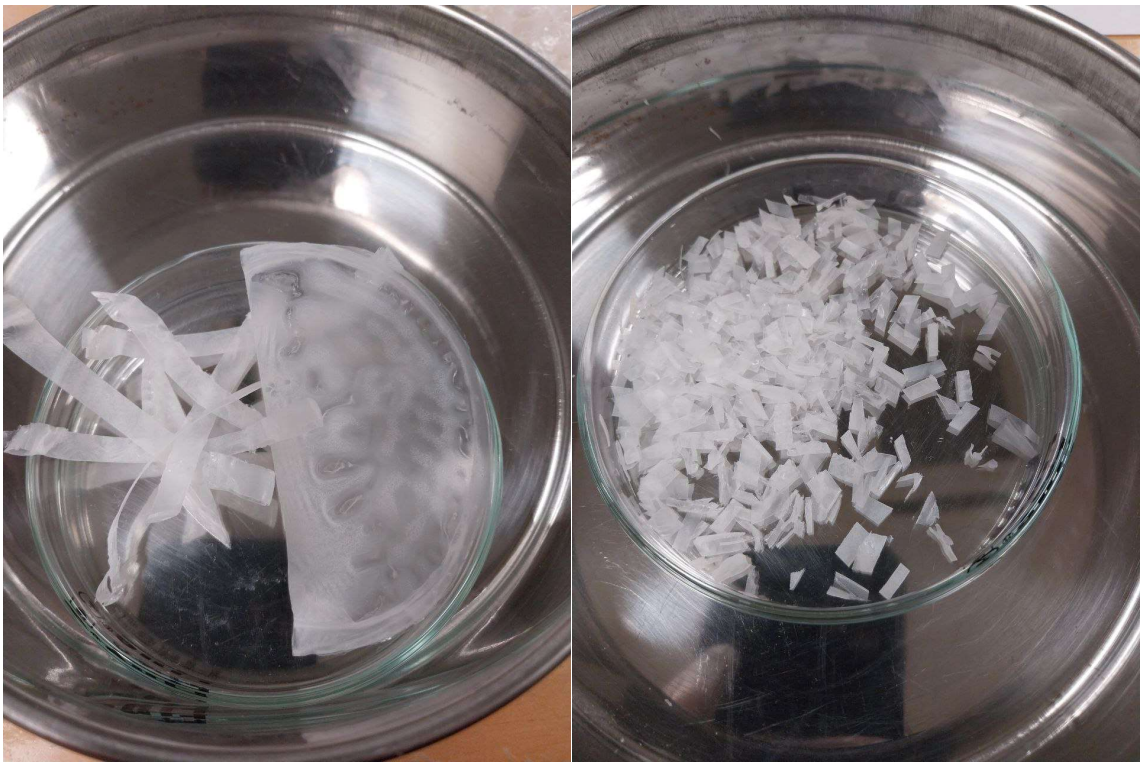

***Figure 16**: Images of the dried raw material during and after the cutting step*

5.3. Melt electro-written scaffold preparation

All the raw composite materials were then printed with MEW using a self-assembled electrohydrodynamic guided melt electro-writing machine described in the previous section and shown in **Fig. 17**. For every print, about 0.5 g of the raw material were weighed. The metal cartridge was previously soaked in chloroform solution to completely dissolve any residual from previous operations. After drying in oven at 80°C overnight, the raw material was inserted inside the cartridge, where a needle with a diameter of 0.12±0.03 mm was attached. The heating element was set to about 190°C, a temperature higher than the melting point of the composite, but not very far from it: this is done to reduce the degradation process, a phenomenon very much influenced by the temperature, that can reduce the quality of the scaffold; limiting this effect allows us to continue printing several scaffolds in one single printing session and maintain a good quality overall. After placing the syringe inside the heating element, the composite began to melt. The tip of the needle was set at a height of 1.5 mm from the collector bed, whose surface temperature was set at 80°C to avoid thermal shock of the filament once in contact with the plane, and guarantee its attachment to it. After 40÷60 minutes the composite was completely melt and the printing process was initiated. As both

the room humidity and temperature influence the result of the printing process, two parameters were manually adjusted for every printing session: (i) the pressure inside the chamber, used to move the melt along the cartridge syringe; (ii) the electric field, which allows the drop of material to be released from the tip of the syringe towards the plate. Each process was completed after printing between 5 and 20 scaffolds. The above-mentioned parameters were kept approximately constant during the different printing sessions of the same raw material.

The scaffold structure was programmed via a .csv file, that defined the movement of the plane during the print, and so the geometry of the scaffold. Here, different settings are possible to be modified; the most important ones are the following: (i) printing speed, affects the deposition of the melted material and the thickness of the fiber; (ii) scaffold geometry, both the number of horizontal and vertical passages, the number of layers and length of each line can be changed to generate different shapes; (iii) number of scaffolds print in the session, as depending on the composite being printed, concurrently with the degradation properties of the latter, more or less scaffolds are able to be printed by maintaining a good quality.

The scaffolds printed for all the tests (excluding the mechanical ones), consist in a square grid with a passage between each filament of 200 µm (pore size), 25 horizontal and vertical lines, 25 layers, and 1cm^2 in total. The mechanical test scaffold geometry, instead, consists of a rectangular grid with a passage between each filament of 200 µm, 10 layers, and 2.4cm^2 in total.

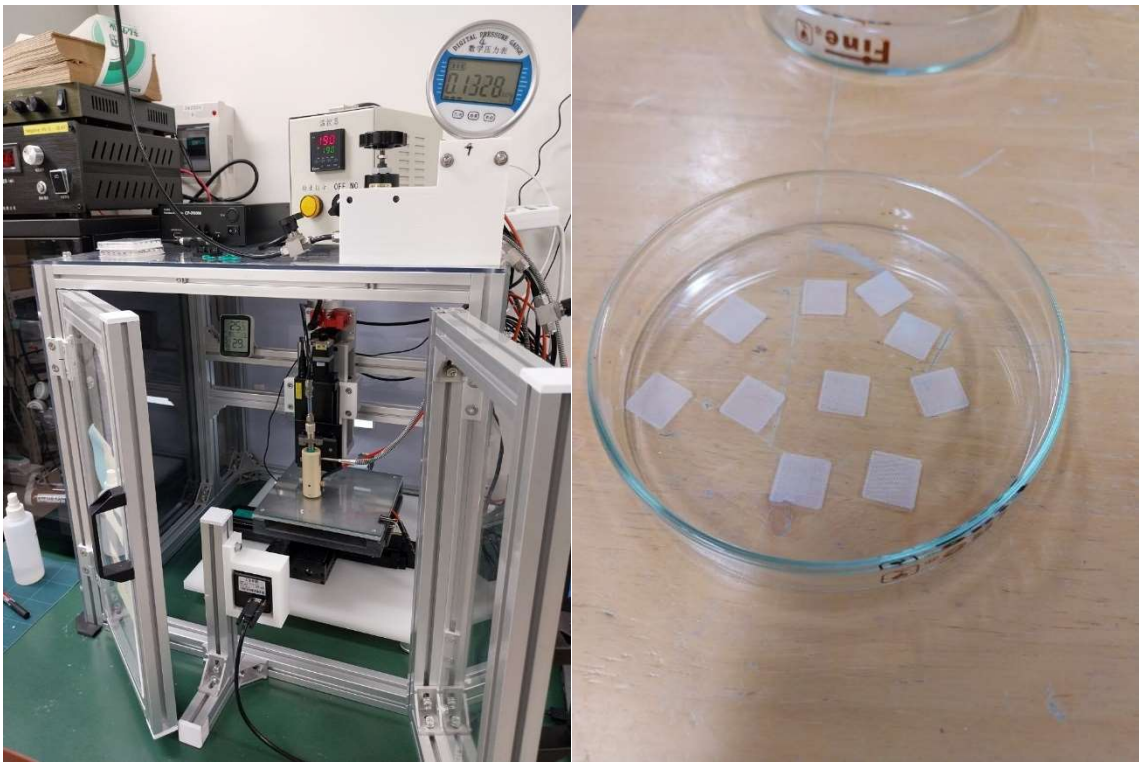

***Figure 17**: On the left, the melt electro-writing machine utilized in this thesis research; on the right, the melt electro-written scaffolds produced with this technique*

5.4. Composite characterization

5.4.1. Morphology characterization techniques

Laser microscope

3D laser-scanning microscope (VKX200K series, Keyence, Osaka, Japan) was used with the melt electro-written scaffolds to verify the result of the printing process and its quality, in terms of both regularity of the structure and diameter of the thread along the scaffold. For all composites a 10x magnification image was taken. For some of them, other magnification images were also taken to further visualize the filaments and the geometry (20x, 50x, 100x).

Scanning Electron Microscopy

Scanning Electron Microscope (SEM) (SM-7001F, JEOL, Tokyo, Japan) was used to obtain high magnification images of both the hydroxyapatite nanopowder and the melt electro-written scaffolds. The latter were sputter-coated with a layer of platinum before being measured with SEM at an accelerating voltage of 15 kV. Every time, at least three images per magnification were taken. Scaffolds with different hydroxyapatite concentration (0%, 1%, 5% and 10% by weight) were run through SEM machine, and images at different magnifications were taken, specifically at 100x, 250x, 500x and 1000x magnification. For each scaffold, at least 3 different locations were explored.

5.4.2. Non-destructive chemical techniques

Contact Angle

Contact angle machine was used to evaluate the wettability of the scaffold surface. The samples were put on a lab slide for testing. By using a mechanically operated syringe, a drop of distilled water was deposited on the surface of the scaffolds. With the use of a camera, the contact angle of the drop was measured, and multiple readings have been recorded every time: each scaffold was tested for contact angle 4 times, and each test resulted in 15 different data sets. For each test, an average of the different contact angles was obtained, and a standard deviation calculation was performed. All the results were then gathered to analyze the behavior of the composite scaffolds in regard to water affinity, with the change of hydroxyapatite content. The pure PLLA scaffold was also analyzed with this technique.

FT-IR

FT-IR analysis (IRAffinity-1S, Shimadzu Corporation, Kyoto, Japan) was used to analyze the composition of pure components and scaffolds in a spectral region between 300 and 4000

nm. Before every analysis, the sample holder and the complementary ATR were cleaned with acetone. Hydroxyapatite nanopowder was analyzed by putting a small amount of powder in the holder and slowly screwing down the pin. A single PLLA pellet was crushed and put in the holder for analysis. The scaffold was put above the container and firmly pinned down with the top pin, to ensure the intimate contact with the parts and the correct signal response. For each sample, a background spectrum was captured beforehand. This way, the subsequent readings were already clean of the disturbing signal. Every sample was measured at the FT-IR at least three times. LabSpec software was used to make the baseline correction and the Origin program for plotting.

Raman

Raman microspectroscope (RAMANtouch, Nanophoton Co., Minoo, Osaka, Japan) was used in the 300 ÷ 4000 cm^{-1} spectral region with a 10x, 50x and 100x magnification lens, with nominal aperture of 0.30 (10x), 0.80 (50x) or 0.90 (100x). Imaging method was performed using a green (532 nm) laser with a power of about 92 mW, using an exposure time of 5 s and averaging 2 measurements; grating of 300 gr/mm. Mapping method was also performed, using a green (532 nm) laser with a power of about 13 mW, using an exposure time of 1 s and averaging 10 measurements; grating of 300 gr/mm.

LabSpec software was used process the data. Processing has been performed through baseline correction and smoothing (whenever necessary), while Origin program was implemented for peaks normalization. If unintended glass bands from the lab slide were captured by the Nanophoton, CaF_2 disks (OptoSigma, SigmaKoki) were used instead. All the scaffolds were analyzed using at least 10x and 100x magnification. In particular, 10x magnification was used to obtain an image of the raw materials, the scaffolds, and for the mapping analysis; 100x magnification was used to analyze a single thread section of the scaffolds and evaluate the distribution of hydroxyapatite along the print.

EDS

Energy-Dispersive X-ray Spectroscopy was performed in conjunction with SEM to evaluate presence and distribution of elements on the scaffolds (0%wt., 1% wt., 5% wt., 10% wt.). In the EDS analysis, Carbon, Oxygen, Phosphorus and Calcium elements have been chosen to be detected in the scaffolds. Specifically, phosphorus and calcium are supposed to be only due to the presence of hydroxyapatite ($Ca_{10}(PO_4)_6(OH)_2$). The samples were treated for the SEM analysis as described before, and put inside the scanning microscope, where a high intensity surface scanning setting was used to enhance the detection of the different elements inside the scaffolds. Each print was analyzed with EDS at least three times in different locations.

XRD

Ultima IV X-Ray Diffractometer (Rigaku Co., Ltd.) was used to evaluate the degree of crystallinity of the raw materials and scaffolds. Each hydroxyapatite percentage specimen, as well as pure PLLA, was put on a sample holder and fixed with a double-sided tape. After inserting each analyte in the instrument, the analysis was initiated via the instrument software, and run in a range of 2θ between 3° and 70°. Graphs were obtained for both the raw materials and the scaffolds to determine if there was any change in crystallinity post-printing due to the re-heating and extrusion process, as well as with the change in hydroxyapatite concentration. Data fitting was done with LabSpec program, while the graphs were elaborated using Origin.

5.4.3. Destructive chemical techniques

Differential Scanning Calorimetry

Differential Scanning Calorimetry (DSC) analysis was performed once for each raw material before printing (0%wt., 1%wt., 5%wt., 10%wt.) to evaluate the melting point and its possible change with the change of hydroxyapatite content. For every test, about 0.002 grams of the

raw material were weighted and put in an aluminum sampler. The latter was then covered with a thin aluminum disk, after which the borders were bent on itself to ensure the specimen would not escape during the test. During the whole process, a constant flow of 25 mL/min of N_2 was sent in the machine chamber. The temperature was set to rise by 10 °C/min until a maximum value of 300 °C. An empty aluminum sampler was used as reference. The data was recorded, and the melting point was defined as the temperature corresponding to the minimum value of DSC (mcal/s) of the melting curve. Plotting was done using Origin program.

TGA

Thermo-Gravimetric Analysis was performed on all scaffolds. Each square sample was cut, and only a quarter was inserted inside the sample holders due to their size and weight. The holding plates were firstly cleansed by heating them with a torch and, after cooling, each scaffold was put inside a holder. The test was set to a temperature increase of 10 °C/min with a maximum temperature of 600 °C. Equilibration was set to 40°C. The weight of each scaffold at the beginning and at the end of the test was used to evaluate the real amount of hydroxyapatite that was present in each composite, as by reaching 600 °C all the polymer has been assumed removed, and the only remaining component was the nanopowder. The temperature at which the reduction in weight reached 10% (90% of the initial weight value) has been defined as the onset degradation temperature. Origin program was used for plotting.

5.4.4. Mechanical tests

Tensile testing machine was utilized to obtain the mechanical properties of the different scaffolds (0%wt., 1%wt., 5%wt., 10%wt.). For this test, a 4x0.6 mm scaffold was attached to a paper holder with a window of 2 cm. The prints were immobilized on the holder using a double-sided tape, and sandpaper was attached on the other side of the tape to further avoid the movement of the scaffolds during the test. The mechanical test was done with a movement of the upper clamp of 10 mm/min, and for every sample the weight value of each scaffold was adjusted in accordance with the previously taken weighings. The test was stopped after the snapping of the sample. For each different concentration scaffold, multiple

tests were conducted, and an average of the maximum strength was obtained. Other parameters like strain, elastic module and toughness were calculated using Origin and Excel programs. In particular, strain was defined as follows:

$$\varepsilon = \frac{\Delta L}{L_0} = \frac{L - L_0}{L_0}$$

Where ΔL is the difference between the initial length (L_0) and current length (L). Elastic module was calculated as the tangent of the tensile test diagram between 0.18% and 0.20% strain, a region where the stress-strain curve resulted constant for all the different samples. Toughness value, instead, was calculated as the integral of the curve up to the snapping point, which corresponds to the maximum strength value.

5.4.5. Biological techniques

Cytotoxicity

All instruments used in this technique used were sterilized with a 70% ethanol solution. The culture media was prepared with the following concentrations: 10% FBS (Fetal Bovine Serum) (Sigma), 1% MEM (Minimum Essential Medium) nonessential amino-acid solution (Naquai Tesque), 1% L-sodium pyruvate (Naquai Tesque), 1% Antibiotic (Penicillin-Streptomycin) (Naquai Tesque), 87% DMEM (Dulbecco's Modified Eagle Medium) (High Glucose). The culture media and the Phosphate-Buffered Saline (PBS) solution were heated up in a water bath up to 37 °C. The immobilized cell culture (HDF22, Human Dermal Fibroblast) was kept in incubator at 37 °C in a 5% CO_2 atmosphere. Two Immobilized Cell Culture (ICC) Petri dishes were used for the Cytotoxicity test. The ICCs were washed two times with PBS, and every time the culture media and PBS solution were removed via vacuum pump. 6 mL of Trypsin were then added to each Petri dish to detach the cells. The cultures were put in incubator for 5÷7 minutes or until the detachment was confirmed by observation with optical microscope. In this phase, the detached cells form agglomerates. In each dish, 6 mL of pure culture media were then added to block the Trypsin detaching effect. Both mediums were then collected in two different Falcon vials and put in centrifuge for 5 minutes at 1000 rpm: this way the cells deposit at the bottom of the vial, while the solution of Trypsin and culture media stay on the top. The latter

was then removed from the Falcon, leaving only the cells. 5 mL of fresh culture media were then added to both samples and mixed with the cell agglomerate. 10 µL of solution were mixed with 10 µL of Trypan Blue solution and put in a cell counter container, which was then used in a cell counter machine to obtain the concentration of cells in the solution (cell/mL). From the results of the instrument, calculations were done in order to obtain 10 mL of a 200000 cells/mL solution. To do so, fresh pure culture media solution was used for dilution.
A 24-well plate was used for the incubation process, and each of the following samples were tested in 4 copies:

- Pure culture media: 1000 µL.
- Only cells culture: 100 µL of 200000 cells/mL solution (20000 cells) with 900 µL of culture media.
- Pure PLLA scaffold: sample immerged in 100 µL of 200000 cells/mL solution (20000 cells) with 900 µL of culture media.
- 1%wt. hydroxyapatite scaffold: sample immerged in 100 µL of 200000 cells/mL solution (20000 cells) with 900 µL of culture media.
- 5%wt. hydroxyapatite scaffold: sample immerged in 100 µL of 200000 cells/mL solution (20000 cells) with 900 µL of culture media.
- 10%wt. hydroxyapatite scaffold: sample immerged in 100 µL of 200000 cells/mL solution (20000 cells) with 900 µL of culture media.

Two sets of the above-mentioned plate were made and incubated for 24 h and 72 h respectively. Bright field images after incubation were taken with an optical microscope. Fiji program was used for image contrast adjustments. After incubation, all the wells were treated with WST solution and then undergone the WST-8 cytotoxicity test: this is a colorimetric technique that allows to determine the number of viable cells by changing the color of the medium: if the cells are alive, the medium would result orange, while if the cells are dead, the medium would remain as a purple colored solution. For each well, two 100 µL of the resulting solution were then taken and put in a 98-well plate, where absorbance readings were taken with the infiniteF50 instrumentation. The data obtained was then analyzed using the Origin program, where all the results were done by defining the absorbance of the pure culture media sample as maximum value. Standard deviation and error% calculations were also performed.

Acidity Test

To better understand how composite degradation affects the pH of the nearby environment, an 'acidity test' has been performed to assess this issue. In a 10 mL Falcon vial, 6 mg of raw composite material (1%wt., 5%wt., 10%wt.) were added to 6 mL of culture media solution (same preparation as the cytotoxicity test). The pH of the solutions has been monitored for a total of 365 hours. Each sample was stored, and three copies have been done for each different raw material, as well as the control solution (pure culture media). pH evaluation has been done with a standard pH meter, where calibration was performed every time before reading. Intervals between each reading varied over time. Origin program was used for plotting.

6. Results

In our work, we prepared four different raw materials and scaffolds with different concentration of hydroxyapatite (0%wt., 1% wt., 5% wt., 10% wt.). To do so, we dispersed PLLA and hydroxyapatite in chloroform in two different vials, this process has been done to allow a better homogenization and dispersion of the 2 components in the solvent. The dissolution of PLLA in chloroform has been done simply by stirring with a magnetic anchor, since the chlorinated solvent is ideal for dissolving the biopolymer [6, 15, 29, 50]. On the contrary, the nanopowder has been dispersed in chloroform via the use of a bath sonicator: this was done since the latter is not optimal for its dispersion via simple agitation. For this reason, a higher power is necessary to de-aggregate the nanoparticles of hydroxyapatite in the medium and obtain a homogeneous dispersion without big aggregates. When the two vials are mixed to obtain the composite mixture, the stirring speed has been increased to ensure a better mixing, and the temperature raised to 70°C to ensure a lower viscosity of the resulting solution. This was done since a too high viscosity would have caused formation of stagnant areas inside the vessel, as well as making the casting process more difficult.
The two materials were then combined into three composites:

- PLLA with 1%wt. of Hydroxyapatite (PLLA-1%).
- PLLA with 5%wt. of Hydroxyapatite (PLLA-5%).
- PLLA with 10%wt. of Hydroxyapatite (PLLA-10%).

That were used to produce four different scaffolds:

- PLLA with 0%wt. of Hydroxyapatite (MEW-0%).
- PLLA with 1%wt. of Hydroxyapatite (MEW-1%).
- PLLA with 5%wt. of Hydroxyapatite (MEW-5%).
- PLLA with 10%wt. of Hydroxyapatite (MEW-10%).

6.1. Morphological characterization

Optical laser microscopy and SEM images of the four different scaffolds were acquired to evaluate the quality of the printing. From **Fig. 18** it is possible to see how the morphology changes as a function of hydroxyapatite concentration. The images show that the higher the amount of hydroxyapatite, the less precise the morphology of the scaffold. This might be caused by mainly two factors: (i) as hydroxyapatite is a poor conductor material, its presence

inside the composite influences the electric field used during the melt-electro writing process, reducing the effect of it in making a good quality Taylor cone and cone-jet, thus directly affecting the quality of the print; (ii) by adding this nanopowder inside the polymeric matrix, the resulting material becomes more irregular and less homogeneous, as the PLLA chains are hindered by the hydroxyapatite, furthermore changing the viscosity and density of the so crafted composite. Another important phenomenon that generally occurs during this print is the resistance effect of the scaffold on the applied voltage, where the further in the print of each scaffold (and so the higher the layer that is being printed), the less the effect of the electric field, that results in a reduction in quality of the cone-jet if not controlled. By increasing the amount of hydroxyapatite, its presence further affects the electric field, resulting in a more dragged filament, with a decrease in regularity of the print, that can degenerate in an electrospun structure.

SEM images also reflect this behavior (**Fig. 18**) where a thicker and disorganized patternis formed with the increase in hydroxyapatite concentration. A possible solution to both phenomena could be to automatically adjust the intensity of the Electric field during the print of each scaffold (as for each printing session more than one scaffold was printed in succession): this way we could have optimal printing conditions among the print, which should directly result in a better quality of the scaffold overall. Although interesting, this solution resulted to be very complicated, as the instrumentation that was used to generate the electric field did not have an automated voltage source.

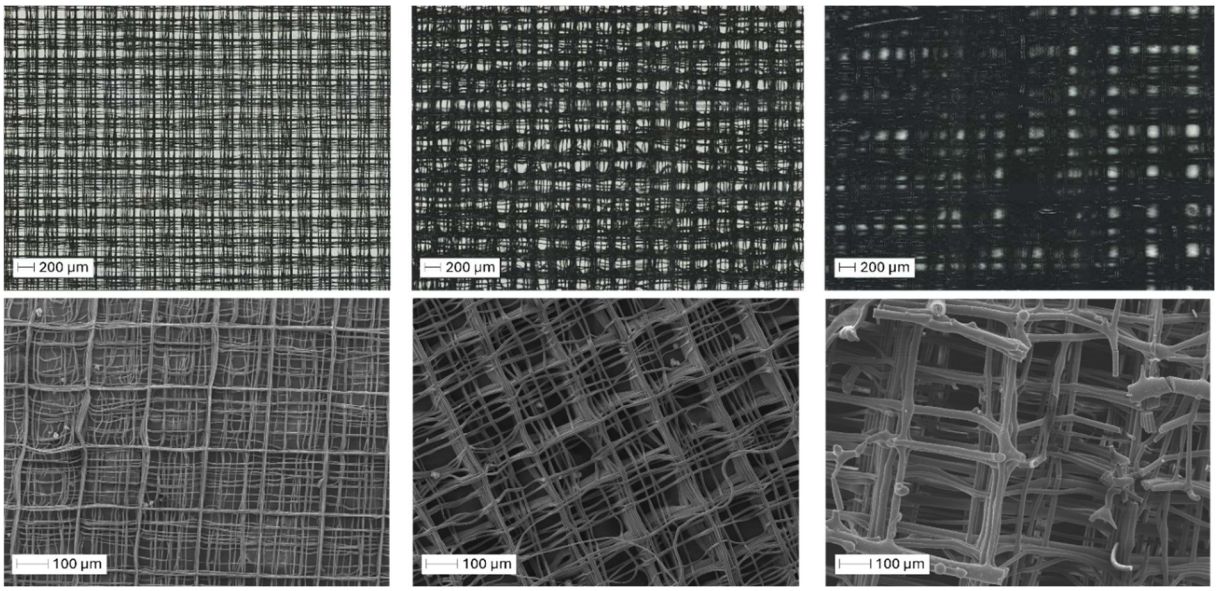

***Figure 18**: Laser microscope images (upper row) and SEM images (bottom row) of the three composite scaffolds. From left to right: MEW-1%, MEW-5%, MEW-10%*

6.2. Non-destructive chemical characterization

Contact Angle

Contact angle analysis was performed to assess the wettability of the scaffolds. This property is fundamental when talking about the interaction between the material and the surrounding biological environment, where the property of hydrophilicity or hydrophobicity regulates cellular adhesion and colonization. The hydroxyapatite-containing scaffolds were compared in terms of wettability to the pure PLLA scaffold to analyze any behavior with the change in composition.

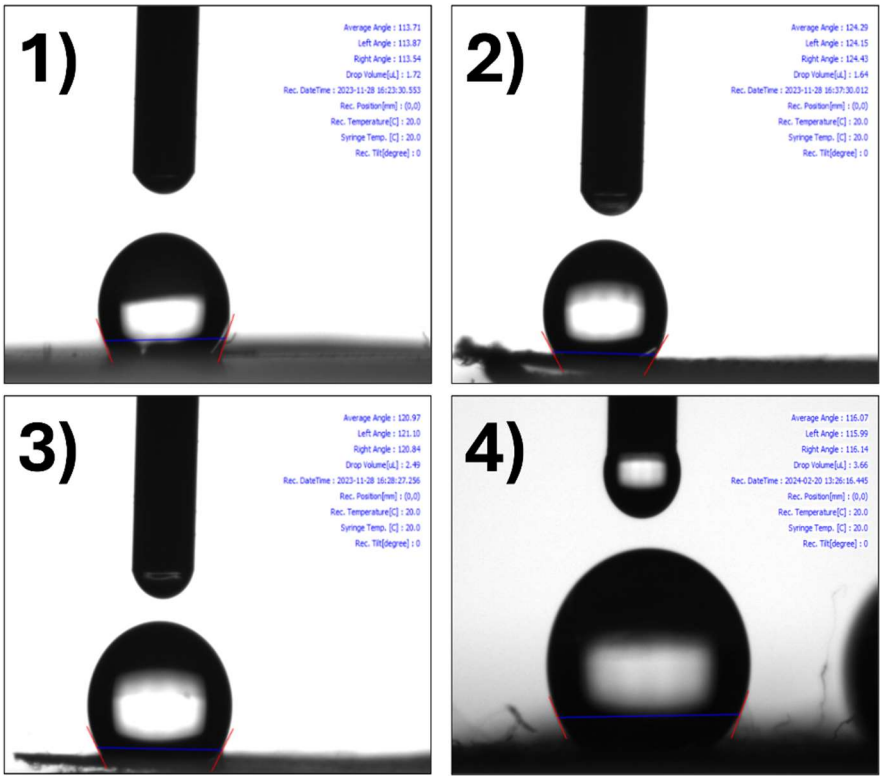

***Figure 19**: Contact angle analysis of 1) MEW-0%, 2) MEW-1%, 3) MEW-5% and 4) MEW-10%*

Fig. 19 shows contact angle images of the different samples: although an initial reduction in hydrophobicity can be seen with MEW-1% (**Tab. 3**, **Fig. 20**), the contact angle value seems to steadily increase with the increase of hydroxyapatite in the scaffolds.

Table 3: Contact angle results of the different scaffolds

Sample	Average (°)	Standard Deviation
MEW-0%	117.64	4.56
MEW-1%	115.03	4.91
MEW-5%	123.77	2.16
MEW-10%	128.61	9.77

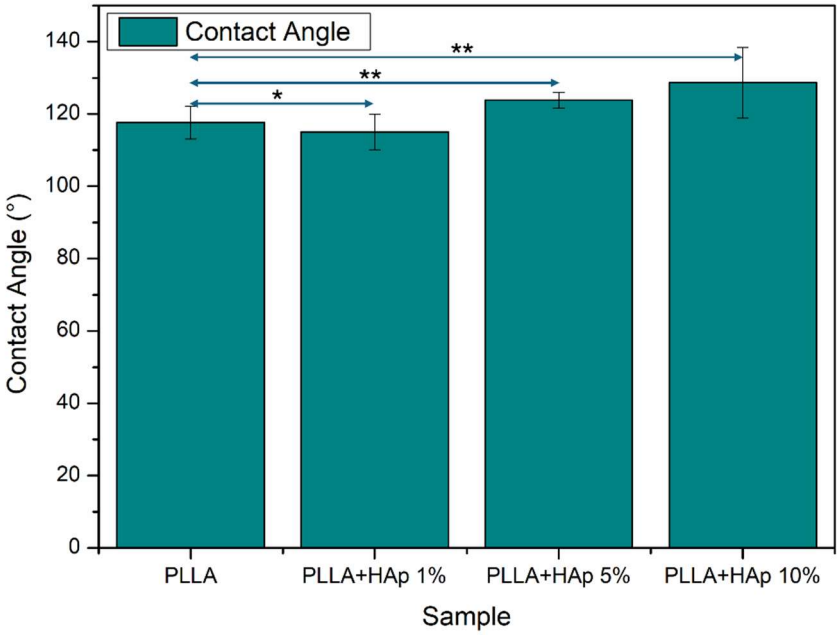

Figure 20: Results of contact angle analysis on the different scaffolds

FT-IR

FT-IR measurements were performed to evaluate the chemical composition of the scaffolds. For comparison, FTIR analyses were also performed with hydroxyapatite nanopowder and pure PLLA pellet to have the spectra of the pure components. After obtaining the base spectra, the analysis was performed on the scaffold samples to confirm the presence of hydroxyapatite and monitor its peaks with the change in concentration. **Fig. 21** reports the spectra of the pure components, as well as MEW-1%. PLLA shows both the O-H bond at 3300÷3700 cm^{-1} and the $-C = O$ stretching at 1700÷1760 cm^{-1}, as found in literature [51]. For hydroxyapatite, instead, the following peaks are present[52]:

Table 4: Main bands observed on the hydroxyapatite spectrum of Fig. 21

Position (cm^{-1})	Vibration	Citation
560	PO_4^{3-}	[53, 54]
600	PO_4^{3-}	[53, 54]
630	HPO_4^{2-}	[53, 54]
1000÷1100	PO_4^{3-}	[53, 54]
1460÷1530	CO_3^{2-}	[53, 54]

Fig. 21 shows an overlapping of the stronger peak of hydroxyapatite with the one of PLLA, which results in a difficulty of discriminating the two components in the composite spectra. This is confirmed with the MEW-1% spectra: this highlights signal overlapping between the two phases, and due the relatively low fraction of hydroxyapatite, it is concluded to be not possible to determine the correct presence and amount of the nanopowder in the scaffold with this technique.

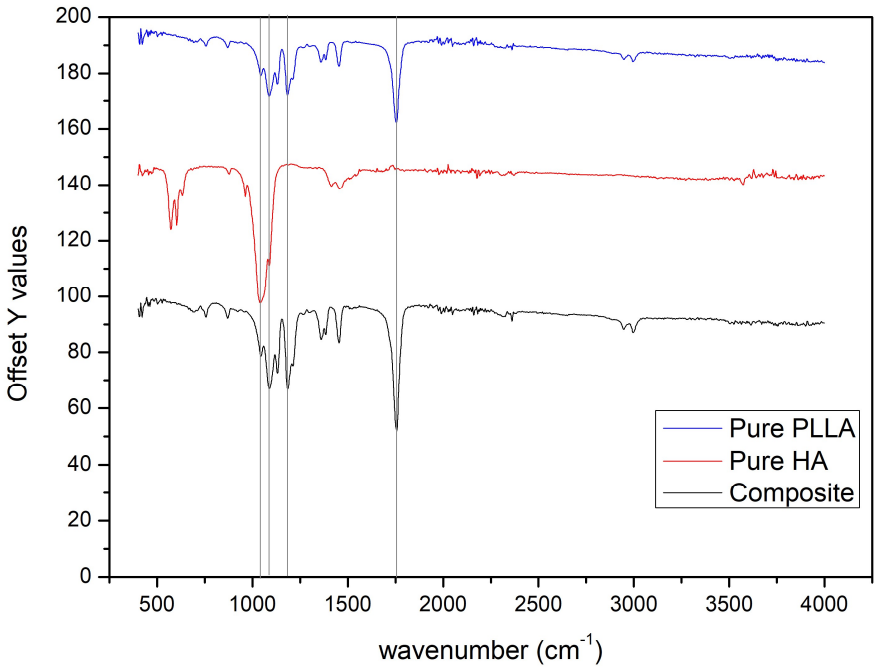

Figure 21: FT-IR spectra of the pure components and the composite scaffold. Starting from the top: pure PLLA, pure hydroxyapatite nanopowder, MEW-1%. Vertical dotted lines show the main peaks' position of the two base materials

Raman

Fig. 22 shows the obtained spectra for pure hydroxyapatite nanopowder and PLLA:

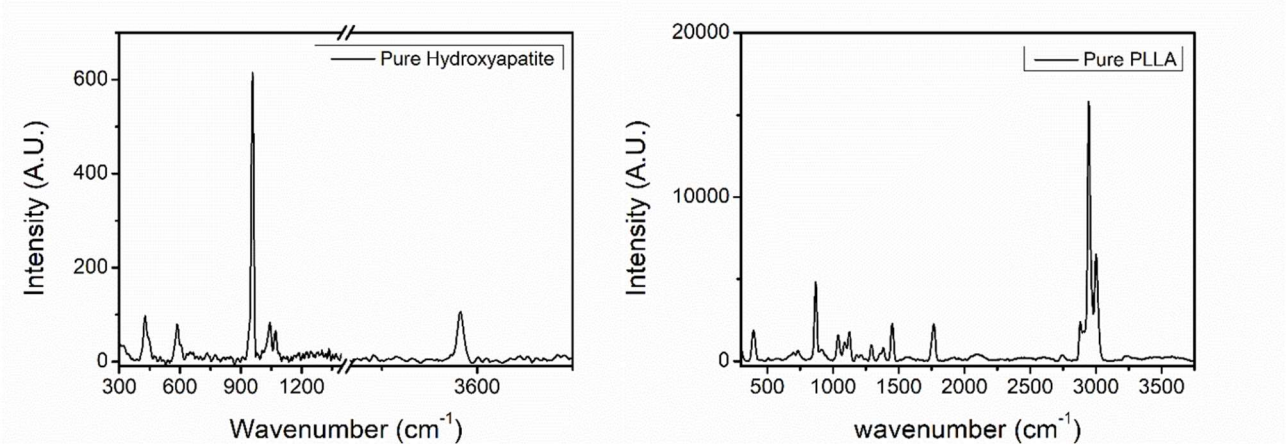

***Figure 22**: Raman spectra of the two base materials. On the left, pure hydroxyapatite nanopowder; on the right, pure PLLA*

The following peaks for hydroxyapatite can be observed in the spectrum:

Table 5**: Main bands observed on the hydroxyapatite spectrum of **Fig. 22

Position (cm^{-1})	Vibration	Citation
430 ÷ 450	$\nu_2\ PO_4^{3-}$	[55, 56]
585 ÷ 610	$\nu_4\ PO_4^{3-}$	[55, 56]
960	$\nu_1\ PO_4^{3-}$	[55, 56]
1020 ÷ 1080	$\nu_3\ PO_4^{3-}$	[55, 56]
1070	$\nu_1\ CO_3^{2-}$	[55, 56]

For the pure PLLA the following peaks can be seen instead:

Table 6**: Main bands observed on the PLLA spectrum of **Fig. 22

Position (cm^{-1})	Vibration	Citation
398 ÷ 411	δCCO	[57, 58]
875	$\nu C - COO$	[57, 58]
1452	δCH_3	[57, 58]
1750	$\nu C = O$	[57, 58]
2878	$\nu_s CH3$	[57, 58]
2923	$\nu_{as}CH_3$	[57, 58]
2950	νCH	[57, 58]

By comparing the two spectra, 960 cm^{-1} was chosen as representative wavenumber for hydroxyapatite presence inside the sample, as no PLLA peaks are detected in those surroundings.

PLLA-1%, PLLA-5% and PLLA-10% were then analyzed and compared to the pure PLLA. **Fig.23** shows the four mapping spectra thus obtained: it can be seen that the peak at 960 cm^{-1} is the only visible peak for hydroxyapatite and, as expected, is steadily more intense the higher the concentration.

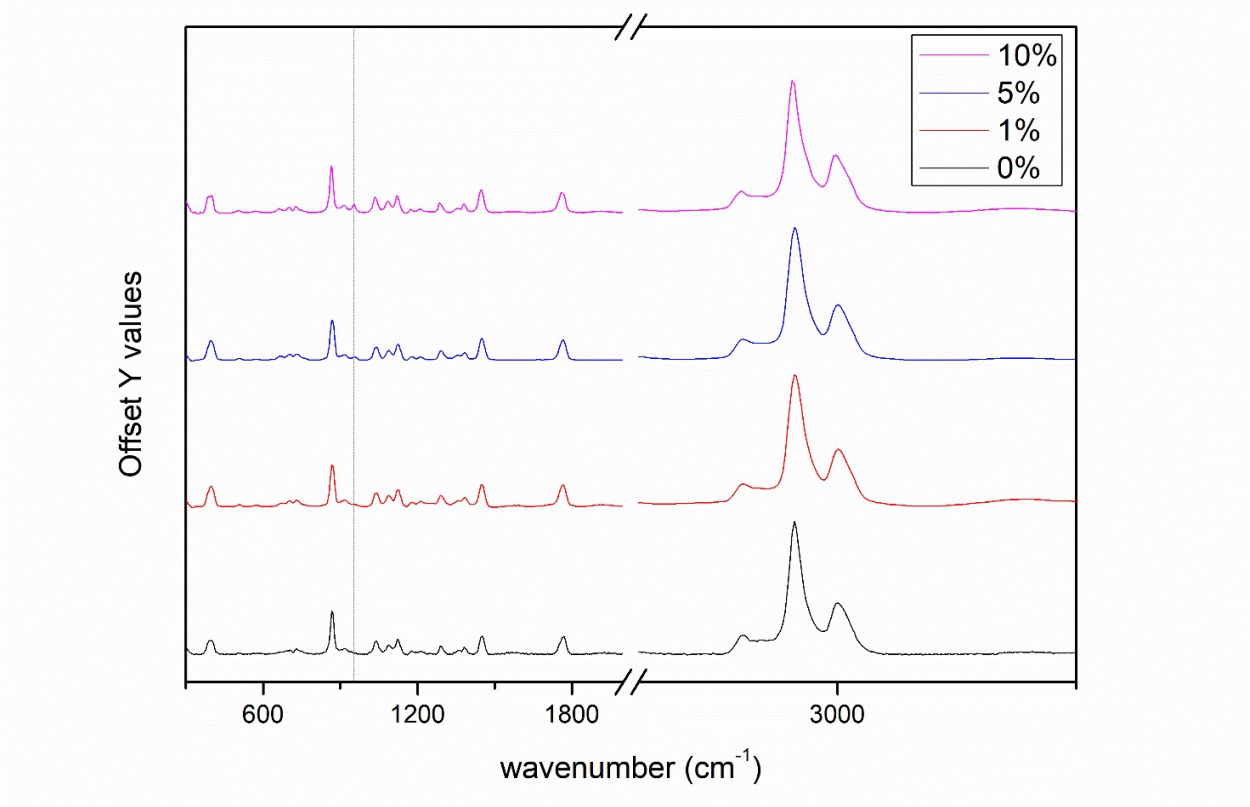

***Figure 23**: Average Raman spectra of the different raw materials, as function of concentration of hydroxyapatite (from bottom to top). The vertical dotted line highlights the Raman band at 960 cm^{-1}*

A proportionality fitting at 960 cm^{-1} was calculated to check the increase of concentration of hydroxyapatite component inside the composite, which confirmed the expected proportionality **(Fig. 24)**.

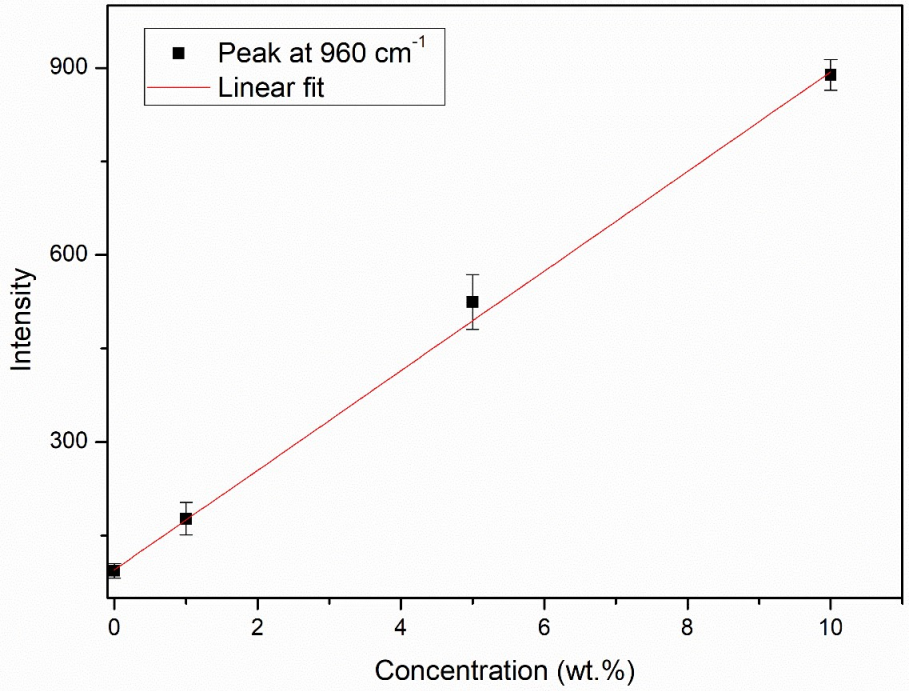

***Figure 24**: Intensity of the Raman band at 960 cm^{-1} on the raw materials as function of hydroxyapatite concentration.*

Raman imaging was used to observe the distribution of the hydroxyapatite in the polymeric matrices, using the peaks at 875 cm^{-1} for PLLA (red) and 960 cm^{-1} for hydroxyapatite (green). Raman imaging uses a 400 pixels linear sensor, resulting in high-resolution chemical maps of the surfaces. **Fig. 25** shows the three different composite raw materials at 10x magnification.

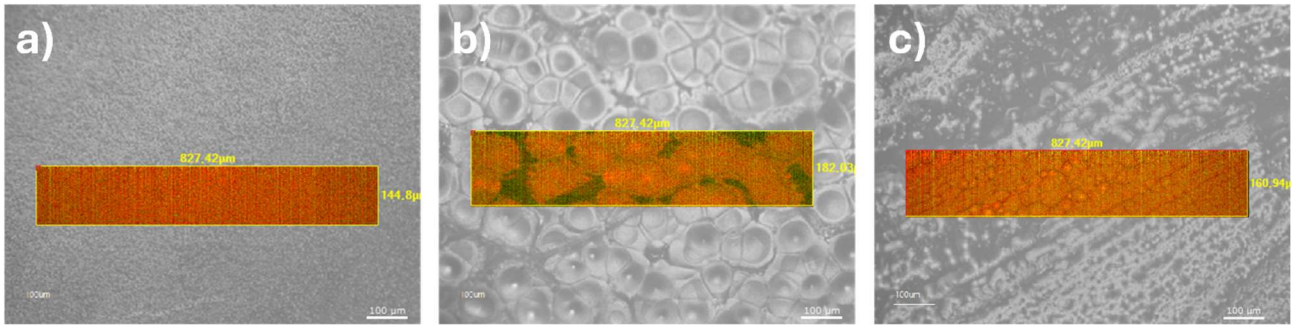

***Figure 25**: Raman imaging at 10x magnification of a) PLLA-1%, b) PLLA-5% and c) PLLA-10%. Red color was used for PLLA, while green color for hydroxyapatite*

Fig. 26 shows a high magnification chemical map of the different surfaces (50x).

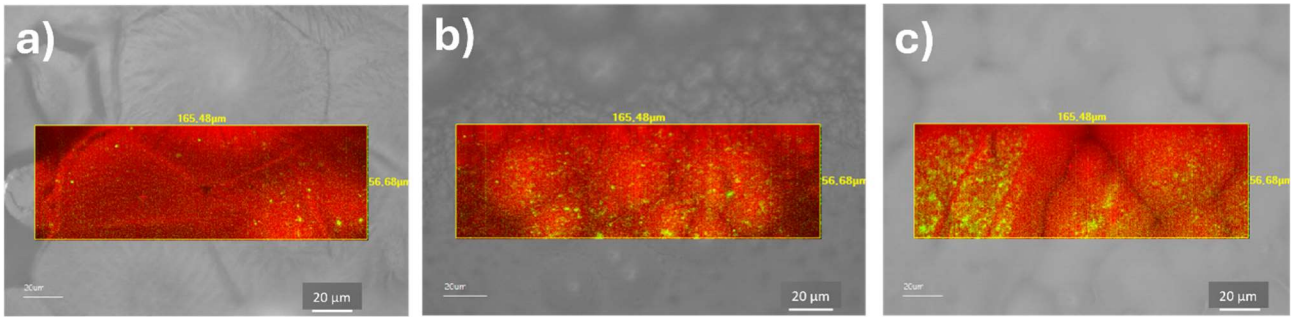

***Figure 26**: Raman imaging at 50x magnification of a) PLLA-1%, b) PLLA-5% and c) PLLA-10%. Red color was used for PLLA, while green color for hydroxyapatite*

The images clearly show that the hydroxyapatite has properly dispersed in the composite as small particles. This initial result shows and confirms the good quality of the sample preparation, in terms of nanopowder dispersion inside the sample. Although extremely promising, particle size and dispersion can surely be further improved with additional research on the preparation method.

After confirming hydroxyapatite incorporation and distribution, MEW was used to print the raw materials into a square grid, as detailed before. After printing, each scaffold was analyzed by Raman to ensure that the hydroxyapatite nanopowder kept a homogeneous distribution, as the melting process may cause aggregation or de-homogenization of the composite. As before, **Fig. 27** shows Raman imaging spectra for all three concentrations.

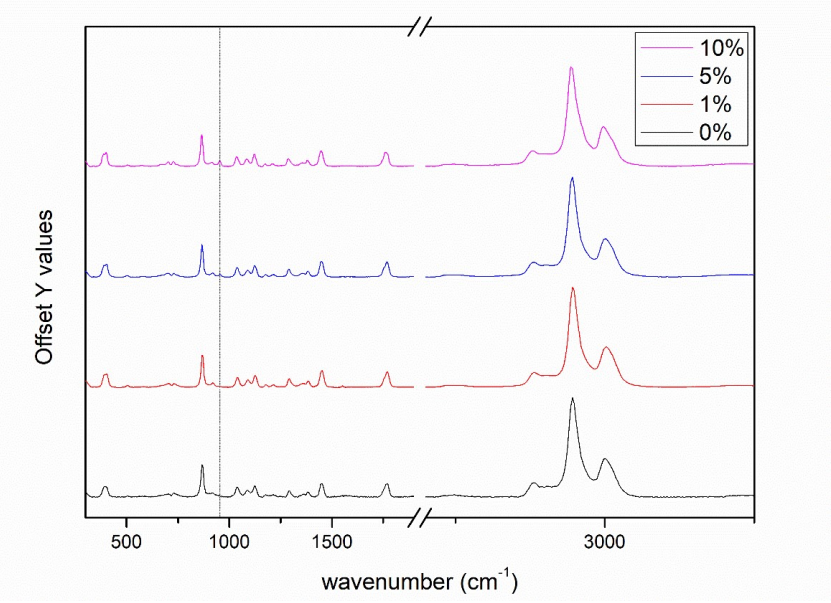

***Figure 27**: Average Raman spectra of the different scaffolds, as function of concentration of hydroxyapatite (from bottom to top). The vertical dotted line highlights the Raman band at 960 cm^{-1}*

Hydroxyapatite peaks are preserved after printing, with an increasing behavior akin to the samples mapping; proportionality of the concentration at 960 cm^{-1} is show in **Fig. 28**:

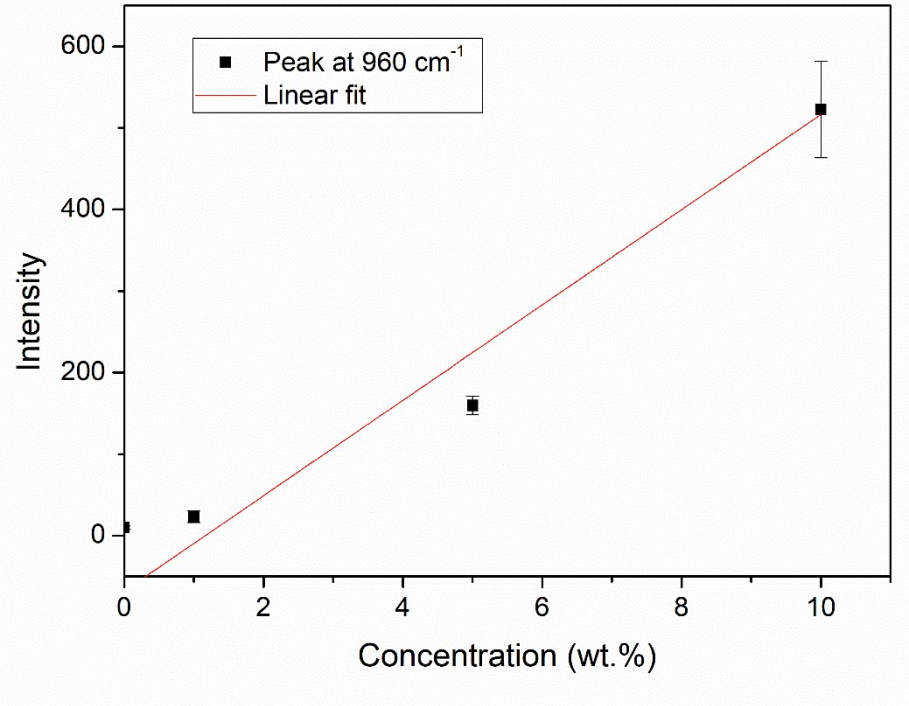

***Figure 28**: Intensity of the Raman band at 960 cm^{-1} on the scaffolds as function of hydroxyapatite concentration.*

Fig. 29 shows imaging results of the scaffolds at 100x magnification:

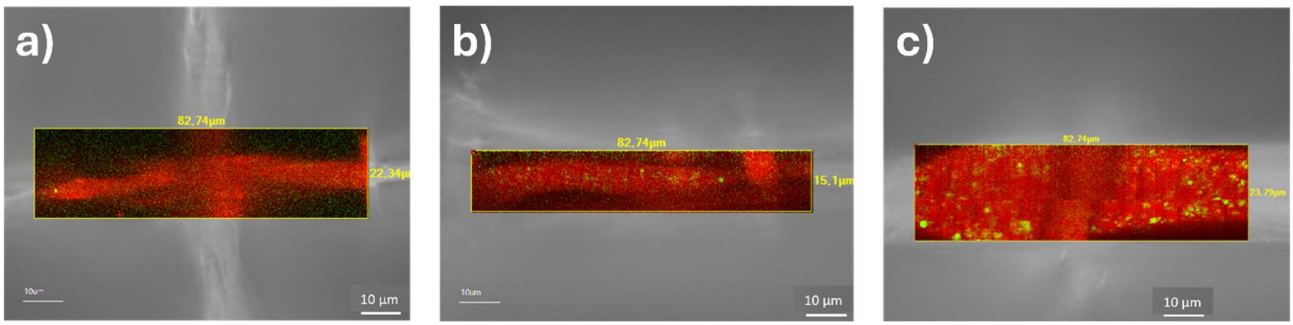

***Figure 29**: Raman imaging of the different scaffolds at 100x magnification. a) MEW-1%, b) MEW-5%, c) MEW-10%. Red color was used for PLLA, while green color for hydroxyapatite*

Despite maintaining an overall good distribution, the hydroxyapatite particles seem to have formed larger aggregates, as clearly observable from a comparison between **Fig. 29** and **Fig. 26**. Overall, scaffold imaging still shows promising results after printing, as hydroxyapatite dispersion is quite homogeneous.

EDS

EDS analyses performed on the different scaffolds showed an anomalous and uniform distribution of phosphorus on all three composite scaffolds (**Fig. 30**). Sometimes, instrumental artifacts or background signals can be misinterpreted as actual elemental signals. Calibration issues or contamination within the EDS system can contribute to such artifacts.

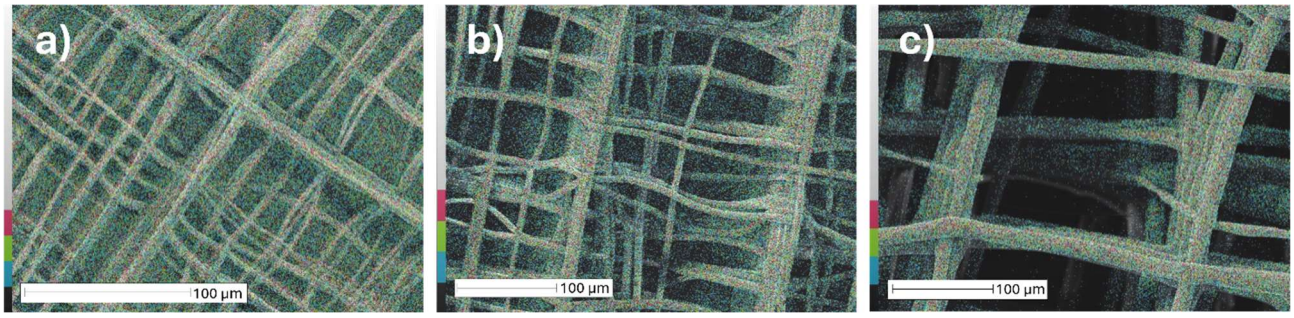

***Figure 30**: Distribution of phosphorus on the three scaffolds: a) MEW-1%, b) MEW-5%, c) MEW-10%*

To make sure the results were correct, an EDS analysis of the background was performed:

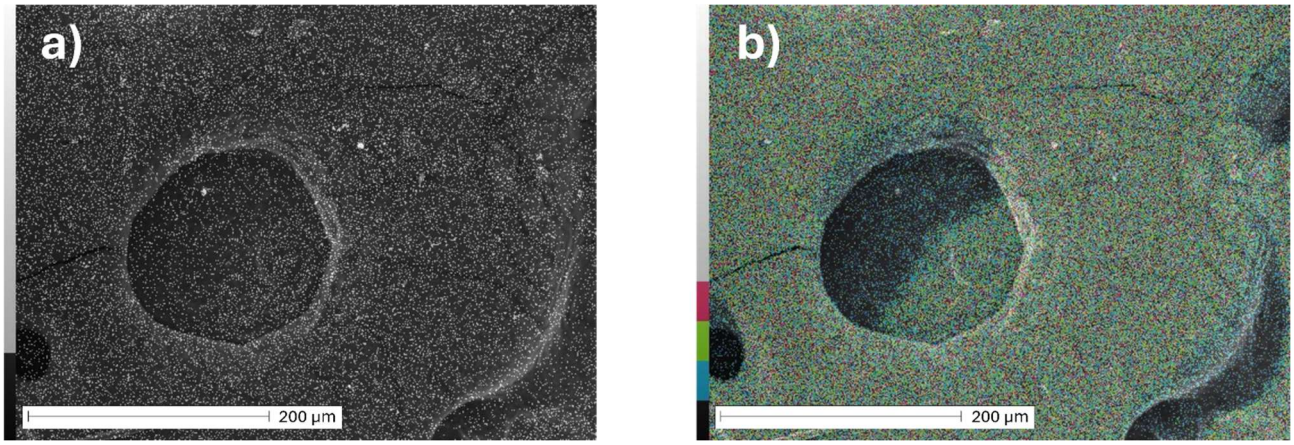

***Figure 31**: Background material EDS images showing distribution a) calcium and b) phosphorus*

Fig. 31 shows high concentration of phosphorus in the reference material, meaning that the anomalous signal in the scaffolds was caused by an instrumental artifact. On the other hand, despite the high noise, calcium signals were not present in such high quantities, and so the relative images could then be used to correctly visualize the distribution of hydroxyapatite in the scaffolds (**Fig. 32**).

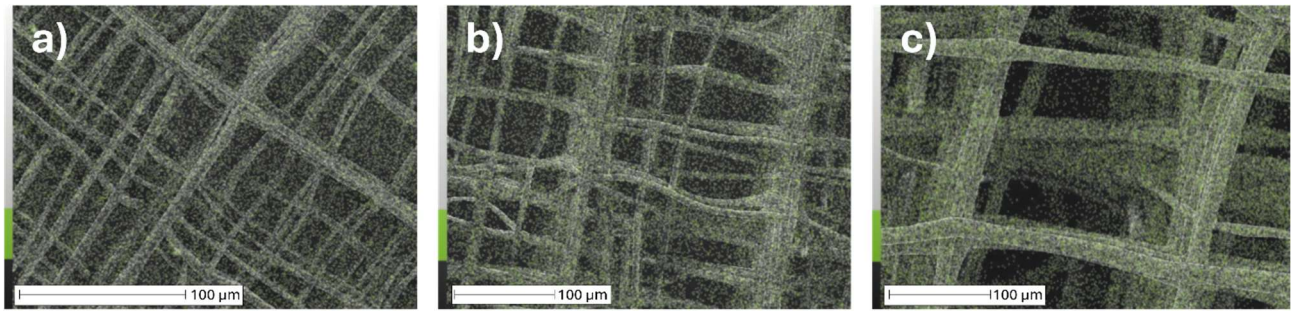

Figure 32: Distribution of calcium on the composite scaffolds, as measured by EDS: a) MEW-1%, b) MEW-5% and c) MEW-10%

As was partially shown by the Raman imaging, hydroxyapatite has been properly dispersed in PLLA and the increase in intensity and amount of calcium dots in the EDS images confirm the proportional increase in concentration. To confirm the elemental distribution, EDS was also performed with MEW-0%. Calcium and phosphorus readings are shown in **Fig. 33**.

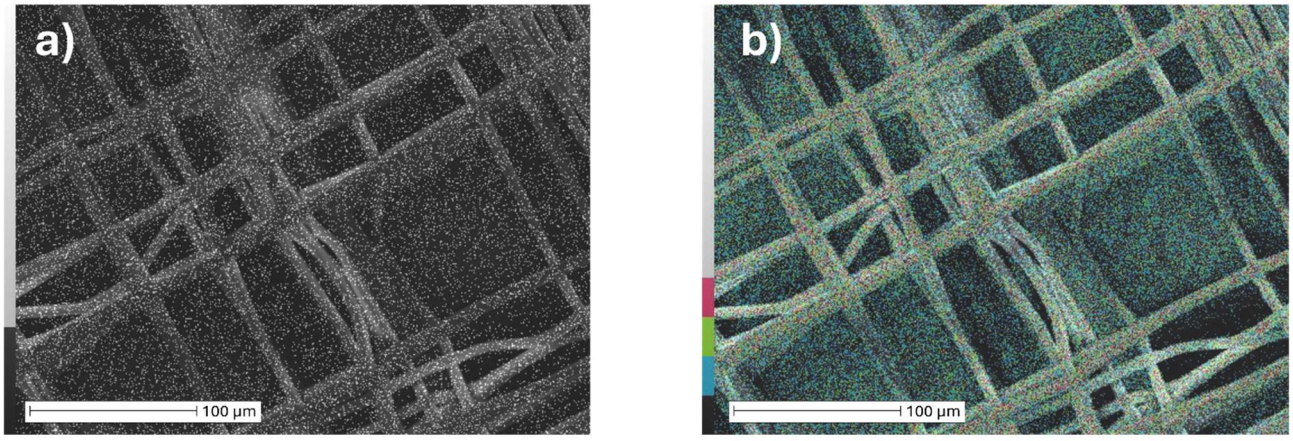

Figure 33: Distribution of a) calcium and b) phosphorus on the pure PLLA scaffold

As expected, the calcium element is not present in the pure polymer, while phosphorus artifacts are analogous to the previous ones. **Fig. 34** shows the concentration of calcium inside the different samples as a function of the theoretical amount of hydroxyapatite. It can be observed that a linear fitting interpolates all points, when considering the error bands.

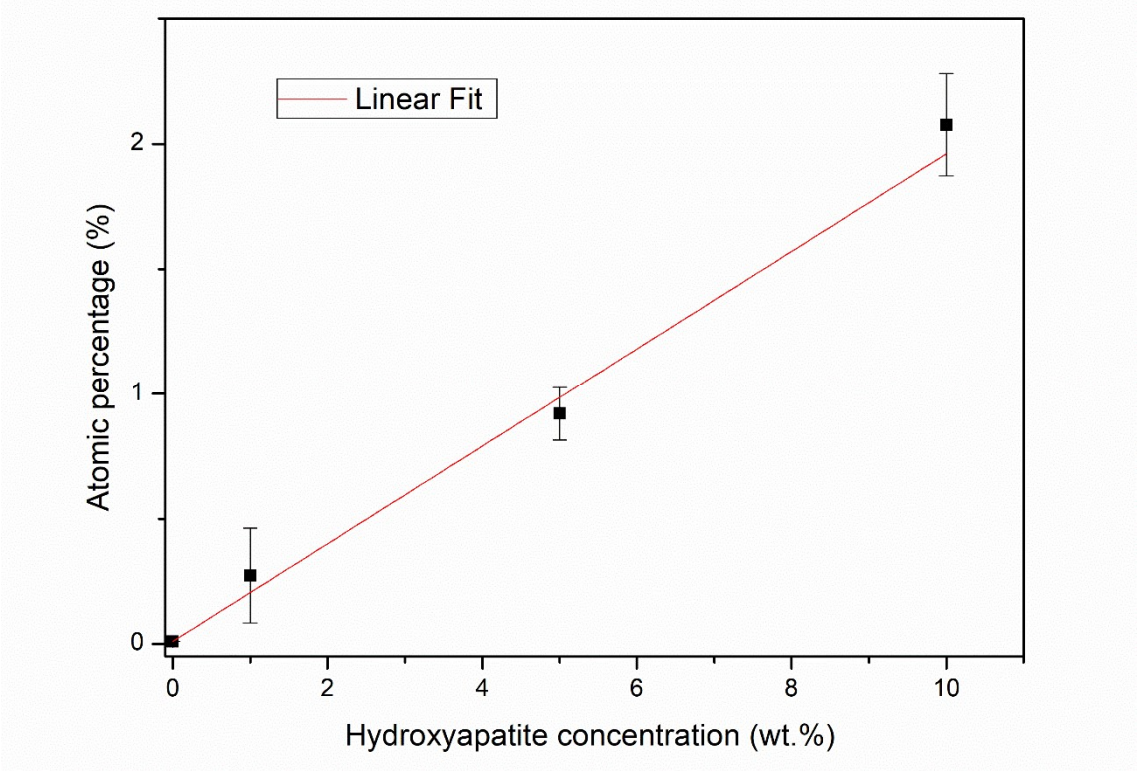

***Figure 34**: Linear fit of EDS calcium element results of the different scaffolds: data shows great proportionality of the element peaks as function of the calcium component*

XRD

XRD analysis has been used to evaluate the degree of crystallinity in each raw material and scaffold, in relation with the hydroxyapatite content. **Fig. 35** shows the X-ray diffraction patterns of the raw materials: the peaks are index of the presence of crystalline phase, while the large bell curve shows the presence of the amorphous phase. Patterns for the printed scaffolds are shown in **Fig. 36**. From both figures, a decrease in intensity of the crystallinity peak can be seen, with the increase in hydroxyapatite content. This relation indicates that the nanopowder hiders the PLLA fibers, reducing the crystallization phenomena.

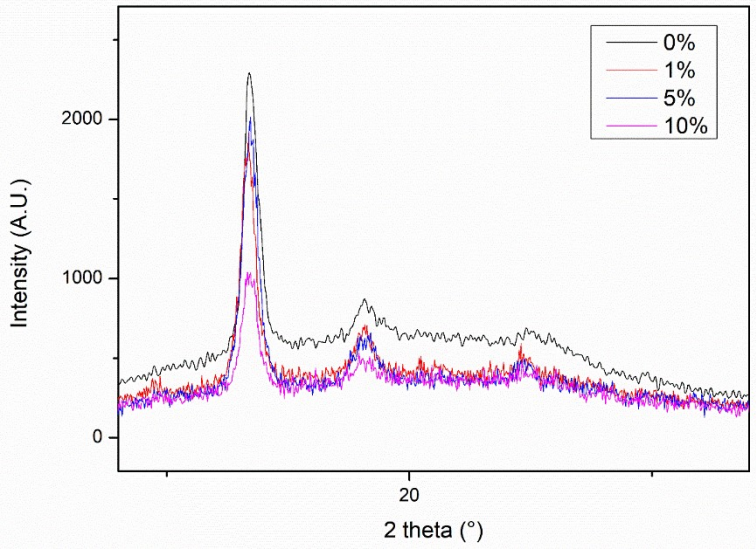

***Figure 35**: X-ray diffraction patterns for the raw materials, as a function of hydroxyapatite concentration*

An important factor that has been calculated with this analysis is the degree of crystallinity X_c: the curve was elaborated via fitting, where the area of the peaks and the amorphous phase have been calculated. As shown by the two graphs, PLLA has three different crystallinity peaks, thus the formula results as follows:

$$X_c = \frac{A_{c1} + A_{c2} + A_{c3}}{A_{c1} + A_{c2} + A_{c3} + A_a}$$

Where A_{c1}, A_{c2} and A_{c3} are the areas of the three crystalline peaks associated with PLLA, while A_a is the area of the broad background peak of the amorphous phase.

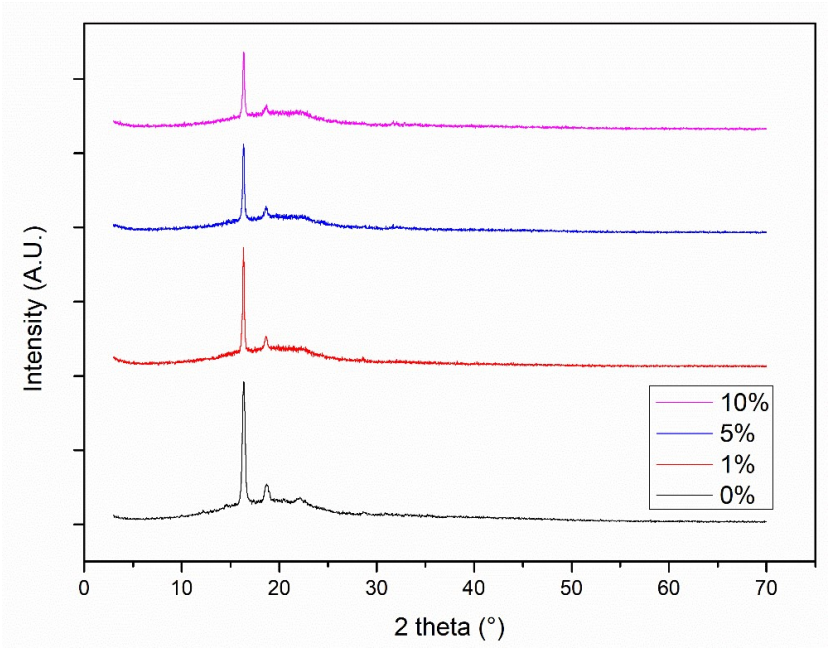

***Figure 36**: X-ray diffraction patterns for the composite samples, as a function of hydroxyapatite concentration*

Fig. 37 shows the behavior of the crystallinity index X_c by varying the amount of hydroxyapatite. Indeed, a trend can be identified: with the introduction of hydroxyapatite, the crystallinity of the sample rapidly decreases, resulting in a more amorphous sample overall. While initially rapid at first, the further increase in nanopowder gradually reduces crystallinity at a slower pace.

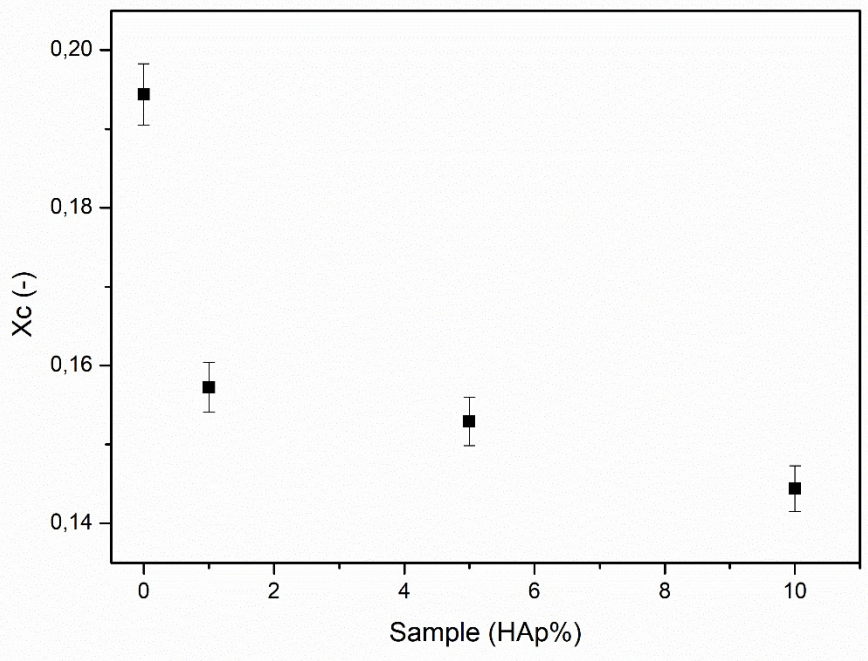

Figure 37: Relationship between the crystallinity index (X_c) and the concentration of hydroxyapatite in the scaffolds

6.3. Destructive chemical characterization

DSC

Differential Scanning Calorimetry was performed to evaluate the melting temperature of the raw materials as function of the hydroxyapatite content. **Tab. 7** shows the summary of the results thus obtained.

***Table 7**: DSC results relative to the melting temperature of the raw materials*

Sample	Melting temperature (°C)	Standard Deviation
PLLA	174.81	0.87
PLLA-1%	175.66	1.28
PLLA-5%	176.04	0.38
PLLA-10%	175.22	0.31

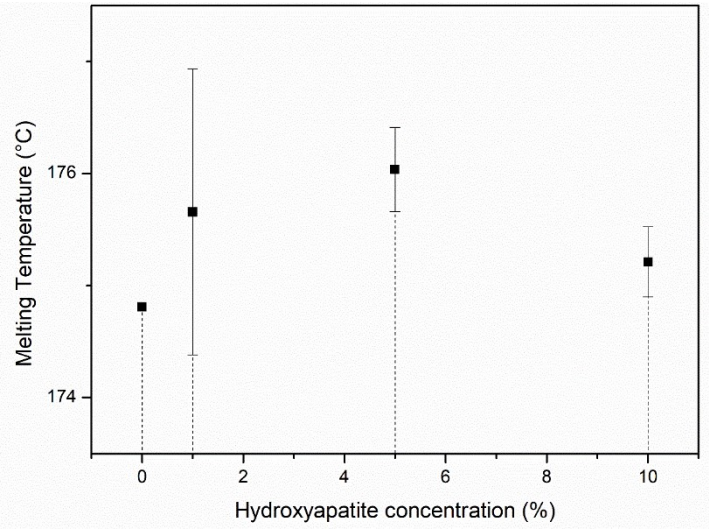

***Figure 38**: Melting temperature of the raw materials, as function of hydroxyapatite concentration*

It can be seen that the temperature at which the different raw materials melt does not differ much from each other and is not influenced by the presence of hydroxyapatite. This result suggests that there is no actual chemical interaction between the two phases, and the chemical structure of PLLA is not macroscopically altered by the presence of the reinforcing particles.

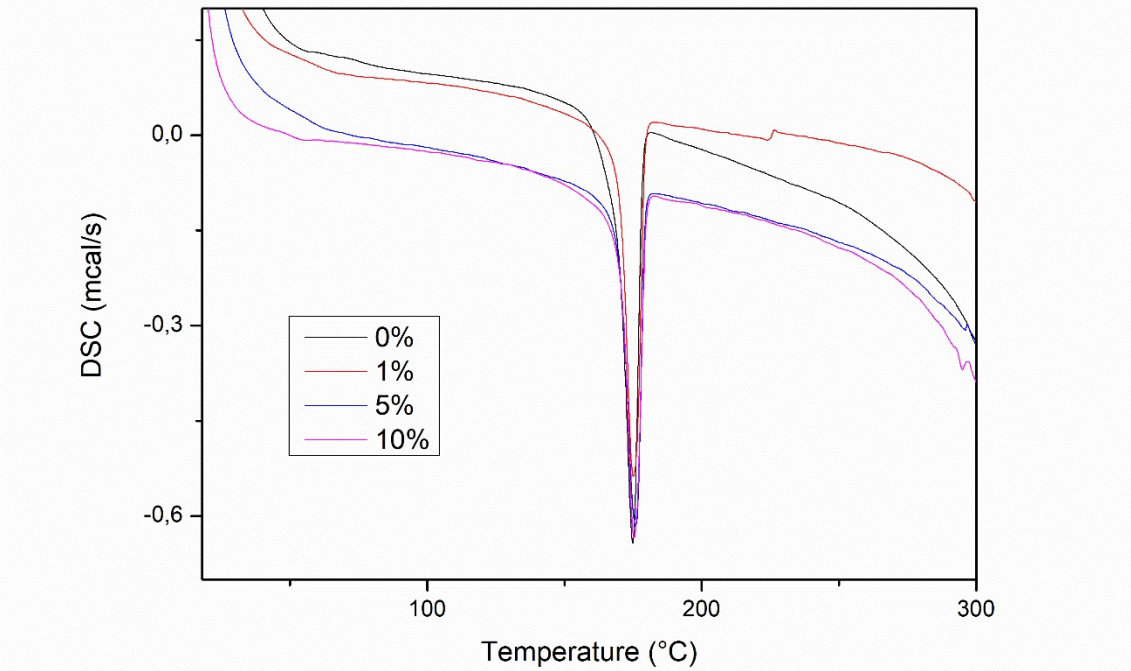

***Figure 39**: DSC curves of the different samples, as a function of hydroxyapatite content*

The width of the peak in **Fig. 39** is also not influenced by the presence of hydroxyapatite, suggesting that there is no noticeable change in the average molecular weight of the polymer. Similar crystallinity would also be suggested, but due to the XRD results we can conclude that the PLLA fibers are simply hindered by the hydroxyapatite, while maintaining the same average length.

TGA

Thermogravimetric analysis was performed on all the scaffolds to evaluate the degradation phenomenon by varying the content of hydroxyapatite. Furthermore, this was used to have a direct measure of the residual amount of material at the end of the test. Due to the final temperature of 600°C, it is safe to assume that what remains after the test is only the hydroxyapatite fraction. **Fig. 40** shows the TGA curves of the different scaffolds.

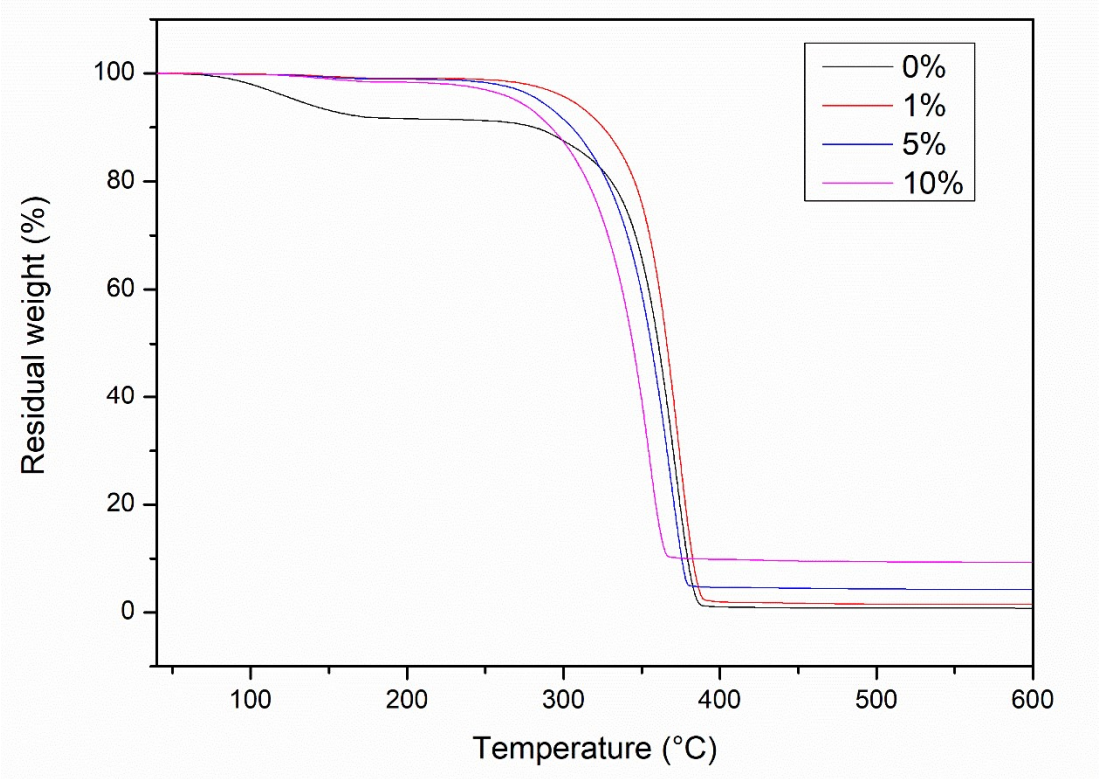

***Figure 40**: TGA curves for the different scaffolds, as a function of hydroxyapatite content*

As can be seen, each curve ends with a visibly different residual weight, and the higher the amount of hydroxyapatite in the sample, the higher this value. To further confirm the above-mentioned hypothesis, a proportionality graph was made with the same procedure done for Raman spectroscopy. **Fig. 41** shows great proportionality of the results obtained: with possible instrumental errors in mind, results confirm the absence of great high-melting impurities inside the samples; this also signifies a good quality in the production process of the scaffolds, that show the expected amounts of hydroxyapatite even after casting, drying, and melting

again during MEW. With the latter being the most critical point for maintaining homogenization after printing, data shows promising results and highlights the ability to preserve the nanopowder dispersed inside the scaffolds, with the intended concentration.

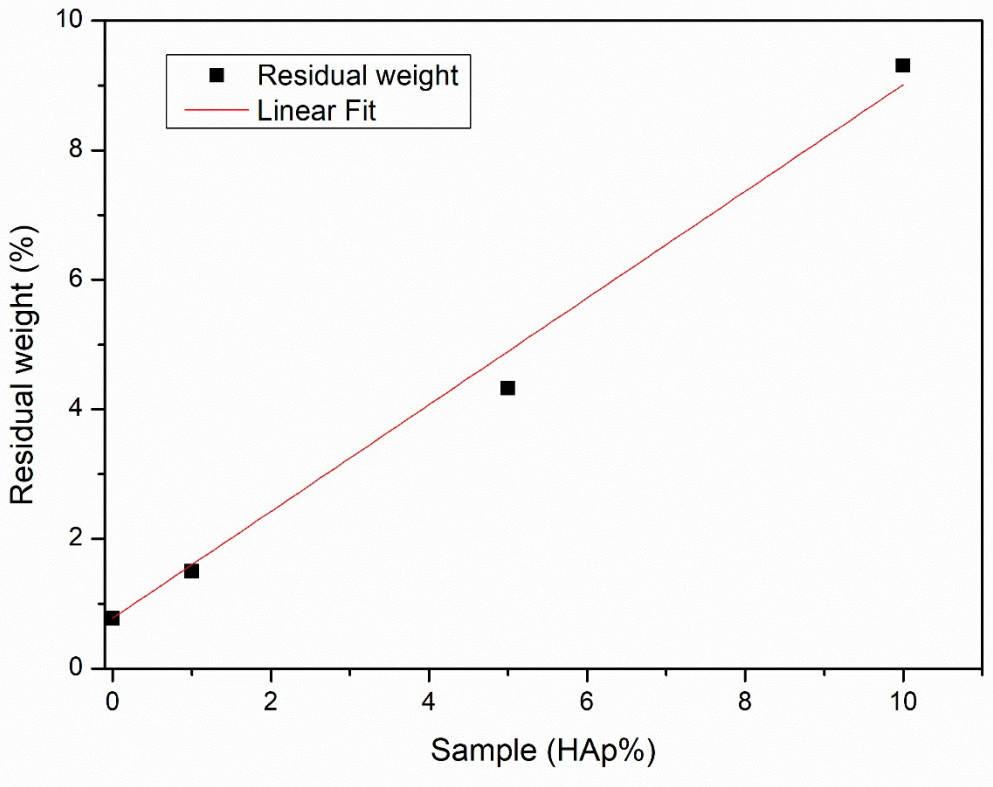

***Figure 41**: Linear fitting of the amount of residuals (weight %) and the amount of hydroxyapatite in the composite scaffolds after TGA. The graph starting from about 0.8% indicates either a contamination or an instrumental error*

6.4. Mechanical tests

Fig. 42 shows tensile testing results for MEW-0%, MEW-1%, MEW-5% and MEW-10%, printed in the shape of a 4x0.6 mm rectangular scaffold (10 layers in height). In general, all hydroxyapatite-containing scaffolds show a brittle behavior, typical of ceramic materials, completely opposite of pure PLLA that clearly behaves as a polymeric material through its characteristic long plastic deformation after the yield point. The toughness diagram also confirms that property, where MEW-0% is much tougher than MEW-1%, MEW-5% and MEW-10%, as they are brittle. Although much more fragile than the pure polymer, an interesting characteristic can be seen, concerning MEW-5%: in fact, despite the errors in the

measurements, higher maximum strength is shown, when compared to MEW-0%. Elastic module also shows great results in these terms, where if MEW-1% is weaker than MEW-0%, MEW-5% outclasses pure PLLA by having more than double the elastic module. While brittleness is unavoidable with this sample due to the presence of hydroxyapatite, having such a higher modulus means the scaffold can sustain more force, while reducing deformation and maintaining its shape during work.

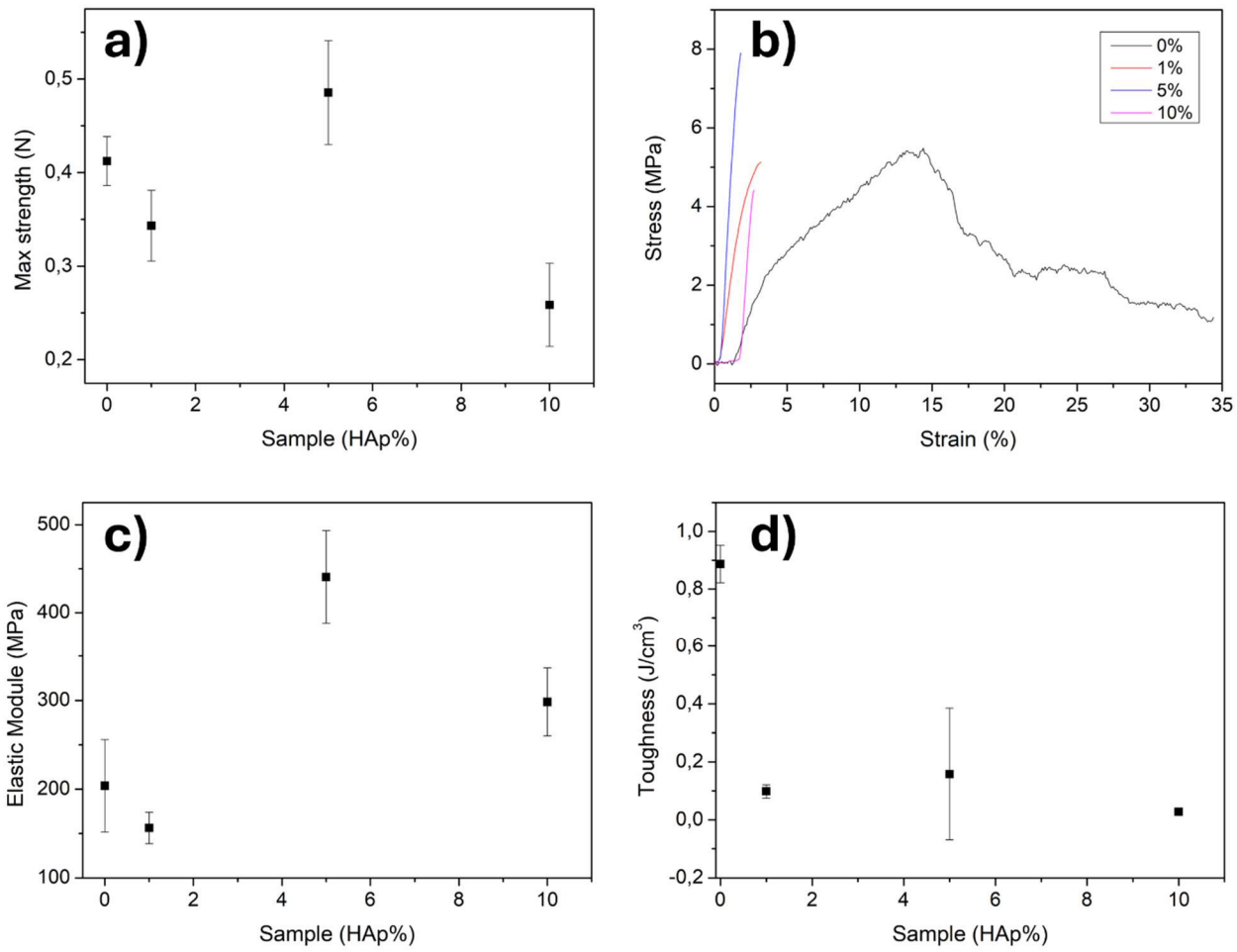

***Figure 42**: Tensile test results of the composite scaffolds: a) ultimate strength, b) Stress-strain curves, c) elastic modulus and d) toughness*

6.5. Biological tests

Cytotoxicity

WST-8 test was performed on Human Dermal Fibroblasts (HDF) in presence of the melt-electro written scaffolds to assess their possible cytotoxicity. Both pure PLLA and the composite scaffolds (MEW-1%, MEW-5%, MEW-10%) were analyzed with this test, and two incubation times of 24 h and 72 h were performed.

***Table 8**: Cytotoxicity WST-8 test results after 24 h and 72 h of incubation of the different scaffolds*

	% Living cells	Error %	% Living cells	Error %
	24h		**72h**	
Control	100.00%	3.45%	100.00%	3.81%
MEW-0%	78.84%	6.84%	81.16%	21.11%
MEW-1%	76.56%	15.49%	86.09%	15.79%
MEW-5%	81.86%	14.18%	78.86%	11.07%
MEW-10%	78.37%	10.92%	83.67%	11.65%

Tab. 8 shows the results for the two incubations after WTS-8 test, which are graphically summarized in **Fig. 43**: as can be seen, the level of living cells in MEW-1%, MEW-5% and MEW-10% is comparable to the one of MEW-0%, with around 80% of the cell colony remaining alive in the final solution environment, and this is true for both 24 h and 72 h cases. This value doesn't consider the number of cells that might be attached to the scaffold surface, which could result in an even higher number of living cells, as well as having good initial results concerning bioactivity. Although a very interesting information, this measurement has been found to be unfeasible to obtain due to the great difficulty in distinguishing the cells on the scaffold, also due to their transparency at the microscope.

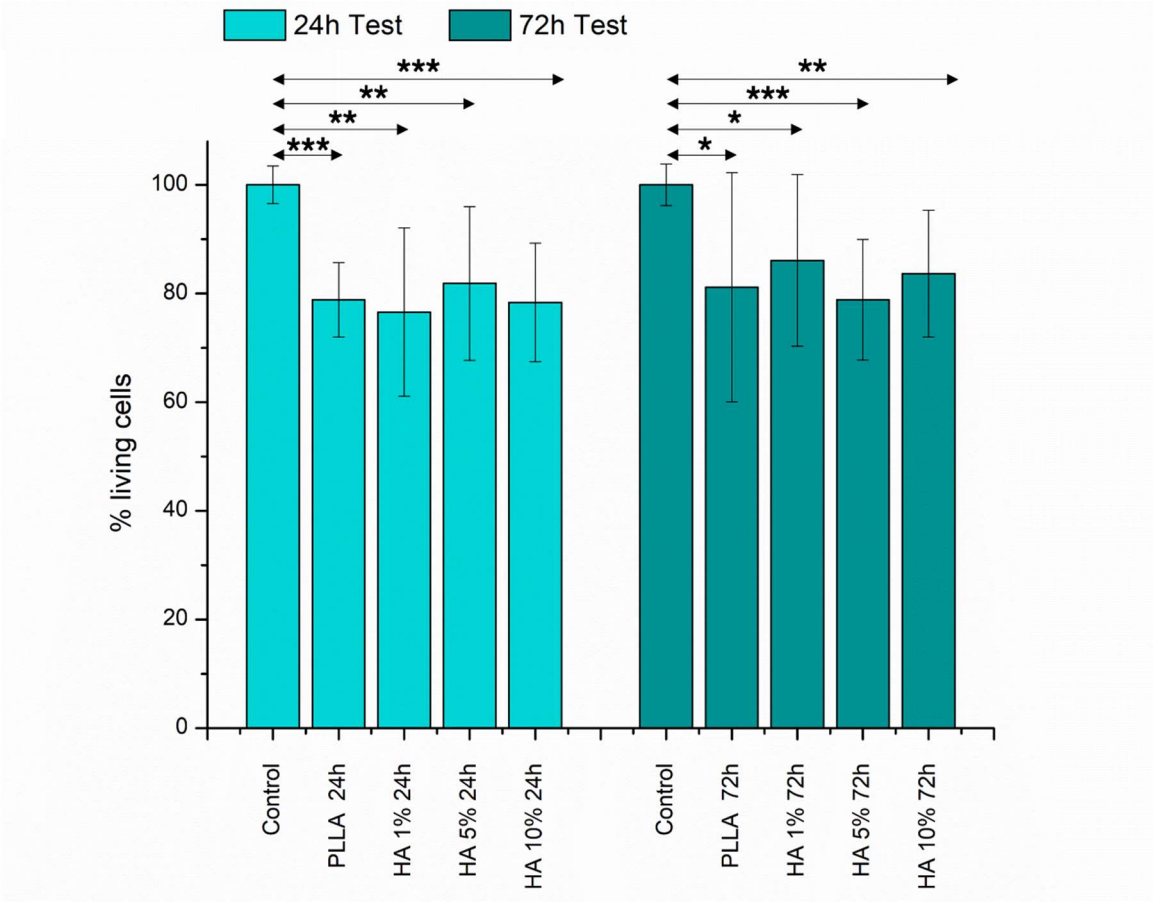

***Figure 43**: Cytotoxicity results of WTS-8 test after 24h (cyan, left) and 72h (dark green, right). From left to right: control system, MEW-0%, MEW-1%, MEW-5%, MEW-10%.* $* = p \leq 0.05,\ ** = p \leq 0.01,\ *** = p \leq 0.0001.$

Fig. 44 and **Fig. 45** show bright field images of cells adhered to the substrate on the 24-well plate after incubation for 24 and 72 hours, respectively. Cell presence can be visually noticed after image elaboration: when compared to the control, the amount seems slightly reduced; finally, no significant accumulation near or far from the scaffolds can be seen.

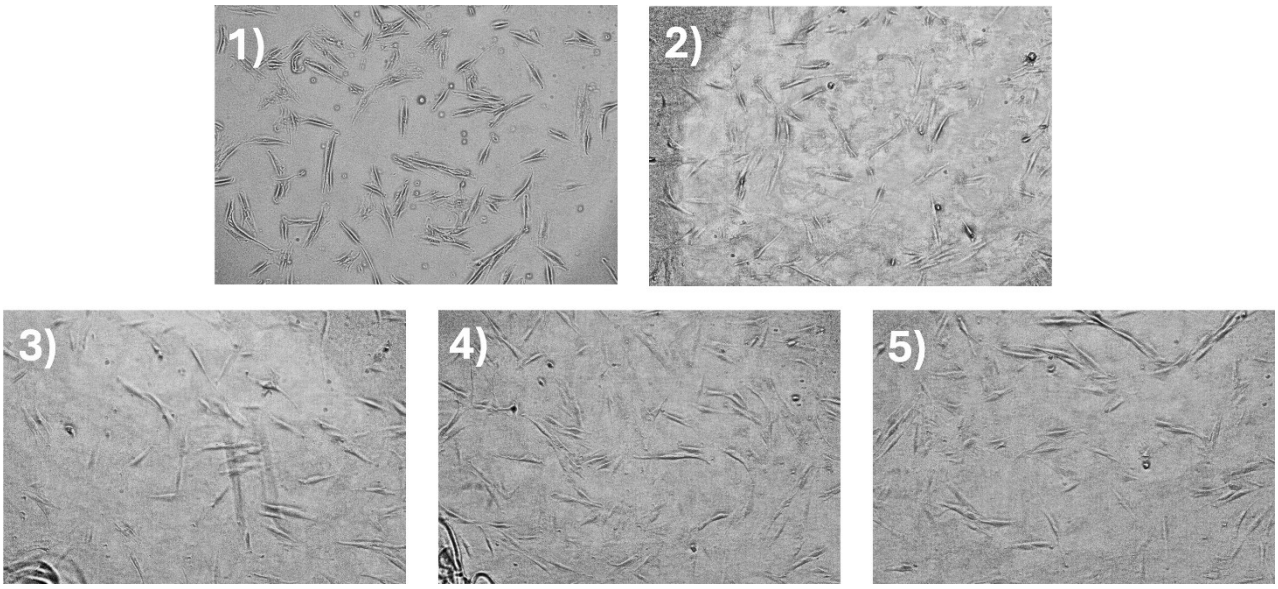

***Figure 44**: Bright field images of the different scaffolds after 24h of incubation: 1) Control, 2) MEW-0%, 3) MEW-1%, 4) MEW-5% and 5) MEW-10%*

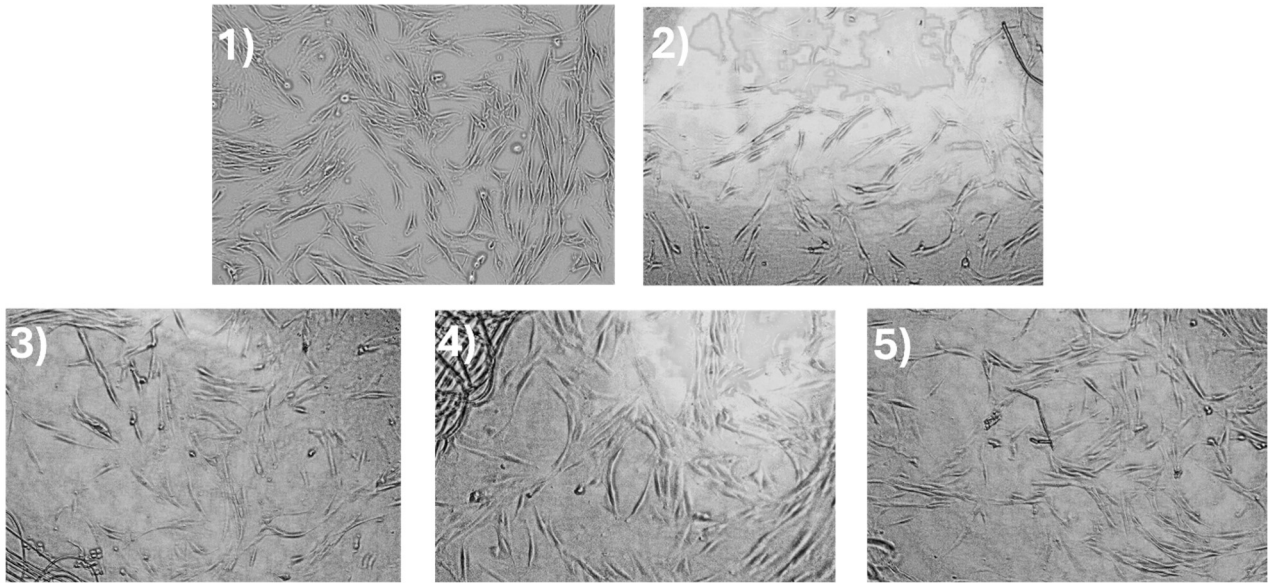

***Figure 45**: Bright field images of the different scaffolds after 72h of incubation: 1) Control, 2) MEW-0%, 3) MEW-1%, 4) MEW-5% and 5) MEW-10%*

An initial conclusion can be reached, as the scaffolds are not cytotoxic, due to most of the cells remaining alive. Furthermore, the remaining 20% of the cells might be dead or attached to the scaffold: this will have to be seen more in depth with a bioactivity test, where cell adhesion and proliferation is studied.

Acidity test

Evaluation of the pH of a 6 mg of raw material in 6mL of culture media solution has been performed to assess variation overtime of the solutions' pH. **Fig. 46** shows the results obtained up to 365 hours.

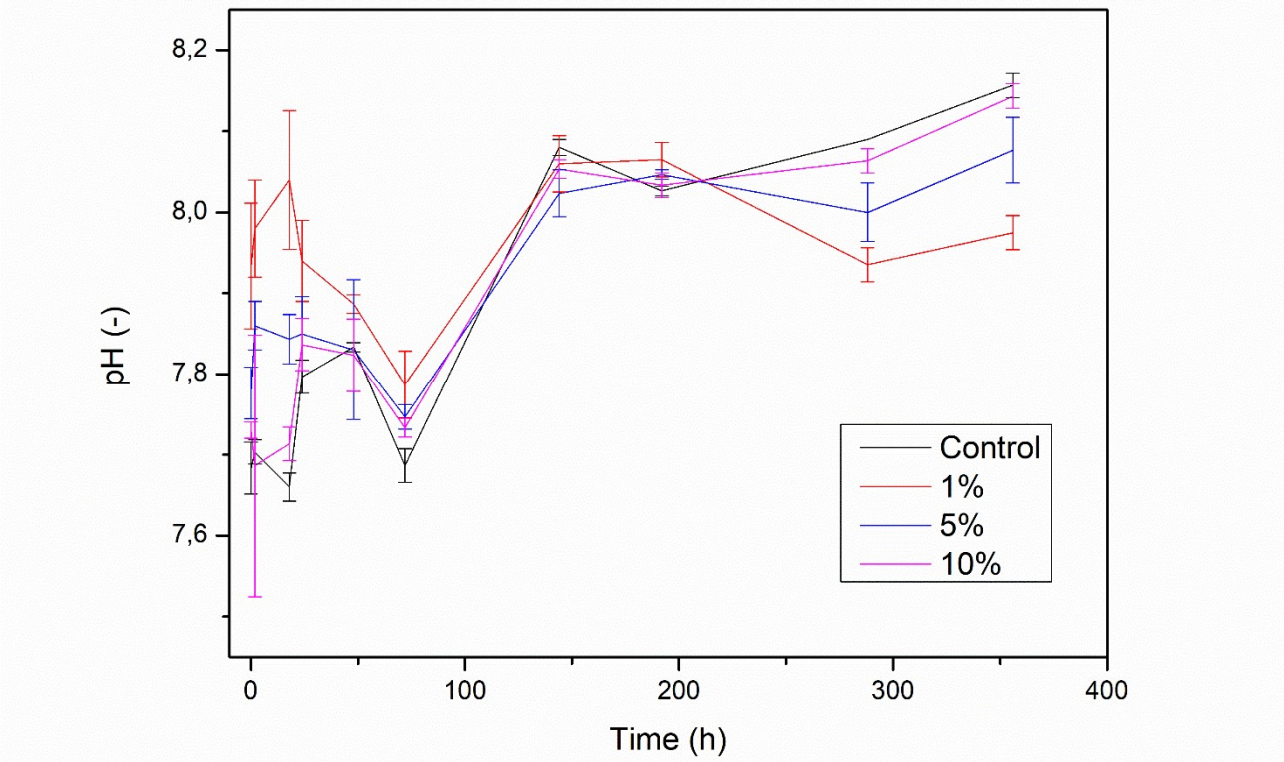

***Figure 46**: Acidity test results: lines show the pH trend over time of the samples*

Due to the nature of the culture media solution (control), its trend is to increase in pH over time. While all samples seem to have the same behavior, the speed at which they follow the control is different. In fact, samples with fewer amount of hydroxyapatite resulted in a slightly lower pH, while PLLA-10%, for example, had less difficulty in following the control solution. The results therefore show a possible degradation of PLLA, inducing a slightly more acid environment; the increase in hydroxyapatite content, though, allows the acidification effect to be more regulated, with a possible release of basic ions, as mentioned in literature [45]. Although the presence of PLLA seems to have some effect on the acidity of the nearby environment, due to the very low effect over the long period of time it is safe to assume that the degradation of the polymer would not result in dangerous situations during the tissue regeneration and healing process.

7. Discussion

With the collected data in this thesis, a few conclusions can be derived.

Starting with the printing process, the retention of a regular structure among the prints and the layers turned out to be a critical factor: the presence of hydroxyapatite would go against the imposed electric field used for printing, and the countereffect did only get more intense the higher the number of layers and the nanopowder concentration.

Despite these difficulties in the printing step, dispersion of the hydroxyapatite nanopowder was maintained before and after printing, as shown by Raman spectroscopy and EDS. Due to the nature of the analysis, TGA allowed us to physically measure the amount of remaining sample after the test: while a somewhat challenging task, the melt electro-written scaffolds turned out to maintain the desired hydroxyapatite concentration, which shows great potential for the techniques used.

Hydrophobicity of the scaffolds has been confirmed increasing by adding hydroxyapatite: this may result in a more difficult proliferation and interaction of cells, which can be acknowledged with the bioactivity test. A possible option to improve hydrophilicity, instead, may be the surface modification of the printed scaffolds, which may result in a better attachment of cells and improved interaction with the environment [59, 60].

The quick reduction in crystallinity induced by the presence of the hydroxyapatite nanopowder, by hindering with the PLLA fibers, was compared with the change in thermal degradation, being that the composite resulted less crystalline and more amorphous. By fitting the data in **Fig. 47**, a linear correlation can be seen, where a reduction in crystallinity due to the presence of hydroxyapatite corresponds to a lower decomposition temperature: the crystalline structure in the composite should bring a higher stability of the material; by obstructing the formation of this structure, the amorphous phase takes over and the material becomes more thermally sensible.

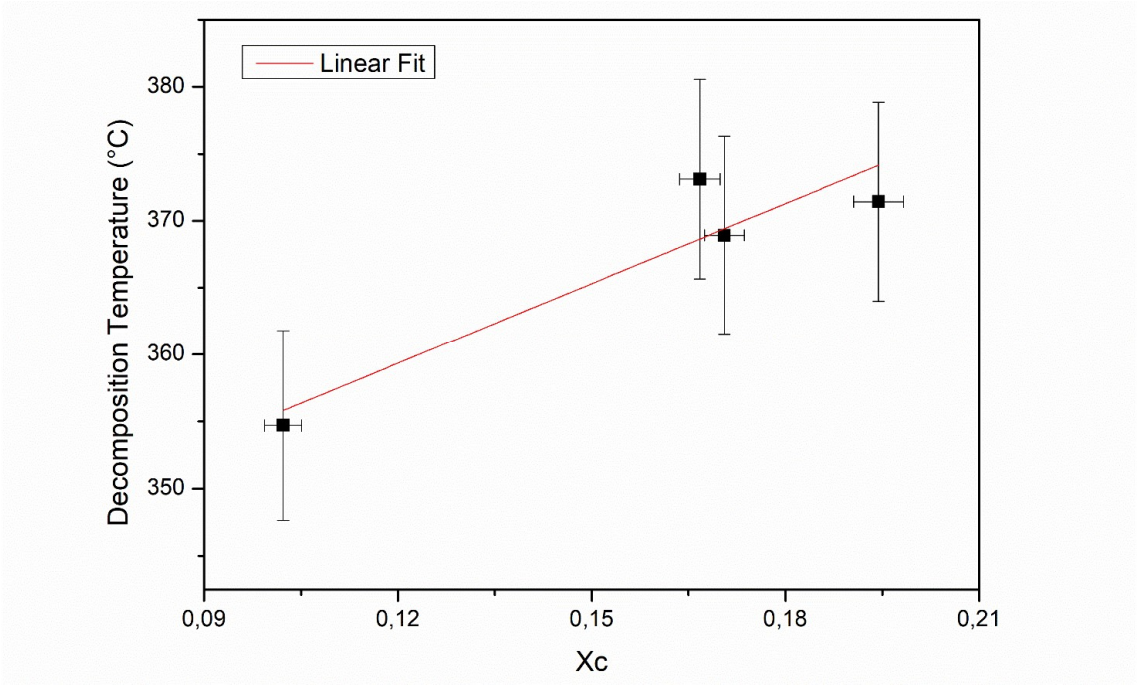

***Figure 47**: Correlation of crystallinity index and decomposition temperature of the scaffolds*

Further relations were made to confront crystallinity of the scaffolds with their elastic module, but no direct correlation was found.

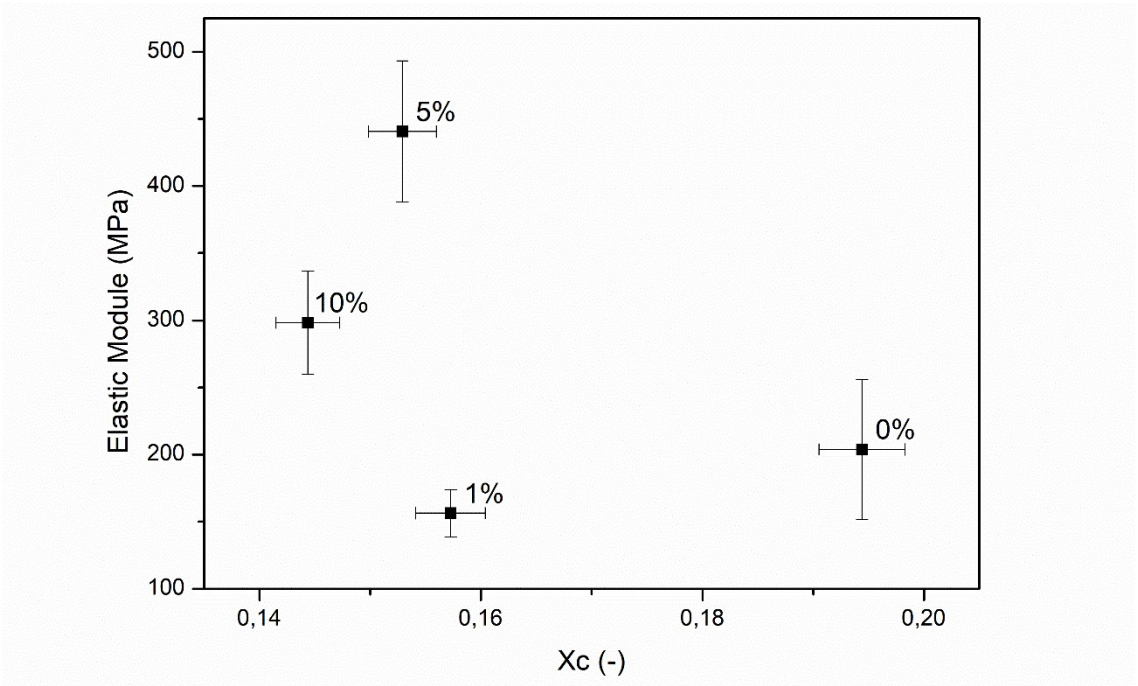

***Figure 48**: Correlation between crystallinity index and elastic modules of the scaffolds*

On the other hand, tensile test shows interesting results: with both elastic module and maximum strength value in mind, a particular behavior is shown: by adding a small amount of hydroxyapatite, the plasticity of the scaffold is lost and quickly replaced by a brittle characteristic. This is probably due to the presence of the nanopowder itself, that was shown to hinder PLLA fibers with the XRD test, thus the higher fragility of the material. With further addition of hydroxyapatite, though, a higher strength of the scaffold is reached, where maximum strength and especially elastic module values overclass the ones of PLLA, and bring higher tenacity to the composite material, able to withstand higher stresses: a great point when talking about its application in bone regeneration. An even higher amount of hydroxyapatite (MEW-10%), though, brings back down the scaffold properties: elastic module is maintained higher than the pure polymer, but the strength of the sample drastically decreases, as was directly noticed by the difficulty of moving the sample without damaging it during experimentation; toughness of the composites does not significantly change between each other, although in general is much lower than the polymer, also due to their brittle nature.

Overall, data shows that there shall be an optimum condition around 5% hydroxyapatite, where mechanical properties (maximum strength, elastic module) are the highest; further increase in nanopowder over 10% would probably over-obstruct the polymeric chains, making a more rigid and difficult composite overall, as long as the preparation and MEW are feasible.

Finally, cytotoxicity test resulted negative, and so the scaffolds are able to undergo the bioactivity test. As results of the latter are not available yet, some hypotheses can be made. Firstly, the composite shall be a good candidate for bone regeneration and cell proliferation: although the structure of the print was not of very high precision due to the presence of hydroxyapatite, cell diffusion shall not be completely hindered. Due to the nature of the ceramic material present in the scaffolds, it is likely that this would act as site for cells to attach to: from there, proliferation would continue, and more and more cells would be able to attach to the composite scaffold. Even though a higher amount of hydroxyapatite would be better due to the increase in attachment sites, mechanical factors (as well as sample preparation complications) have to be taken into account: the increase in cell adhesion is not the only variable that has to be kept in mind here, as structural stability needs to be maintained for a long period of time. This makes tensile testing results an important asset to utilize. The optimal

condition is a composite with enough hydroxyapatite to improve cell adhesion, amount mediated to obtain a scaffold with high mechanical resistance and strength: this would grant a stable and durable structure that can sustain stresses, where osteoblastic cells easily proliferate to promote bone tissue regeneration.

8. Conclusions

In this thesis work composites with different concentration of hydroxyapatite (from 0% to 10%) were produced. Scaffolds were then printed and characterized using a self-assembled electrohydrodynamics guided melt electro-writing 3D printer.

The morphological characterization performed with SEM and Optical Laser Microscope showed a relatively good quality print, even if the scaffolds resulted not completely regular due to the presence of hydroxyapatite, that destabilized the electric field.

The chemical characterization performed through FT-IR, EDS and Raman spectrometry showed a uniform distribution of hydroxyapatite across the PLLA fibers, with a total concentration in line with the expected results: with their presence both before and after the printing process, hydroxyapatite peaks confirmed homogenization and proportionality to the expected composite concentration. TGA analysis further confirmed the presence of hydroxyapatite and quantitatively showed the amount of remaining nanopowder after the thermogravimetric test, again proportional to the expected concentrations. In conjunction with that, DSC was also performed, but the resulting melting temperature showed no substantial derivation from the pure component, indicating a non-chemical interaction between the two materials.

Contact angle was also evaluated to determine the hydrophobicity of the sample, where an overall increase was shown as hydroxyapatite content increased: to improve hydrophilicity surface modification can be a possible solution.

With the addition of hydroxyapatite, changes in crystallinity were shown with XRD analysis, where the nanopowder was confirmed to obstacle the polymer fibers by reducing the ability to form crystalline structures, and therefore increasing the amorphous phase.

Brittle behavior was shown with the tensile testing: despite showing complete brittleness for all the three composite samples, MEW-5% had good results in terms of max strength and elastic module values, where the latter resulted much higher than the pure PLLA, expressing promising results in terms of its mechanical resistance during the treatment in the patient.

Finally, cytotoxicity for both the pure component and the hydroxyapatite-containing composites was tested through WST-8 test on Human Dermal Fibroblast (HDF). The samples were incubated for 24h and 72h before being tested. All the results showed that around 80% of the cells was still alive after the test, thus confirming the non-cytotoxicity of the samples. Moreover, the remaining 20% of cells might not have been completely dead, as some of the cells could have attached to the scaffolds. Although a challenging task in this phase, this hypothesis brings good expectations for the bioactivity test.

Acidity test was then performed to evaluate the degradation of the composites and the possible acidification of the environment. Results showed a similar behavior to what was expected from bibliography, where no dangerous behavior was observed over time.

Overall, the raw material production process, as well as the results after MEW printing, confirmed the feasibility of the method to homogeneously disperse the nanopowder in the polymer matrix. The addition of hydroxyapatite helped maintain good affinity to the environment the scaffold would be exposed to. Although, when compared to the pure PLLA scaffold, reduction in crystallinity and brittleness transition can be shown, more interesting characteristics are highlighted, such as higher strength and lower deformation.

All in all, the PLLA-hydroxyapatite composite has shown great results in terms of sample production, printing, and characterization outcomes. Although more studies would certainly benefit further knowledge on this type of material, the data obtained in this thesis research highlights some potential characteristics and properties of this composite material, showing promising signs to applications for bone regeneration in the biomedical field.

9. Acknowledgements

The author of this work is grateful to the Kyoto Institute of Technology, Ceramics Department Laboratory for allowing the development of this research. Thanks to the Erasmus+/Non-EU Partner Countries 2023/2024 International Program, sponsored by Polytechnic of Turin, for thesis research project position at the Kyoto Institute of Technology, Japan.

10. References

1. Feng, X.: Chemical and Biochemical Basis of Cell-Bone Matrix Interaction in Health and Disease. Curr Chem Biol. 3, 189–196 (2009). https://doi.org/10.2174/187231309788166398
2. Morgan, E.F., Unnikrisnan, G.U., Hussein, A.I.: Bone Mechanical Properties in Healthy and Diseased States, (2018)
3. Fan, J., Abedi-Dorcheh, K., Vaziri, A.S., Kazemi-Aghdam, F., Rafieyan, S., Sohrabinejad, M., Ghorbani, M., Adib, F.R., Ghasemi, Z., Klavins, K., Jahed, V.: A Review of Recent Advances in Natural Polymer-Based Scaffolds for Musculoskeletal Tissue Engineering, (2022)
4. Abbasi, N., Hamlet, S., Love, R.M., Nguyen, N.T.: Porous scaffolds for bone regeneration, (2020)
5. Abjornson, C., Yoon, B.V., Lane, J.M.: Chapter 2 | Bone Graft Substitutes: Classifications and Orthopedic Applications.
6. Meng, J., Boschetto, F., Yagi, S., Marin, E., Adachi, T., Chen, X., Pezzotti, G., Sakurai, S., Yamane, H., Xu, H.: Melt-Electrowritten Poly(L-lactic acid)- and Bioglass-Reinforced biomimetic hydrogel for bone regeneration. Mater Des. 219, (2022). https://doi.org/10.1016/j.matdes.2022.110781
7. Zhang, H., Mao, X., Du, Z., Jiang, W., Han, X., Zhao, D., Han, D., Li, Q.: Three dimensional printed macroporous polylactic acid/hydroxyapatite composite scaffolds for promoting bone formation in a critical-size rat calvarial defect model. Sci Technol Adv Mater. 17, 136–148 (2016). https://doi.org/10.1080/14686996.2016.1145532
8. Roseti, L., Parisi, V., Petretta, M., Cavallo, C., Desando, G., Bartolotti, I., Grigolo, B.: Scaffolds for Bone Tissue Engineering: State of the art and new perspectives, (2017)
9. Murphy, S. V., Atala, A.: 3D bioprinting of tissues and organs, (2014)
10. Bose, S., Vahabzadeh, S., Bandyopadhyay, A.: Bone tissue engineering using 3D printing, (2013)
11. Zhang, M., Lin, R., Wang, X., Xue, J., Deng, C., Feng, C., Zhuang, H., Ma, J., Qin, C., Wan, L., Chang, J., Wu, C.: A P P L I E D S C I E N C E S A N D E N G I N E E R I N G 3D printing of Haversian bone-mimicking scaffolds for multicellular delivery in bone regeneration. (2020)

12. Kim, C.G., Han, K.S., Lee, S., Kim, M.C., Kim, S.Y., Nah, J.: Fabrication of biocompatible polycaprolactone–hydroxyapatite composite filaments for the FDM 3D printing of bone scaffolds. Applied Sciences (Switzerland). 11, (2021). https://doi.org/10.3390/app11146351
13. Lee, K.W., Wang, S., Fox, B.C., Ritman, E.L., Yaszemski, M.J., Lu, L.: Poly(propylene fumarate) bone tissue engineering scaffold fabrication using stereolithography: Effects of resin formulations and laser parameters. Biomacromolecules. 8, 1077–1084 (2007). https://doi.org/10.1021/bm060834v
14. Fathi, A., Kermani, F., Behnamghader, A., Banijamali, S., Mozafari, M., Baino, F., Kargozar, S.: Three-dimensionally printed polycaprolactone/multicomponent bioactive glass scaffolds for potential application in bone tissue engineering. Biomedical Glasses. 6, 57–69 (2021). https://doi.org/10.1515/bglass-2020-0006
15. Dubinenko, G., Zinoviev, A., Bolbasov, E., Kozelskaya, A., Shesterikov, E., Novikov, V., Tverdokhlebov, S.: Highly filled poly(l-lactic acid)/hydroxyapatite composite for 3D printing of personalized bone tissue engineering scaffolds. J Appl Polym Sci. 138, (2021). https://doi.org/10.1002/app.49662
16. Tulyaganov, D.U., Fiume, E., Akbarov, A., Ziyadullaeva, N., Murtazaev, S., Rahdar, A., Massera, J., Verné, E., Baino, F.: In Vivo Evaluation of 3D-Printed Silica-Based Bioactive Glass Scaffolds for Bone Regeneration. J Funct Biomater. 13, (2022). https://doi.org/10.3390/jfb13020074
17. Anvari Kohestani, A., Pishbin, F.: 3D Printing of Bone Scaffolds Based on Alginate/Gelatin Hydrogel Ink Containing Bioactive Glass 45S5 and ZIF-8 Nanoparticles with Sustained Drug-Release Capability. Adv Eng Mater. 25, (2023). https://doi.org/10.1002/adem.202300563
18. Montalbano, G., Borciani, G., Cerqueni, G., Licini, C., Banche-Niclot, F., Janner, D., Sola, S., Fiorilli, S., Mattioli-Belmonte, M., Ciapetti, G., Vitale-Brovarone, C.: Collagen hybrid formulations for the 3d printing of nanostructured bone scaffolds: An optimized genipin-crosslinking strategy. Nanomaterials. 10, 1–23 (2020). https://doi.org/10.3390/nano10091681
19. Jeong, J.E., Park, S.Y., Shin, J.Y., Seok, J.M., Byun, J.H., Oh, S.H., Kim, W.D., Lee, J.H., Park, W.H., Park, S.A.: 3D Printing of Bone-Mimetic Scaffold Composed of Gelatin/β-

Tri-Calcium Phosphate for Bone Tissue Engineering. Macromol Biosci. 20, (2020). https://doi.org/10.1002/mabi.202000256

20. Bae, E. Bin, Park, K.H., Shim, J.H., Chung, H.Y., Choi, J.W., Lee, J.J., Kim, C.H., Jeon, H.J., Kang, S.S., Huh, J.B.: Efficacy of rhBMP-2 Loaded PCL/ β -TCP/bdECM Scaffold Fabricated by 3D Printing Technology on Bone Regeneration. Biomed Res Int. 2018, (2018). https://doi.org/10.1155/2018/2876135
21. Jin, G., Kim, G.H.: Rapid-prototyped PCL/fucoidan composite scaffolds for bone tissue regeneration: Design, fabrication, and physical/biological properties. J Mater Chem. 21, 17710–17718 (2011). https://doi.org/10.1039/c1jm12915e
22. Wang, Y., Shi, X., Ren, L., Yao, Y., Zhang, F., Wang, D.A.: Poly(lactide-co-glycolide)/titania composite microsphere-sintered scaffolds for bone tissue engineering applications. J Biomed Mater Res B Appl Biomater. 93, 84–92 (2010). https://doi.org/10.1002/jbm.b.31561
23. Balen, R., Da Costa, W.V., De Lara Andrade, J., Piai, J.F., Muniz, E.C., Companhoni, M.V., Nakamura, T.U., Lima, S.M., Da Cunha Andrade, L.H., Bittencourt, P.R.S., Hechenleitner, A.A.W., Pineda, E.A.G., Fernandes, D.M.: Structural, thermal, optical properties and cytotoxicity of PMMA/ZnO fibers and films: Potential application in tissue engineering. Appl Surf Sci. 385, 257–267 (2016). https://doi.org/10.1016/j.apsusc.2016.05.122
24. Wang, F., Liu, J., Liu, J., Zhang, S., Yang, M., Kang, K.: Comparison of the Effects of 3D Printing Bioactive Porous Titanium Alloy Scaffolds and Nano-biology for Direct Treatment of Bone Defects. Cell Mol Biol. 68, 86–95 (2022). https://doi.org/10.14715/cmb/2022.68.3.11
25. Guo, Y., Wu, J., Xie, K., Tan, J., Yang, Y., Zhao, S., Wang, L., Jiang, W., Hao, Y.: Study of Bone Regeneration and Osteointegration Effect of a Novel Selective Laser-Melted Titanium-Tantalum-Niobium-Zirconium Alloy Scaffold. ACS Biomater Sci Eng. 5, 6463–6473 (2019). https://doi.org/10.1021/acsbiomaterials.9b00909
26. Sari, M., Kristianto, N.A., Chotimah, Ana, I.D., Yusuf, Y.: Carbonated hydroxyapatite-based honeycomb scaffold coatings on a titanium alloy for bone implant application—physicochemical and mechanical properties analysis. Coatings. 11, (2021). https://doi.org/10.3390/coatings11080941

27. Farah, S., Anderson, D.G., Langer, R.: Physical and mechanical properties of PLA, and their functions in widespread applications — A comprehensive review, (2016)
28. Morão, A., de Bie, F.: Life Cycle Impact Assessment of Polylactic Acid (PLA) Produced from Sugarcane in Thailand. J Polym Environ. 27, 2523–2539 (2019). https://doi.org/10.1007/s10924-019-01525-9
29. Balla, E., Daniilidis, V., Karlioti, G., Kalamas, T., Stefanidou, M., Bikiaris, N.D., Vlachopoulos, A., Koumentakou, I., Bikiaris, D.N.: Poly(lactic acid): A versatile biobased polymer for the future with multifunctional properties-from monomer synthesis, polymerization techniques and molecular weight increase to PLA applications, (2021)
30. Velghe, I., Buffel, B., Vandeginste, V., Thielemans, W., Desplentere, F.: Review on the Degradation of Poly(lactic acid) during Melt Processing, (2023)
31. Carrasco, F., Pérez, O.S., Maspoch, M.L.: Kinetics of the thermal degradation of poly(Lactic acid) and polyamide bioblends. Polymers (Basel). 13, (2021). https://doi.org/10.3390/polym13223996
32. Oberbek, P., Bolek, T., Chlanda, A., Hirano, S., Kusnieruk, S., Rogowska-Tylman, J., Nechyporenko, G., Zinchenko, V., Swieszkowski, W., Puzyn, T.: Characterization and influence of hydroxyapatite nanopowders on living cells. Beilstein Journal of Nanotechnology. 9, 3079–3094 (2018). https://doi.org/10.3762/bjnano.9.286
33. Fiume, E., Magnaterra, G., Rahdar, A., Verné, E., Baino, F.: Hydroxyapatite for biomedical applications: A short overview, (2021)
34. Wu, X., Walsh, K., Hoff, B.L., Camci-Unal, G.: Mineralization of biomaterials for bone tissue engineering, (2020)
35. Budharaju, H., Suresh, S., Sekar, M.P., De Vega, B., Sethuraman, S., Sundaramurthi, D., Kalaskar, D.M.: Ceramic materials for 3D printing of biomimetic bone scaffolds – Current state-of-the-art & future perspectives, (2023)
36. Solubility of Hydroxyapatite.
37. Chen, Z.F., Darvell, B.W., Leung, V.W.H.: Hydroxyapatite solubility in simple inorganic solutions. Arch Oral Biol. 49, 359–367 (2004). https://doi.org/10.1016/j.archoralbio.2003.12.004
38. Meng, J., Boschetto, F., Yagi, S., Marin, E., Adachi, T., Chen, X., Pezzotti, G., Sakurai, S., Yamane, H., Xu, H.: Design and manufacturing of 3D high-precision micro-fibrous poly

(L-lactic acid) scaffold using melt electrowriting technique for bone tissue engineering. Mater Des. 210, (2021). https://doi.org/10.1016/j.matdes.2021.110063

39. Marin, E., Yoshikawa, O., Boschetto, F., Honma, T., Adachi, T., Zhu, W., Xu, H., Kanamura, N., Yamamoto, T., Pezzotti, G.: Innovative electrospun PCL/fibroin/l-dopa scaffolds scaffolds supporting bone tissue regeneration. Biomedical Materials (Bristol). 17, (2022). https://doi.org/10.1088/1748-605X/ac6c68
40. Loewner, S., Heene, S., Baroth, T., Heymann, H., Cholewa, F., Blume, H., Blume, C.: Recent advances in melt electro writing for tissue engineering for 3D printing of microporous scaffolds for tissue engineering, (2022)
41. Zheng, G., Jiang, J., Wang, X., Li, W., Yu, Z., Lin, L.: High-aspect-ratio three-dimensional electrospinning via a tip guiding electrode. Mater Des. 198, (2021). https://doi.org/10.1016/j.matdes.2020.109304
42. Afghah, F., Dikyol, C., Altunbek, M., Koc, B.: Biomimicry in bio-manufacturing: Developments in melt electrospinning writing technology towards hybrid biomanufacturing, (2019)
43. Liu, Z., Ji, J., Tang, S., Qian, J., Yan, Y., Yu, B., Su, J., Wei, J.: Biocompatibility, degradability, bioactivity and osteogenesis of mesoporous/macroporous scaffolds of mesoporous diopside/poly(L-lactide) composite. J R Soc Interface. 12, (2015). https://doi.org/10.1098/rsif.2015.0507
44. Liu, Y.S., Huang, Q.L., Kienzle, A., Müller, W.E.G., Feng, Q.L.: In vitro degradation of porous PLLA/pearl powder composite scaffolds. Materials Science and Engineering C. 38, 227–234 (2014). https://doi.org/10.1016/j.msec.2014.02.007
45. Huang, J., Xiong, J., Liu, J., Zhu, W., Wang, D.: Investigation of the in vitro degradation of a novel polylactide/ nanohydroxyapatite composite for artificial bone. J Nanomater. 2013, (2013). https://doi.org/10.1155/2013/515741
46. Hu, Q., Liu, H. Bin, Weng, W.J., Cheng, K., Song, C.L., Du, P.Y., Zhao, G.L., Shen, G., Wang, J.X., Han, G.R.: Emulsion Technique Preparation of Nano-HA/PMMA Composites and In Vitro Evaluation. Key Eng Mater. 309–311, 553–556 (2006). https://doi.org/10.4028/www.scientific.net/kem.309-311.553
47. Szustakiewicz, K., Włodarczyk, M., Gazińska, M., Rudnicka, K., Płociński, P., Szymczyk-ziółkowska, P., Ziółkowski, G., Biernat, M., Sieja, K., Grzymajło, M., Jóźwiak, P., Michlewska, S., Trochimczuk, A.W.: The effect of pore size distribution and l-lysine

modified apatite whiskers (Hap) on osteoblasts response in plla/hap foam scaffolds obtained in the thermally induced phase separation process. Int J Mol Sci. 22, (2021). https://doi.org/10.3390/ijms22073607

48. Han, Y., Lian, M., Wu, Q., Qiao, Z., Sun, B., Dai, K.: Effect of Pore Size on Cell Behavior Using Melt Electrowritten Scaffolds. Front Bioeng Biotechnol. 9, (2021). https://doi.org/10.3389/fbioe.2021.629270
49. Rocha, C.R., Chávez-Flores, D., Zuverza-Mena, N., Duarte, A., Rocha-Gutiérrez, B.A., Zaragoza-Contreras, E.A., Flores-Gallardo, S.: Surface organo-modification of hydroxyapatites to improve PLA/HA compatibility. J Appl Polym Sci. 137, (2020). https://doi.org/10.1002/app.49293
50. Singla, P., Mehta, R., Berek, D., Upadhyay, S.N.: Microwave assisted synthesis of poly(lactic acid) and its characterization using size exclusion chromatography. Journal of Macromolecular Science, Part A: Pure and Applied Chemistry. 49, 963–970 (2012). https://doi.org/10.1080/10601325.2012.722858
51. Wu, C.S., Liao, H.T.: A new biodegradable blends prepared from polylactide and hyaluronic acid. Polymer (Guildf). 46, 10017–10026 (2005). https://doi.org/10.1016/j.polymer.2005.08.056
52. A novel hydroxyapatite –Hardystonite nanocomposite ceramic.
53. Gheisari, H., Karamian, E., Abdellahi, M.: A novel hydroxyapatite -Hardystonite nanocomposite ceramic. Ceram Int. 41, 5967–5975 (2015). https://doi.org/10.1016/j.ceramint.2015.01.033
54. Sahadat Hossain, M., Ahmed, S.: FTIR spectrum analysis to predict the crystalline and amorphous phases of hydroxyapatite: a comparison of vibrational motion to reflection. RSC Adv. 13, 14625–14630 (2023). https://doi.org/10.1039/d3ra02580b
55. Timchenko, P.E., Timchenko, E. V., Pisareva, E. V., Vlasov, M.Yu., Volova, L.T., Frolov, O.O., Kalimullina, A.R.: Experimental studies of hydroxyapatite by Raman spectroscopy. Journal of Optical Technology. 85, 130 (2018). https://doi.org/10.1364/jot.85.000130
56. Nosenko, V. V., Yaremko, A.M., Dzhagan, V.M., Vorona, I.P., Romanyuk, Y.A., Zatovsky, I. V.: Nature of some features in Raman spectra of hydroxyapatite-containing materials. Journal of Raman Spectroscopy. 47, 726–730 (2016). https://doi.org/10.1002/jrs.4883

57. Lin, T., Liu, X.Y., He, C.: Calculation of infrared/raman spectra and dielectric properties of various crystalline poly(lactic acid)s by density functional perturbation theory (DFPT) method. Journal of Physical Chemistry B. 116, 1524–1535 (2012). https://doi.org/10.1021/jp210123q

58. Babichuk, I.S., Lin, C., Qiu, Y., Zhu, H., Ye, T.T., Gao, Z., Yang, J.: Raman mapping of piezoelectric poly(l-lactic acid) films for force sensors. RSC Adv. 12, 27687–27697 (2022). https://doi.org/10.1039/d2ra04241j

59. Meng, J., Boschetto, F., Yagi, S., Marin, E., Adachi, T., Chen, X., Pezzotti, G., Sakurai, S., Sasaki, S., Aoki, T., Yamane, H., Xu, H.: Enhancing the bioactivity of melt electrowritten PLLA scaffold by convenient, green, and effective hydrophilic surface modification. Biomaterials Advances. 135, (2022). https://doi.org/10.1016/j.msec.2022.112686

60. Cairns, M.L., Dickson, G.R., Orr, J.F., Farrar, D., Hardacre, C., Sa, J., Lemoine, P., Mughal, M.Z., Buchanan, F.J.: The potential of electron beam radiation for simultaneous surface modification and bioresorption control of PLLA. J Biomed Mater Res A. 100 A, 2223–2229 (2012). https://doi.org/10.1002/jbm.a.34156

11. Ringraziamenti

Dopo un lungo percorso durato tanti anni (non ho voglia di contarli) sono finalmente arrivato ad un grande traguardo. Purtroppo per pandemie mondiali non ho potuto fare la laurea triennale in presenza; anche per questo ritengo che questa laurea magistrale sia un avvenimento molto importante nella mia vita; vita che ne ha passate di cotte e di crude, o come si dice, fatto cose visto gente. Un sacco di persone mi hanno supportato e seguito in questo percorso, purtroppo ho una pagina per scrivere e mi sono già dilungato troppo. Ringrazio intanto Vittorio Barbano, che nonostante momenti difficili, esami insuperabili e casini vari non si è dato per vinto ed è andato avanti a testa alta. Ringrazio poi i miei genitori e tutta la mia famiglia (un classico), che mi hanno sostenuto e affiancato nelle scelte che ho portato avanti, accettando anche di non vedermi per 5 mesi mentre ero in Giappone (esperienza magnifica). Ringrazio Lorenzo e Giulia, che mi hanno sopportato nelle mie follie, ripagate però da ravioli cinesi. Grazie anche al mitico "gruppo dell'America": Michela, Barbara, Francesco, Andrea, Stefano, Stefano. Abbiamo fatto un sacco di viaggi assieme e spero di poterne fare molti altri in futuro. Grazie anche a Luca, Luca…e già che ci siamo l'altro Luca ancora (troppi Luca!). Grazie anche a Davide, amico d'infanzia che mi ha sempre seguito e fatto divertire, prima o poi torno su WoW! Ringrazio e saluto Davide e Silvia, con cui ho viaggiato e scoperto le meraviglie del Giappone durante il periodo di tesi. Davide, scusa per le millemila domande sulla qualunque che ti facevo in laboratorio! Gomen! A Daniel, il mio tutor per la tesi, un enorme grazie per tutto il lavoro che hai fatto e la tua immensa disponibilità, in bocca al lupo per il tuo lavoro! A proposito, un saluto anche a tutte le altre persone che ho conosciuto a Kyoto, mi sono trovato davvero benissimo e mi sono divertito un mondo. Danilo, Matteo, Alessandro, Roberto, Alberto, Daniele e Davide, il gruppo "Ingegneristicamente": sono stati anni fantastici e tra un report di qua (gli assignment!!) ed una presentazione di là ce la siamo cavata e aiutati a vicenda. Grazie a Gabriele e Daniele, ad uno devo una pizza e all'altro una partita a scacchi! Un enorme abbraccio allo staff della Taverna dello Zio Fester, mi sono divertito un mondo quest'estate ed è stata un'esperienza fantastica, grazie di tutto! La pagina sta finendo e sicuro mi sono dimenticato qualcuno, quindi faccio una carrellata di nomi, spero di non dimenticare nessuno (nel caso grazie anche a chi manca!): grazie infinite di tutto Alberto, Nicolò, Simone, Kevin, Laura, Carlo, Luca, Davide, Manfred, Claudio, Davide, Simone, Stefano, Giovanni, Leonardo, Matteo, Sophie. Grazie e alla prossima avventura!